PHASE TRANSITIONS IN $K_{1-x}(NH_4)_xH_2PO_4$ SINGLE CRYSTALS

MAREK BROMBEREK


CENTRE FOR NFLD. STUDIES
MEMORIAL UNIVERSITY
OF NEWFOUNDLAND

Phase Transitions in $K_{1-x}(NH_4)_xH_2PO_4$ Single Crystals

by

© Marek Bromberek
M.Sc., M.Sc.

A thesis submitted to the
School of Graduate Studies
in partial fulfillment of the
requirements for the degree of
DOCTOR OF PHILOSOPHY.

Department of Physics and Physical Oceanography
Memorial University of Newfoundland

December 11, 2008

ST. JOHN'S NEWFOUNDLAND

Contents

Abstract

An apparatus for growing single crystals from aqueous solution by the slow evaporation method was constructed. Mixed crystals of $K_{1-x}(NH_4)_xH_2PO_4$ (KADP) with $(NH_4)H_2PO_4$ (ADP) fractions of 0.021 and 0.12 were successfully grown. Their composition was determined by means of the x-ray powder diffraction method. This analysis also suggests that those crystals are a mixture of two phases even at room temperature. The details of the structure of the additional phase could not be determined.

The dielectric constant ε of the mixed crystals as well as pure KH_2PO_4 (KDP) was measured along the polar axis in the temperature range from 20 K to 300 K. The frequency range of the applied electric field was from 100 Hz to 10 MHz. The data were analyzed by means of the standard Landau theory of phase transitions with coupling terms reflecting the interaction between the electric and elastic degrees of freedom. The temperature dependence of ε follows a typical Curie-Weiss behavior in the range of approximately 30 K above T_c for all crystals studied. The value of the critical temperature decreases with increasing ammonium ion content in agreement with previously published results. The analysis of the frequency dependence of the dielectric susceptibility clearly indicates the existence of two dispersion processes: resonant and relaxational. The former is attributed to the piezoelectric activity of all the crystals studied. The latter is the result of the response of the permanent dipole moments

present in ferroelectric crystals to the applied electric field. In the case of mixed crystals the relaxational dispersion is characterized by a distribution of relaxation times. Its mean relaxation time as well as its width increases with decreasing T. This is a typical behavior for mixed crystals for which the two end members of the solid solution in their pure form undergo ferroelectric and antiferroelectric phase transitions, respectively. This behavior is a result of competing long range interactions.

New results for the temperature dependence of the C_{66}^E and C_{11}^E elastic constants of the crystals were obtained by means of the Brillouin spectroscopy. In addition to that the soft acoustic mode behaviour was also studied by means of the piezoelectric resonance method. Both of them gave qualitatively similar results which also correlate very well with the dielectric measurements. All major differences could be explained by assuming an inhomogeneous distribution of the ammonium ions in the KDP matrix. The Brillouin results were also analyzed by means of the Landau theory. It approximates very well the temperature dependence of the C_{66}^E elastic constant in the paraelectric phase region for all crystals studied. The measured values of C_{66}^E below T_c are in general lower than those predicted by the model. The greater the NH_4 content the bigger the discrepancy.

Moreover, the analysis of the temperature dependence of the C_{66}^E elastic constant indicates the existence of a new phase in the mixed materials. Its stability region broadens with increasing NH_4 concentration. For the crystal with the highest ammonium concentration studied it coincides with the dielectric plateau region between 70 K and 55 K. At temperatures below the plateau region the $K_{0.88}(NH_4)_{0.12}H_2PO_4$ sample scattered the laser light very strongly. This is most likely caused by defects and sample inhomogeneities but annealing the sample for two hours at 400 K does not result in any significant change.

Acknowledgements

It is finally over. The eight-year battle has ended and it is time to move on. Before I do so I need to pause for a moment and reflect upon the past. I had a great privilege to work under the supervision of Dr. M. J. Clouter in a laboratory in which light scattering technique was always a primary research tool. The completion of this project would not be possible without his continuous financial support. He was always willing to share his tremendous knowledge of Brillouin spectroscopy with me, but most importantly he has never lost faith in me and he patiently responded to all my questions and concerns.

Two of my supervisory committee members, Drs. R. Mason and G. Quirion deserve special thanks. The former, from the Department of Earth Science, for helping me with my X - ray diffraction measurements and data analysis, the latter for sharing his expertise in the field of Landau theory of phase transitions. Our numerous discussions were of great importance for they allowed me to a gain considerable amount of confidence in both of those subject areas.

I would also like to acknowledge Dr. N. Zaitseva from Lawrence Livermore National Laboratory for talking me through one of my crystal growing sessions. We exchanged over a hundred emails one day when I was reporting to her what I was seeing in my crystal growing vessel and she was advising me on the next course of action. This help is greatly appreciated.

It so happened that most of the results presented in this thesis were collected in the Crystal Physics Division of the Institute of Physics in Poznan (Poland) during my yearly Christmas visits. A few of the team members deserve special thanks. Dr. B. Mroz, for providing pure KDP crystals. Dr. M. Wiesner for help with the dielectric as well as the piezoelectric measurements and for finding time to discuss my results with me, very often over the internet, even though he was busy writting his own habilitation. I am also indebted to Dr. S. Mielcarek for making sure that the Brillouin setup was ready for me when I got there, for help with setting up the tandem Fabry-Perot interferometer and primarily for wonderfull times during our yearly dinners at his house. I hope this tradition remains alive.

Last but not lest I would like to thank my friends Bill Kavanagh (M.Sc.), Ania Polomska (M.Sc.,M.Sc.), Jason Mercer (M.Sc.), Mark McDonald (M.Sc.) and Johnny Hawking (M.Sc.) for great times, tons of fun, intersting discussions and for being there for me at all times. Jason however deserves a special thanks. I would like to thank him for kindly preparing Figure 3.2 for me and for his help with many computer related issues I have encountered throughout my project. The speed with which he solved them was truly impressive.

List of Tables

List of Figures

Should reality be something that only a handful of the world's most advanced physicists understand? One would expect at least a majority of people to understand it. Should reality be expressible only in symbols that require university-level mathematics to manipulate? Should it be something that changes from year to year as new scientific theories are formulated? Should it be something about which different schools of physics can quarrel for years with no firm resolution on either side? If this is so then how is it fair to imprison a person in a mental hospital for life with no trial and no jury and no parole for "failing to understand reality"? By this criterion shouldn't all but a handful of the world's most advanced physicists be locked up for life? Who is crazy here and who is sane?

Robert M. Pirsig
-LILA-

Chapter 1

Introduction

1.1 Orientational Glasses

Crystalline solids are probably the most extensively studied materials in physics. The degree of understanding of their properties is sufficient to produce numerous technological applications. This state of affairs is undoubtedly related to the fact that material in that form posesses long range order, i.e their structure can be generated fully by indefinite repetition of certain groups of atoms, the content of a unit cell, in three dimensions. This idea was first introduced by Abbé Haüy as early as in 1784. Clearly the discovery of 32 crystal point groups by J. F. C. Hessel in 1830, an enumeration of all 230 space groups independently by E. S. Fedorov, A. M. Schoenflies and W. Barlow in the last decade of the nineteenth century, the discovery of X-ray radiation by W. C. Roentgen in 1895, and an experimental confirmation of the regular arrangement of atoms in solids by Max von Laue in 1912, were milestones in the development of lattice dynamics and electronic band theories. They, in turn were very successful theories explaining a large number of static and dynamic properties of crystals.

Solids in which there is no regular arrangement of atoms are located on the other end of the spectrum. They are called structural glasses or amorphous solids. An understanding of their physical properties, in particular the glass phase transition (i.e. their formation mechanism), is still lacking. Most difficulties come from a complete lack of internal symmetries in the atomic arrangement. It is therefore no surprise that a related group of physical systems, very often referred to as *orientational glasses*, attracted considerable attention from the scientific community. From the structural point of view these systems do possess a long range order, i.e. their atoms form a crystalline lattice. On the other hand they undergo a phase transition which displays certain characteristics qualitatively resembling the structural glass phase transition mentioned earlier. Therefore they present an opportunity to investigate slow dynamics of electric, magnetic or elastic degrees of freedom in a system with crystalline order.

In practice an orientational glass is often realized as a solid solution or mixed crystal. This very fact distinguishes them from structural glasses by introducing composition as an extra variable. In general they can be divided into two groups. The first one resembles very much a spin glass. It is made by introducing an impurity possessing a dipole or quadrupole moment into an otherwise neutral matrix of mother material. Some examples include alkali halides doped with hydroxyl or Li ions ($KCl:OH$, $KCl:Li$, $KBr:OH$), mixed cyanides ($(KBr)_{1-x}(KCN)_x$, $(KCl)_{1-x}(KCN)_x$, $(NaCl)_{1-x}(NaCN)_x$) or more exotic examples like a mixture of *ortho*-H_2 and *para*-H_2 and $Ar_{1-x}(N_2)_x$ mixed crystals. Characteristic phase diagrams for those materials are shown in Figure 1.1.

A structural glass results from random freezing of a disordered sublattice below a certain temperature often referred to as the glass phase transition temperature (T_g). When the concentration of impurities exceeds a certain critical value x_c their

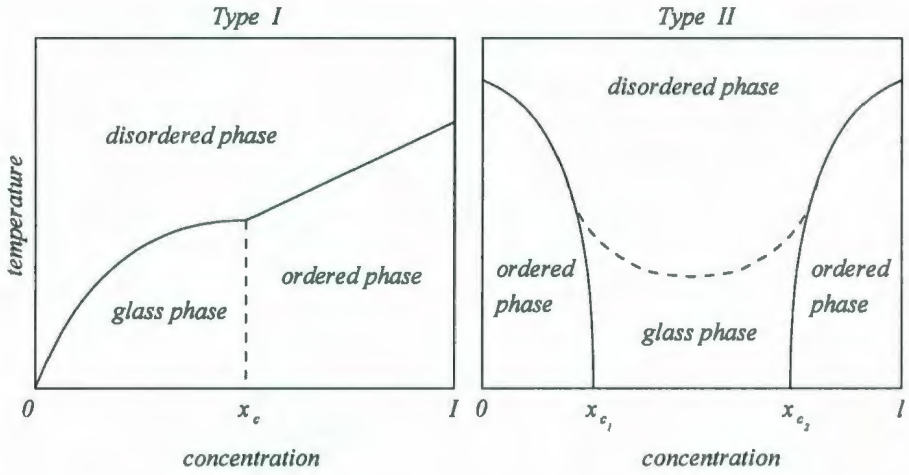

Figure 1.1: Schematic phase diagrams of type 1 and type 2 orientational glasses (see text).

mutual distances are short enough so that long range dipolar or quadrupolar interactions cause their long range ordering. On the other hand a type 2 orientational glass results from a mixture of two components displaying an ordered state at low temperatures in their pure form. The glass-like arrangement is a consequence of competing interactions. A mixture of NaCN with KCN, as well as mixed crystals of ferroelectric and antiferroelectric crystals from KDP family serve as primary examples in that group. The glass phase in those solid solutions is realized at low temperatures only for a limited range of intermediate concentrations.

Many ideas regarding the freezing process of reorienting moments in orientational glasses were taken from the studies of spin glasses which were discovered in 1930s by introducing magnetic impurities into a non magnetic matrix. The name itself was coined by B. R. Coles in 1970 for AuCo system. In 1975 Edwards and Anderson [4] as well as Sherington and Kirkpatrick [5] proposed mean field models of spin glass systems which laid the foundation for their theoretical treatment. Variations thereof are being used to date for modeling of orientational glasses.

1.2 The KDP Family of Crystals

Potassium dihydrogen phosphate ($KH_2PO_4 \equiv$ KDP) and ammonium dihydrogen phosphate ($(NH_4)H_2PO_4 \equiv$ ADP) are the most extensively studied members of a family of crystals often referred to as hydrogen bonded ferroelectrics. In this section a review of the most important experimental results, regarding the mechanism of the phase transformations taking place in those two crystals is presented. Since it is the solid solution of a ferroelectric KDP and antiferroelectric ADP crystals which is the topic of this thesis, emphasis is given to the major differences between the two, and the reasons why their low temperature behavior is so different.

Several compounds belong to the KDP family. They can be described by a general formula XY_2MO_4 where X = Li, Na, K, Rb, Cs or NH_4, Y = H or D and M = P or As. Some basic data regarding the most studied members of the phosphate family are listed in Table 1.1. All of them are isostructural at room temperature and undergo a phase transition to a ferroelectric (FE) or antiferroelectric (AFE) phase at the temperatures indicated. Several facts are obvious from inspecting Table 1.1. Although all of the crystals from the KDP family belong to tetragonal space group $I\bar{4}2d$ at room temperature, the difference between the c and a unit cell parameters is not large. Secondly, only compounds containing the NH_4^+ cation show antiferroelectric behavior at low temperatures. It is also evident that deuteration dramatically influences the phase transition temperature. This fact played a crucial role in the development of a scientific understanding of the phase transition mechanism in those crystals.

From a crystallographic point of view KDP crystals belong to the $I\bar{4}2d$ space group with Z=4 formula units per unit cell [6–9]. The content of its unit cell is shown schematically in Figure 1.2. The structure consists of almost undistorted PO_4 tetrahedral units [6, 7, 9, 10] interconnected by a network of $O - H \cdots O$ hydrogen bonds

Crystal	a [Å]	c [Å]	T_c [K]	Ordering
KH_2PO_4	7.452	6.959	123	FE
KD_2PO_4	7.471	6.956	213	FE
RbH_2PO_4	7.608	7.296	146	FE
RbD_2PO_4	–	–	218	FE
$(NH_4)H_2PO_4$	7.500	7.549	148	AF
$(NH_4)D_2PO_4$	7.502	7.520	242	AF

Table 1.1: Room temperature unit cell dimensions, phase transition temperatures and the type of low temperature order of selected hydrogen bonded ferroelectrics from the KDP family (data taken from [1]).

approximately 2.5 Å long [7]. Considerable effort was devoted to the determination of the precise position of hydrogens in the unit cell. Initially they were assumed to lie at the mid point between the two adjacent O atoms [6, 8, 9]. The hydrogen reflections were elongated along the hydrogen bond indicating some anisotropy of thermal motion [9]. However, later structural investigations [10–12] revealed considerable disorder in their positions, in support of the structural model of the phase transition proposed by Slater [13] in 1941. They indicated that the hydrogen atoms are located in a double well potential. The two minima are separated by a distance of approximately 0.4 Å [11, 12]. Moreover, the protons are tunneling from one minimum to the other along a line which is inclined at 6° to the xy plane [11].

Below T_c this crystal belongs to the orthorhombic crystallographic system with the space group Fdd2 and dimensions $a = 10.54$ Å, $b = 10.458$ Å, and $c = 6.918$ Å with Z=8 molecular units. Care needs to be taken in comparing the two structures. The low temperature unit cell is rotated by 45° around the [001] direction with respect to the paraelectric unit cell. It is possible to choose a different high temperature cell,

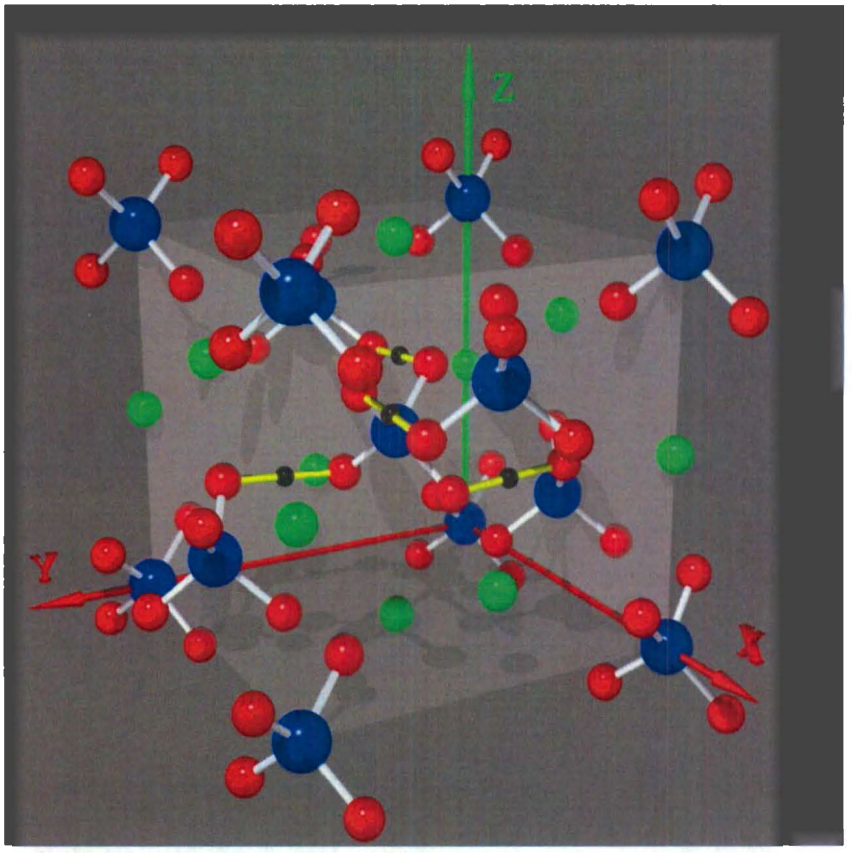

Figure 1.2: KDP unit cell. Different color spheres represent different atoms: red - oxygen, green - potassium, blue - phosphorus, black - hydrogen.

such that the x and y axis coincide with each other in both phases. Then the point group symbol is $F\bar{4}d2$, the unit cell has twice the volume of the original one and its dimensions are $a = b = 10.534$ Å and $c = 6.959$ Å. With that choice of unit cell the phase transition results in a small elongation of one of the sides and contraction of the other. Also, the unit cell type stays the same in accordance with the fact that there is no soft mode at the Brillouin zone boundary and no cell multiplication. From the point of view of the smaller cell however, the phase transition induces a shear deformation in the xy plane and the resulting cell becomes rhombic with the inner angles differing from 90° by about 27 minutes of arc [14].

Anomalous behavior of the longitudinal dielectric constant ϵ_c in potassium dihydrogen phosphate was reported initially by Busch and coworkers [15, 16]. Although they reported the transition temperature to be 115 K it is generally accepted now that T_c=123 K. The dielectric constant reaches values as high as 80000 at T_c [17]. In the paraelectric phase it obeys the Curie-Weiss law [18]. Below the transition temperature it drops to about 50 and stays at that level down to about 90 K where it returns to the room temperature value [17]. This decrease is accompanied by a peak in the temperature dependence of the imaginary part of ϵ. The temperature range between 90 K and T_c is often referred to as the *plateau-region*. Sample deuteration has a pronounced effect on the value of ϵ_c in that region [17]. This somewhat unusually high dielectric constant below T_c is attributed to the high mobility of domain walls [19–21], and the decrease of the value of the dielectric constant around 90 K is attributed to domain freezing [22]. In addition, there is an anomaly in the transverse dielectric constant ϵ_a at the transition temperature [16, 23, 24].

The ferroelectric phase transition in KDP is associated with the occurrence of spontaneous polarization P_s in the z direction [16], which can be reversed by application of an electric field [18]. Its saturation value reaches 5×10^{-6} C cm^{-2} [14, 16]. Since the direction of polarization can be in either the positive or negative z direction, below T_c KDP crystals consist of ferroelectric domains which differ in the orientation of P_s. Their existence was evident in early X-ray studies by means of a splitting of certain reflections [8] which disappeared after application of an electric field to the sample [9]. Moreover, the domain structure was later confirmed by direct optical observation [25]. Although initial reports of the temperature dependence of P_s indicated its gradual increase below T_c, later studies showed a discontinuity of the order of $\Delta P_s = 1.87 \pm 0.09$ μC cm^{-2} [18, 26]. This was clear indication of the discontinuous character of the phase transition, also confirmed by lattice constant measurements

close to T_c [27–29], which revealed a jump in the crystallographic a and b parameters of the order of 0.02 Å. The same measurements revealed thermal hysteresis of the order of 0.5 K or less, as expected in a case of a discontinuous transformation. Those results are in agreement with the specific heat measurements which clearly showed that the phase transformation in KH_2PO_4 crystal is associated with a latent heat of transformation. An entropy change of ΔS=0.74 cal mole^{-1} K^{-1} [30–32] was reported and attributed to the proton ordering.

Light scattering spectroscopy was also widely used to study the dynamics of the crystal lattice in KDP in both phases. It was discovered that the ferroelectric phase transition at 123 K is associated with an overdamped soft optical mode of B_2 symmetry [33, 34]. Also, application of external pressure to the sample caused the overdamped mode to become underdamped [35]. Moreover, since that mode has the symmetry of the strain component e_6 it makes the lattice unstable with respect to this deformation which in turn, *via* the piezoelectric effect, causes an acoustic lattice vibration frequency to drop to zero at T_c. This soft acoustic phonon associated with C_{66} elastic constant, was observed by Brody and Cummins [36, 37].

One of the most interesting features of the structural transformation in KDP is the fact that its nature changes with application of external electric field or pressure. This behavior was suggested by Schmidt [38]. The point on the phase diagram where the order of the phase transition changes is called tricritical. For the KDP crystal the value of the critical pressure p_c is approximately 2 kPa [39, 40]. Further increase of pressure completely suppresses the phase transition in KDP at 17 kPa [41]. The application of an electric field has a similar effect. The value of the critical field was reported to be approximately 300 Vcm^{-1}. In the vicinity of a critical point on the phase diagram one would expect to observe anomalous light scattering in the form of a central peak. Indeed, this phenomenon has been observed in KDP by Lagakos

in 1974 [42]. However, there are some doubts whether the central peak in KDP is due to nonpropagating entropy modes, resembling critical opalescence in fluids [43], or due to static defects. It was reported by Courtens in 1981 that the quasielastically scattered light decreases dramatically in intensity after annealing KDP samples for several hours at 140°C [44] suggesting the latter origin of this phenomena. The debate regarding the origin of the central peak continues to this day [45–47].

At the time when ferroelectricity was discovered in KDP crystals it was only the second crystal known to possess spontaneous polarization. The simplicity of its crystal structure led to the development of many microscopic models of the phase transition in this material. Three of them deserve special attention.

The first one was proposed by Slater [13] in 1941. He considered all possible arrangements of hydrogen atoms at low temperature, and assigned the lowest energy to those orientations of $(H_2PO_4)^-$ units which could give rise to a spontaneous polarization along the c axis. The procedure for counting all different combinations was suggested earlier by Pauling [48] for ice and is often referred to as the *ice rules*. Slater's model predicted a discontinuous phase transition to the ordered state with a configurational entropy of 0.69 calories. This value does not agree with the experimental result of 0.8 calories [30]. Moreover, if spontaneous polarization in KDP arises solely due to hydrogen ordering it can be calculated using the structural data mentioned earlier and its value would be $P_s = 3.5 \times 10^{-7}\,\mathrm{C\,cm^{-2}}$, i.e. only about 8% of the reported value [14]. It also did not include any mechanism which could be used to explain the large isotope effect observed in subsequent years [49].

The shortcomings of the Slater model were circumvented to some extent by Kobayashi [50]. In his approach the tunneling mode of hydrogen atoms was coupled to an optic mode of the lattice. This was in agreement with experimentally determined shifts of P and K sublattices [10]. It also explained the appearance of a

soft optic mode, and since the tunneling frequency was dependent on the mass of the hydrogen isotope it also explained to some extent the isotope effect.

However, it was recently pointed out [51] that the phase transition temperature in hydrogen bonded ferroelectrics is a linear function of the length of $O-H\cdots O$ bond and not of the mass of tunneling species. Moreover, as pointed out by Bilz *et al.* [52], about 97% of ferroelectric crystals known to date have an oxygen atom in their structure [53]. Those facts resulted in a development of an interatomic potential based on the nonlinear polarizabilities of oxygen atoms [52, 54, 55] which properly describe phase transitions in perovskites, hydrogen bonded crystals and other material undergoing displacive phase transition. Therefore, this approach promises to be the most adequate one for the problem at hand.

As mentioned earlier, ADP crystals are isomorphous with KDP crystals at room temperature. The unit cell parameters (see Table 1.1) were determined by X-ray diffraction [56–58] and neutron diffraction techniques [59, 60]. The positions of atoms are essentially the same as in KDP [57] with N taking the place of K atoms. Neutron data support an ordering of hydrogen atoms forming $O-H\cdots O$ bonds below the phase transition point. However, unlike in KDP, the hydrogens order in such a way that for a given PO_4 group one hydrogen on its top and one on its bottom gets closer/further away from corresponding oxygens. This arrangement produces an antiferroelectric order with individual dipoles oriented in [100] or [010] directions (which are equivalent above T_c) [60]. However, the location of H atoms from the NH_4 group indicates a possibility of the existence of a set of $N-H\cdots O$ bonds which seems to stabilize an antiferroelectric order below T_c. They are located at a general position in a unit cell [58, 59].

Anomalous behavior of the longitudinal and transverse dielectric constants was originally reported by Busch [16] in 1938. The phase transition takes place at 148 K.

It should be noted that the transverse dielectric constant in the KDP single crystal has a temperature dependence similar to that of the ADP crystal. Therefore the phase transition in KDP can be considered as ferroelectric and antiferroelectric at the same time. The low temperature structure is orthorhombic and belongs to the $P2_12_12_1$ space group [61]. It is a strongly first order, cell doubling transition characterized by thermal hysteresis $\Delta T = 15$ K [62]. Therefore, it should be accompanied by a softening of a Brillouin zone boundary optical phonon. However, because the crystal shatters at T_c it was not observed experimentally. Application of pressure causes T_c to shift towards lower temperatures and at p > 33 kbar there is no transition into the antiferroelectric phase [41].

The molar heat capacity of ADP in the range between 15 K and 300 K [63], and in the immediate vicinity of T_c [64], displays a peak characteristic of a first order phase transition with an entropy change of the order of 1.05 ± 0.04 cal K^{-1} mol^{-1} of which 0.8 cal K^{-1} mol^{-1} corresponds to hydrogen ordering and the remaining 0.2 cal K^{-1} mol^{-1} is due to reorientation of NH_4 radicals [65].

A model, in the spirit of Slater's model [13] of the transition in KDP crystal, and which properly predicted the antiferroelectric nature of the low temperature phase of ADP, was proposed by Nagamiya in 1952 [66]. However, as pointed out by Ishibashi [67] several different low temperature symmetries, corresponding to different arrangements of dipoles, are compatible with Slater's rules. He showed that dipolar interactions in the xy plane stabilize the low temperature structure in point group $P2_12_12_1$ as observed experimentally.

1.3 KADP and RADP Crystals

Several reports exist in scientific literature indicating that KDP and ADP crystals form a solid solution in the entire composition range [68–70]. However, due to a relatively large difference between ionic radii (K^+ *vs.* NH_4^+), it is difficult to grow good quality large single crystals. This is not the case for $Rb_{1-x}(NH_4)_xH_2PO_4$ (which is commonly abreviated as RADP:$100x$). As a consequence, there have been many more papers published regarding the physical properties of the latter [see ref 71]. It has been established however that both of the solid solutions mentioned above form crystals of tetragonal symmetry, at room temperature, for all compositions. The c lattice parameter changes linearly as a function of NH_4^+ content [2]. This fact is often used to determine the composition of those crystals.

Some of the earliest studies of mixed ferroelectric and antiferroelectric crystals were undertaken in order to understand the difference in ferroelectric behavior of the two end members of this solid solution [70]. It wasn't until the work of Courtens in 1982 [72], who suggested that RADP single crystals are electric analogs of spin glasses, when the systematic investigation of those materials started. He arrived at his conclusion by analyzing the temperature dependence of the dielectric constant in an RADP:35 crystal. It displayed a cusp like feature followed by decrease of the dielectric constant value accompanied by a peak in the imaginary part of the dielectric constant. Based on the dielectric constant and other measurements, the phase diagram for KADP mixed crystals can be schematically represented as shown in Figure 1.3. It should be pointed out that for arsenites it becomes asymmetric, *i.e.*, the glass-antiferroelectric phase boundary is shifted towards lower x values [73]. For phosphates $x_c^1 = 0.2$ and $x_c^2 = 0.7$ [74]. The exact determination of those concentration limits is difficult because it requires preparation of many samples with

small increments of x. The greyed out regions indicate the concentration range where a ferroelectrically or antiferroelectrically ordered phase coexists with a proton glass phase. There are two characteristic temperatures indicated on the phase diagram in

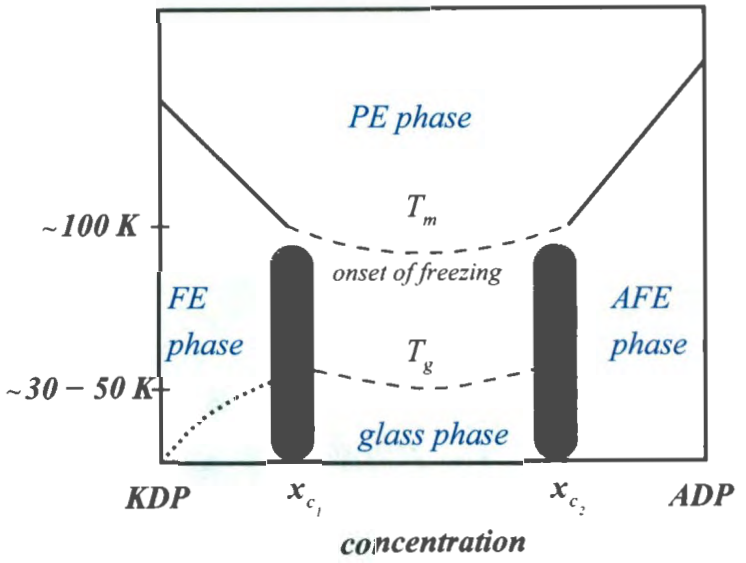

Figure 1.3: Schematic x-T phase diagram for $K_{1-x}(NH_4)_xH_2PO_4$ solid solution (after [74]).

Figure 1.3. First, T_m designates the onset of freezing. It is easily determined from a plot of the inverse dielectric constant *vs.* temperature. It corresponds to the temperature at which it starts to deviate from Curie-Weiss behavior. The temperature derivative of ϵ shows a minimum at that temperature. Second, T_g is the glass transition temperature, usually taken as a temperature at which the real part of ϵ displays a maximum value. This statement is true everywhere outside the mixed phase region where typically two maxima are observed, one due to ferro- or antiferroelectric phase transitions (taking place in clusters of those phases) and another one at the glass phase transition temperature. The approximate values of the two characteristic temperatures are also indicated at the left side of Figure 1.3.

Following Courtens' pioneering work about dipolar glass behavior in the RADP system [72], several papers became available reporting the results of various measurements in KADP mixed crystals [2, 75, 76]. Due to difficulties with crystal growth mentioned earlier they were mostly concerned about low impurity concentration limits. Based on those results it was confirmed that the temperature of the ferroelectric (antiferroelectric) phase transition in pure KDP (ADP) decreases with increasing ADP (KDP) concentration [75, 76]. On both ends of the phase diagram, the minority cations form hard defects [77] and cause rounding of the temperature dependencies of dielectric constant anomalies.

In the concentration range close to either of the critical concentrations the dielectric constant shows a broad maximum around $T_m - 20$K followed by an abrupt decrease of dielectric constant around T_g [78, 79]. This behavior is explained by the fact that in this concentration regime samples consist of a mixture of ferroelectric or antiferroelectric and proton glass phases. The anomalies around T_m are typically attributed to the onset of freezing of NH_4 ions responsible for an appearance of clusters showing antiferroelectric order. Their existence was confirmed in RADP crystals by Courtens [80] who observed a diffuse scattered peaks indicating antiferroelectric order. The low temperature decrease of ϵ is accompanied by an appreciable dielectric loss attributed to a *random ferroelectric type of ordering* [72], *i.e.*, a formation of the glass phase. The temperature of this decrease is different for cooling and heating runs [81]. The difference can be as high as 20 K.

In the intermediate concentration range, where the proton glass phase is realized, one would expect to observe a frequency dependent cusp in ε at the temperature T_g, in analogy with the temperature dependence of magnetic susceptibility in spin glass systems [82]. The higher the probing frequency the higher the temperature at which the maximum of the dielectric constant appears. This type of behavior in KADP

crystals was indeed observed [81]. The dielectric dispersion is very well described by the Vogel-Fulcher empirical law which in the case of RADP crystals is obeyed for 17 orders of magnitude in frequency [83].

The onset of freezing temperature T_m, clearly detectable in ε measurements was also confirmed by other techniques. Since it is usually attributed to the dynamics of NH_4^+ ions, several authors investigated the temperature dependence of its internal vibrations [84, 85]. Indeed, a symmetric stretching mode (ν_1) which is heavily overdamped at room temperature, becomes well defined around 100 K [85]. Its width remains constant for T < 60 K. Moreover, the process of proton ordering at low temperatures affects the frequencies of the internal modes of the PO_4 group. Its symmetric stretching frequency (ν_1) starts to decrease with decreasing temperature below T_m [86, 87]. Its ν_2 mode displays a pronounced asymmetry below T_m which is attributed to cluster formation [88].

At T_c in the pure KDP crystal the hydrogen bonds change their character from short and symmetric to longer and asymmetric [89], and the crystal expands [90]. Gradual deviations from typical Debye behavior of the unit cell dimensions and volume were reported in RADP:35 crystals [80] and were attributed to the progressive asymmetrization of hydrogen bonds. The temperature dependence of the lattice constants also shows significant deviation from typical Debye behavior. The anomalies start near 100 K which confirms the dielectric results. Moreover, the values of thermal expansion coefficients at low temperatures show that the structure of the RADP crystal contracts in the c direction as in pure ADP and expands in the a direction as in pure KDP. From a microscopic point of view those anomalies are related to progressive freezing of NH_4 librational motions which in turn is related to the ordering of protons participating in $N-H\cdots O$ hydrogen bonds. There are no detailed low temperature X-ray studies reported for KADP crystals. Boukhris [91, 92] re-

ported structural data for a series of concentrations at temperatures above 100 K. He concluded that $H_2PO_4^-$ ions are statically disordered at low temperatures.

It is worth noticing that careful examination of RADP and KADP systems with very low ammonium concentrations reveals that the glass state is realized in those crystals at very low temperatures. Trybula [93] reported dielectric studies of KADP and RADA (RADA stands for $Rb_{1-x}(NH_4)_xH_2AsO_4$) systems and suggested that the phase diagram for the low x values be modified as shown in Figure 1.3 by dashed line. He observed an anomalous behavior of the dielectric constant in the 0.3-1 K temperature range for crystals with $x < 0.002$ [93, 94].

The temperature and composition effects on the elastic properties of KADP and RADP solid solutions has not been studied systematically until now. This is a rather surprising fact since they can be readily measured with various experimental techniques. Ono [2] reported the temperature behavior of the elastic compliance coefficient $(\frac{1}{2}(s_{11} + s_{12}) + \frac{1}{4}s_{66}^E)$ for KADP determined by a resonance method from a 45°-Z cut bar. The compositions studied were x=0, 0.05, 0.11, 0.17, 0.25, 0.85, 0.97, 1.0. On the KDP rich side, the observed anomalies were attributed to the anomalies in ϵ_{33} which are piezoelectrically coupled to s_{66}. For $x = 0.97$ and 1.0 it was impossible to follow the piezoelectric resonance below the transition temperature. The elastic compliance coefficient for $x = 0.85$ showed no anomalous behavior in the entire temperature range studied. Careful Brillouin line shape studies of transverse acoustic wave propagating in [100] direction in RADP:35 single crystals allowed Courtens to confirm that the dielectric dispersion in this material is characterized by a broad distribution of relaxation times.

Therefore the primary purpose of this thesis is to investigate the temperature dependence of the soft acoustic mode in KDP-ADP solid solution. It is expected that it will be affected by the disorder introduced by incorporating NH_4 cations in

the crystal structure. Although originally it was planned to measure several crystals which covered a wide range of compositions, due to difficulties in obtaining good quality single crystals the experiments were performed only on two specimens. Two different methods were chosen for that purposes: the Brillouin spectroscopy, and the piezoelectric resonance method. The major difference between them is that the former is a local probe and therefore will not be affected by the existence of ferroelastic domains in the sample. The latter one should serve as an additional confirmation of the outcome of the former. Moreover, in order to correlate any anomalies observed in the temperature dependence of the elastic constants studied with the dielectric properties the latter will also be performed.

NEWTON'S THREE LAWS OF GRADUATION

Though famous for his seminal work in Mechanics, Isaac Newton's theories on the prediction of a doctoral graduation formulated while still a grad student at Cambridge remain his most important contribution to academia.

FIRST LAW

"A grad student in procrastination tends to stay in procrastination unless an external force is applied to it"

This postulate is known as the "***Law of Inertia***" and was originally discovered experimentally by Galileo four years before Newton was born when he threatened to cut his grad student's funding. This resulted in a quickening of the student's research progress.

Galileo's observations were later perfected by Descartes through the application of "Weekly Meetings."

Before Galileo's time, it was wrongfully thought that grad students would rest only as long as no work was required of them and that in the absence of external forces, they would graduate by themselves.

(From Encyclopaedia Britannica)

PHD.STANFORD.EDU
JORGE CHAM ©THE STANFORD DAILY

Pile Higher and Deeper
by Jorge Cham
www.phdcomics.com

Chapter 2

Theory

2.1 Light Scattering in Anisotropic Materials

The mechanism of the light scattering process can be summarized as follows. The electric field from an incident light beam induces an oscillating dipole moment in the scattering volume which re-radiates electromagnetic waves of the same frequency in all directions. At the same time however, the material properties of the scattering medium are being modulated as a result of thermally excited elementary excitations (phonons, magnons, plasmons etc.). Therefore the scattered light will consist of a central, unshifted line and a number of satellite peaks which will be shifted towards higher and lower frequencies by the amount equal to the frequency of the elementary excitations under study. In general the efficiency of the scattering process is a function of (i) the frequency of incident radiation, (ii) the state of polarization of incident and scattered beams, (iii) the relative orientation of incident and scattered wavevectors (scattering geometry) and (iv), in a case of anisotropic materials, the orientation of the electric field and wavevectors of the incident and scattered beams with respect to crystallographic axes of the specimen. In some cases care has to be

taken to consider the influence of sample boundaries (refraction) on the result of the experiments. However, the necessary corrections can be determined based on geometric optics [95], or as is very often the case, entirely avoided by adequate sample preparation. Those latter corrections, as well as corrections due to surface reflections and absorption inside the material are not considered in what follows.

From quantum mechanical point of view, the scattering process can be described as emission or absorption of a phonon: an "optical" one in a case of Raman scattering, and "acoustic" in a case of Brillouin scattering. In the case of phonon absorption the scattered photon will gain energy, and in a case of phonon emission scattered photon will lose energy. As a result the spectrum of scattered light will consist of an unshifted peak centered at the frequency of the incident radiation used, and additional peaks displaced from the center by the amount proportional to the energy of the elementary excitation. In a case of the Brillouin spectra at most three shifted lines can be observed, one corresponding to longitudinal, and two corresponding to transverse acoustic waves propagating in the sample. The energy of incident and scattered photon and that of the phonon involved are related because the energy ($\hbar\omega$) has to be conserved in the scattering process. Therefore we have

$$\omega_i = \omega_s \pm \omega \tag{2.1}$$

where ω_i, ω_s and ω are incident, scattered and phonon frequencies respectively. In the above formula the plus and minus signs correspond to anti-Stokes and Stokes peaks, respectively.

The number of modes observed depends on the symmetry of the crystal studied and the geometry of the experiment. The choice of the direction of the acoustic phonon wavevector studied is governed by the conservation of momentum which relates the wavevectors of incident and scattered photons and that of the phonon

involved. It takes the following form

$$\vec{k}_i = \vec{k}_s \pm \vec{q} \tag{2.2}$$

where the subscripts i and s stand for incident and scattered, respectively, and $\vec{q}$ is the acoustic phonon wavevector. From the wavevector triangle shown in Figure 2.1 the amplitude of $\vec{q}$ can be readily calculated. Starting from

$$q^2 = k_i^2 + k_s^2 - 2k_i k_s \cos\theta \tag{2.3}$$

and substituting the dispersion relations for incident and scattered photons as well as for the acoustic phonon, the following expression can be obtained

$$\omega = \frac{\omega_i v_a}{c}\sqrt{n_i^2 + n_s^2 + 2n_i n_s \cos\theta} \tag{2.4}$$

where ω and ω_i are the frequencies of the acoustic phonon and the incident light, respectively, v_a is the acoustic phonon velocity, c is the speed of light in vacuum, n_i and n_s are the indices of refraction in the direction of the incident and scattered wavevectors, respectively, and θ is the scattering angle. Since Brillouin shifts are very small relative to the frequency of the laser light the incident and scattered frequency were set equal to each other in the above equation. In the case when the difference between n_i and n_s can be neglected, Equation 2.4 simplifies and takes the form

$$\omega = 2\frac{v_a}{c}\omega_i n \sin\left(\frac{\theta}{2}\right) \tag{2.5}$$

The above equation is used to calculate the velocity of the acoustic phonon v_a given the Brillouin shift ω. Those velocities are related to the elastic properties of the material studied through the solution of the elastic wave equation for an anisotropic medium

$$\rho\frac{\partial^2 u_k}{\partial t^2} = C_{klmn}\frac{\partial^2 u_n}{\partial x_l \partial x_m} \tag{2.6}$$

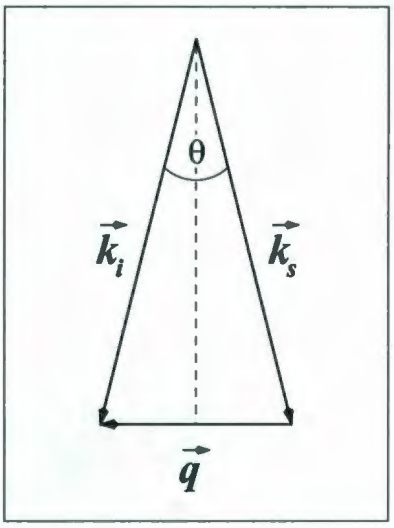

Figure 2.1: Conservation of momentum diagram.

in which ρ is the density, u_k is the component of the displacement vector of a volume element considered and C_{klmn} are elements of the elastic stiffness tensor. After substituting a plane wave solution into Equation 2.6 it takes the following form

$$\rho u_k \omega^2 = C_{klmn} k_l k_m u_n \tag{2.7}$$

where ω and k_l are the acoustic wave frequency and its wavevector component, respectively. The above equation is typically expressed in terms of the acoustic wave velocity and the direction cosines of the phonon wavevector as

$$\left(\rho v^2 \delta_{ij} - \Gamma_{ij}\right) u_n = 0 \tag{2.8}$$

where $\Gamma = C_{klmn} n_l n_m$ and n_l are the direction cosines of the acoustic phonon wavevector. Equation 2.8 is an eigenvalue problem. It has three solutions which represent the three acoustic waves propagating in a given direction in the crystal.

The relative orientation of the incident and scattered wavevectors is not always a sufficient condition for observation of a particular phonon. The orientation of the electric field in the incident and scattered beams with respect to the crystallographic

direction plays also an important role because for some combinations of them the scattering cross section is identically zero. Those *selection rules* can be derived from classical electrodynamics. It can be shown [96] that the Rayleigh ratio (differential cross section per unit volume) for the j-th acoustic mode is proportional to

$$R^j \propto \left[\hat{e}_s \cdot \mathrm{T}^j \cdot \hat{e}_i\right]^2 \tag{2.9}$$

where $\hat{e}_s$ and $\hat{e}_i$ are the unit vectors in the direction of the electric field vectors of the scattered and incident light, respectively. The tensor T expresses the strain dependence of the optical indicatrix, and has elements of the form:

$$\mathrm{T}_{\alpha\beta} = \varepsilon_{\alpha\alpha}\varepsilon_{\beta\beta}p_{\alpha\beta\gamma\delta}\epsilon_{\gamma\delta} \tag{2.10}$$

where $\varepsilon_{\alpha\alpha}$ are the components of the dielectric tensor, $p_{\alpha\beta\gamma\delta}$ are the components of the photo-elastic tensor (also known as Pockel's coefficients) and $\epsilon_{\gamma\delta}$ are the components of elastic strain produced by propagating acoustic wave.

To illustrate the concepts presented above we will consider the case of Brillouin scattering in a pure KDP crystal. In this case the strain component ϵ_6 has the same symmetry as the order parameter (see section 2.3.2). Because of piezoelectric interaction a soft optical mode drives the frequency of one of the acoustic modes to zero at T_c. The phonon in question is the one which propagates in the x (or y) direction and is polarized in the y (or x) direction, because

$$\epsilon_6 = \epsilon_{12} = \left(\frac{\partial u_1}{\partial x_2} + \frac{\partial u_2}{\partial x_1}\right). \tag{2.11}$$

In other words a transverse acoustic wave propagating in the x direction and polarized in the [010] direction is nothing but an oscillating ϵ_6 strain component. As an example we will now consider how to set up the experiment so that we can observe this particular phonon.

We start with solving Christoffel's equation. The phonon wave vector has the direction cosines [100]. Th elastic constants matrix for a tetragonal system (point group $\bar{4}2m$) has the form [97]:

$$C_{\bar{4}2m} = \begin{bmatrix} C_{11} & C_{12} & C_{13} & 0 & 0 & 0 \\ C_{12} & C_{11} & C_{13} & 0 & 0 & 0 \\ C_{13} & C_{13} & C_{33} & 0 & 0 & 0 \\ 0 & 0 & 0 & C_{44} & 0 & 0 \\ 0 & 0 & 0 & 0 & C_{44} & 0 \\ 0 & 0 & 0 & 0 & 0 & C_{66} \end{bmatrix} \tag{2.12}$$

We can now write down Equation 2.8 in a matrix form as:

$$\begin{bmatrix} C_{11} - \rho v_1^2 & 0 & 0 \\ 0 & C_{44} - \rho v_2^2 & 0 \\ 0 & 0 & C_{66} - \rho v_3^2 \end{bmatrix} \begin{bmatrix} u_1 \\ u_2 \\ u_3 \end{bmatrix} = 0 \tag{2.13}$$

There are three solutions to Equation 2.13. The eigenvalues give the relations between elastic constants and the speeds of sound for a given mode. The eigenvectors are the components of the displacement vector which describe the polarization of the elastic wave. In the above case the solutions are

$$v_1 = \sqrt{\frac{C_{11}}{\rho}} \qquad u_1 = [1, 0, 0] \tag{2.14}$$

$$v_2 = \sqrt{\frac{C_{44}}{\rho}} \qquad u_2 = [0, 0, 1] \tag{2.15}$$

$$v_3 = \sqrt{\frac{C_{66}}{\rho}} \qquad u_3 = [0, 1, 0] \tag{2.16}$$

Clearly the first solution corresponds to the longitudinal and the other two to the two transverse acoustic waves. Therefore one would expect to observe three distinct Brillouin lines. However, it is necessary to check the selection rules mentioned earlier.

In what follows we will assume the right angle scattering geometry, i.e. the incident and scattered photon wavevectors are perpendicular to each other ($\theta = 90°$ in Equation 2.4). There are two sample geometries which will allow the study of the phonon of interest. Either (110) or (101) crystallographic planes are aligned with the scattering plane. They are depicted in Figure 2.2. In the first case the incident and scattered beams can be polarized in either (001) or (110) direction whereas in the second case the polarization direction is (010) or (101). Using an appropriate form of the T tensor [96] and Equation 2.9 it can be shown that the soft mode in the KDP crystal can be observed only in the arrangement shown in Figure 2.2 b) with the incident beam polarization perpendicular to the scattering plane. Without an

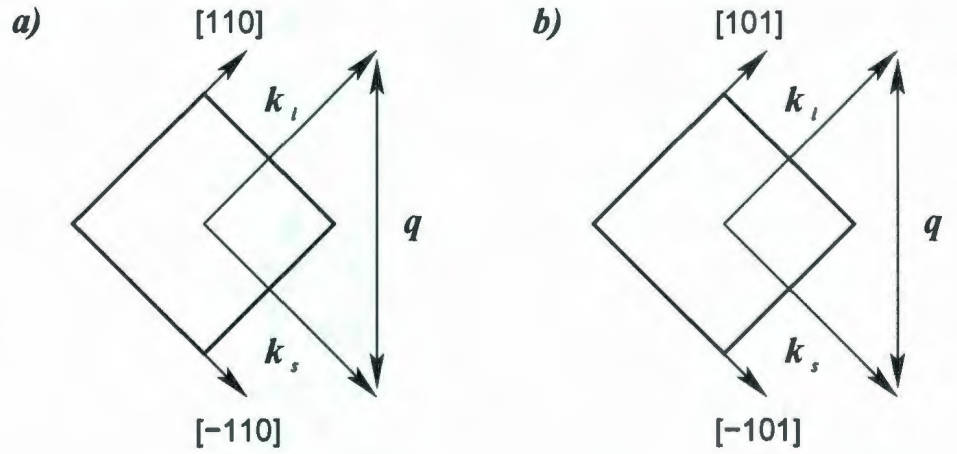

Figure 2.2: Two experimental arrangements allowing observation of an acoustic phonon propagating in the [100] direction.

analyzer in the path of the scattered light both longitudinal and transverse acoustic modes will be visible. By setting the analyzer with the easy axis perpendicular to the scattering plane one can select only the LA mode. If the analyzer's easy axis is parallel to the scattering plane only the soft transverse acoustic (TA) mode will be observed.

2.2 Relaxation Phenomena in Solids

The principal technique for investigating dipolar glasses, formed as solid solutions of ferro and antiferroelectrics, is a dielectric susceptibility measurement. Those measurements are typically performed with a commercial capacitance bridge which can measure small capacitance and a phase difference between voltage and current while applying an ac voltage to a sample prepared in a form of a parallel plate capacitor. Measurements are fully automatic and can be performed relatively easily over a wide range of temperatures and frequencies.

If a dielectric material is introduced between the plates of a parallel plate capacitor its ability to store electric charge increases. The relative difference in capacitance

$$\frac{\Delta C}{C_0} = \frac{C - C_0}{C_0} = \frac{C}{C_0} - 1 = \frac{\varepsilon}{\varepsilon_0} - 1 = \varepsilon_r - 1 \tag{2.17}$$

depends on the material used. In the above formula ε, ε_r and ε_0 are dielectric permittivity, relative dielectric permittivity (often referred to as the dielectric constant) and permittivity of free space ($\varepsilon_0 = 8.854 \cdot 10^{-12}\,\mathrm{Fm}^{-1}$), respectively. C_0 is the capacitance in vacuum. This increase in capacitance is a direct consequence of the appearance of polarization inside the dielectric. The resulting dipole moment density is proportional to the electric field and given by

$$\vec{P} = \varepsilon_0 \chi_r \vec{E} = \chi \vec{E} \tag{2.18}$$

where the constant of proportionality χ_r is called the dielectric susceptibility[1]. Materials for which the above formula holds are called linear dielectrics.

Introducing the dielectric displacement vector $\vec{D}$ we can write the fundamental equation of electrodynamics in the presence of dielectrics as

$$\vec{D} = \varepsilon_0 \vec{E} + \vec{P} \tag{2.19}$$

[1] the subscript r indicates dimensionless relative quantities and will be used throughout this thesis

which with the help of Equation 2.18 becomes

$$\vec{D} = \varepsilon_0(1 + \chi_r)\vec{E} \tag{2.20}$$

Therefore $\vec{D}$ is also proportional to $\vec{E}$ and it can be shown [98] that

$$\vec{D} = \varepsilon\vec{E} \tag{2.21}$$

which leads to the relation between the relative dielectric permeability and susceptibility of the form

$$\frac{\varepsilon}{\varepsilon_0} = \varepsilon_r = (1 + \chi_r). \tag{2.22}$$

In principle there are three major contributions to the polarization in the dielectric: dipolar, ionic, and electronic. The latter two are due to the relative displacements of positive and negative ions or charges and inertia is the primary loss mechanism in this case. For the dipolar contribution polarization is a result of reorientation of units possessing a dipole moment, or a mutual displacement of entities with opposite charges. The first mechanism is responsible for the appearance of spontaneous polarization in order-disorder, and the second in displacive, types of phase transitions. The loss mechanism is considerably more complex in this case and is typically related to interactions with the crystal lattice.

In general, the loss mechanisms mentioned above prevent the polarization vector from being in phase with the applied field. Therefore there will be a phase difference and to account for that it is necessary to introduce the dielectric susceptibility as a complex number. Equation 2.18 can be written as

$$\vec{P}_0 e^{-i(\omega t+\delta)} = (\mathrm{Re}\,[\chi] + i\,\mathrm{Im}[\chi])\,\vec{E}_0 e^{-i\omega t} \tag{2.23}$$

where $\mathrm{Re}[\chi]$ and $\mathrm{Im}[\chi]$ are real and imaginary parts of the susceptibility respectively and δ is a phase difference between $\vec{P}$ and $\vec{E}$. It is easy to show that

$$\tan\delta = \frac{\mathrm{Im}[\chi]}{\mathrm{Re}[\chi]} \tag{2.24}$$

If we now assume after Debye [99] that after a step-like application of an electric field to a dielectric sample its polarization will increase exponentially with a single relaxation time then we can write down an equation describing that process as

$$\vec{P}(t) = \chi_\infty \vec{E}(t) + \varepsilon_0 \int_{-\infty}^{t} \vec{E}(u)\alpha(t-u)du \tag{2.25}$$

where α is a polarization decay function which, based on our earlier assumptions, can be written as

$$\alpha(t) = \alpha_0 e^{-t/\tau} \tag{2.26}$$

with τ being the relaxation time.

The integral in Equation 2.25 represents a superposition principle which says that the response of a system to an external stimulus can be represented as a sum of responses to individual elementary excitations. If we also assume that the field was turned on at $t = 0$ then the integral from $-\infty$ to 0 vanishes (because $\vec{E} = 0$). Moreover, we have separated out the instantaneous response due to electronic polarization which is represented by the first term on the right hand side of it. Under the assumption that in the static field the system reaches an equilibrium after sufficiently long time it can be shown [100] that the constant α_0 in Equation 2.26 is:

$$\alpha_0 = \frac{\varepsilon_0 - \varepsilon_\infty}{\tau} \tag{2.27}$$

Substituting it back to Equation 2.26 gives the well known Debye formula for the dielectric constant

$$\varepsilon(\omega) = \varepsilon_\infty + \frac{\varepsilon_0 - \varepsilon_\infty}{1 + i\omega\tau} \tag{2.28}$$

Separating real and imaginary parts we obtain

$$\mathrm{Re}[\varepsilon(\omega)] = \varepsilon_\infty + \frac{\varepsilon_0 - \varepsilon_\infty}{1 + (\omega\tau)^2} \tag{2.29}$$

$$\mathrm{Im}[\varepsilon(\omega)] = \frac{(\varepsilon_0 - \varepsilon_\infty)\omega\tau}{1 + (\omega\tau)^2} \tag{2.30}$$

The general shapes of the real and imaginary parts of the dielectric constant are plotted in Figure 2.3. Clearly increasing the frequency of the applied field causes the dielectric constant to drop from the static value ε_0 to the high frequency value ε_∞. This drop is accompanied by a peak in the imaginary part of $\mathrm{Im}[\varepsilon(\omega)]$. Eliminating $\omega\tau$

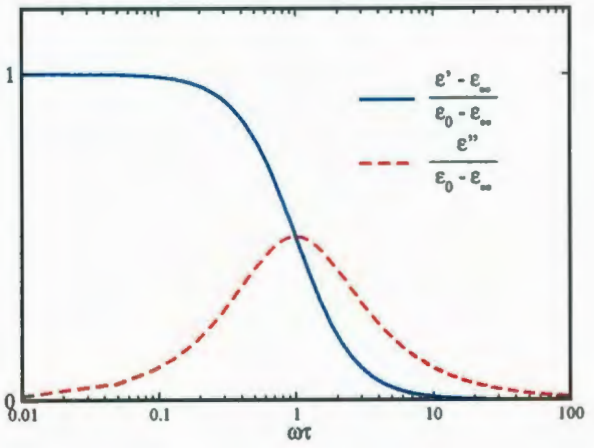

Figure 2.3: Real and imaginary parts of the dielectric constant according to the Debye model.

from equations 2.29 and 2.30 gives the following relation between $\mathrm{Re}[\varepsilon]$ and $\mathrm{Im}[\varepsilon]$

$$\left[\mathrm{Re}[\varepsilon] - \frac{(\varepsilon_0 + \varepsilon_\infty)}{2}\right]^2 + \mathrm{Im}[\varepsilon]^2 = \left[\frac{\varepsilon_0 - \varepsilon_\infty}{2}\right]^2. \tag{2.31}$$

therefore the plot of $\mathrm{Im}[\varepsilon]$ *vs.* $\mathrm{Re}[\varepsilon]$, referred to as a Cole-Cole diagram, is a semicircle of radius $(\varepsilon_0 - \varepsilon_\infty)/2$ centered on the real axis at a point with coordinates $(\frac{(\varepsilon_0+\varepsilon_\infty)}{2}, 0)$. However, most physical systems do not show this type of behaviour. Instead they are properly described by a semicircular arc, resulting from a shift of the center of the Debye circle below $\mathrm{Re}[\varepsilon]$ axis. It can be shown [101, 102] that this type of Cole-Cole diagram corresponds to the following expression for the dielectric constant

$$\varepsilon(\omega) = \varepsilon_\infty + \frac{\varepsilon_0 - \varepsilon_\infty}{1 + (i\omega\tau)^{1-h}}, \tag{2.32}$$

and corresponds to a dispersion mechanism characterized by a logarithmic distribution of relaxation times, $g(\tau)$, which is symmetric around a point $\tau = \tau_0$.

Another empirical formula often used to describe dielectric data properly has the following form

$$\varepsilon(\omega) = \varepsilon_\infty + \frac{\varepsilon_0 - \varepsilon_\infty}{(1 + i\omega\tau)^l} \tag{2.33}$$

and is called the Davidson-Cole equation. It has been introduced by D. W. Davidson [103, 104] in order to explain the dielectric dispersion of glycerol and propylene glycol which displayed a skewed circular arc. This type of Cole-Cole graph is characteristic of materials for which the $g(\tau)$ is asymmetric with respect to $\tau = \tau_0$ point.

The normalized plots of the above equations together with corresponding Cole-Cole diagrams are shown in Figure 2.4. Clearly equation 2.32 and 2.33 reduce to the Debye equation for $h = 0$ and $l = 1$ respectively. Both of the equations mentioned earlier are empirical in nature. There is no microscopic model which would justify either of them. Nonetheless, they have been used extensively in analyzing dielectric data with great success. The expression for the frequency dependence of the dielectric constant in cases when the dispersion process is characterized by the distribution of relaxation times takes the following form

$$\varepsilon(\omega) = \int_0^\infty \frac{g(\tau)}{1 + i\,\omega\tau}\, d(\ln(\tau)) \tag{2.34}$$

and the $g(\tau)$ fulfills the normalization condition

$$\int_0^\infty g(\tau)\, d(\ln(\tau)) = 1 \tag{2.35}$$

Although the determination of the exact form of the $g(\ln(\tau))$ function is a challenging task [105] the empirical parameters h and l appearing in equations 2.32 and 2.33 can be readily obtained. In a case of Cole-Cole equation it can be calculated from the

$$\varepsilon = \varepsilon_\infty + \frac{\varepsilon_s - \varepsilon_\infty}{1 + (i\omega\tau)^{1-h}} \qquad \varepsilon = \varepsilon_\infty + \frac{\varepsilon_s - \varepsilon_\infty}{(1 + i\omega\tau)^{l}}$$

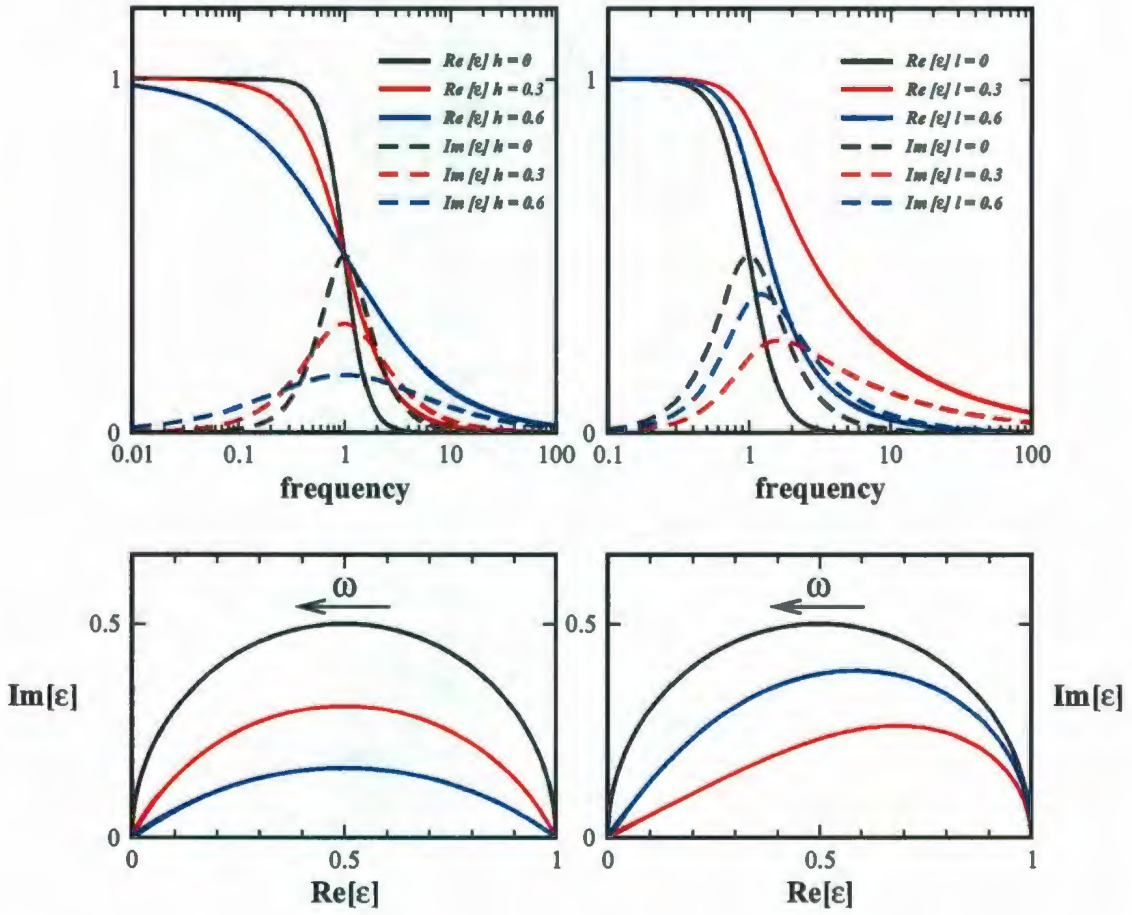

Figure 2.4: Real and imaginary parts of the dielectric constant (top) and corresponding Cole-Cole diagrams (bottom) according to Debye model.

position of the center of the circular arc which in this case is described by the equation

$$(\mathrm{Re}[\varepsilon] - a)^2 + (\mathrm{Im}[\varepsilon] - b)^2 = R^2 \tag{2.36}$$

where a and b are the abscissa and ordinate of its center and R its radius. It can be shown that those parameters can be described by the following formulae:

$$\begin{aligned} a &= \frac{1}{2}(\varepsilon_0 + \varepsilon_\infty) \\ b &= -\frac{1}{2}(\varepsilon_0 - \varepsilon_\infty)\tan\left(\frac{h\pi}{2}\right) \\ R &= \frac{1}{2}(\varepsilon_0 - \varepsilon_\infty)\sec\left(\frac{h\pi}{2}\right) \end{aligned} \tag{2.37}$$

In the case of Davidson-Cole expression the parameter l is related to the slope of a tangent to the skewed circular arc on the high frequency side and is given by the following relation

$$\frac{\mathrm{d}}{\mathrm{d}(\mathrm{Re}[\varepsilon])}\mathrm{Im}[\varepsilon] = \tan\left(\frac{l\pi}{2}\right) \tag{2.38}$$

In light of the above considerations the advantage of presenting the dielectric constant results in a form of a Cole-Cole diagram is clear. It allows one to recognize immediately the most important characteristics of the dispersion process involved.

2.3 Landau Model

2.3.1 General Considerations

The Landau theory of continuous phase transitions plays a prominent role in their phenomenological description. It is solely based on symmetry considerations and makes use of the concept of an order parameter - a physical quantity which takes non-zero values in the less symmetrical, low temperature phase. Although initially introduced to model phase changes of the second kind, it can also be successfully

applied for discontinuous phase transitions. The main assumption of the theory is that in the immediate vicinity of phase transition temperature the order parameter Q is sufficiently small so that the Gibbs free energy can be expanded as a power series.

To determine the form of the Landau expansion it is necessary to know the symmetry of the order parameter which is determined by a pair of point groups describing the high and low temperature phase, respectively. For Landau theory to be applicable, the low temperature point group has to be a subgroup of the high temperature one. In general for a given symmetry of the high temperature phase several low temperature phases can be conceived. In the group theory language, every one of them is subduced by a physically irreducible representation of the high symmetry point group. It is often referred to as an active representation. The details of the group theoretical analysis are beyond the scope of this thesis. However, for phase transitions without a change in translational symmetry[2] its results have been tabulated by Janovec [106]. According to his paper the order parameter for a phase transition from $\bar{4}$2m to mm2 belongs to a one dimensional irreducible representation B_2. It follows that its transformation properties are the same as those of the z component of a polar vector. Keeping that in mind we can now write the Landau free energy in general form as

$$\Delta G = G - G_0 = \alpha Q + \frac{1}{2}AQ^2 + \beta\frac{1}{3}Q^3 + \frac{1}{4}BQ^4 + \frac{1}{5}\gamma Q^5 + \frac{1}{6}DQ^6 + \ldots \qquad (2.39)$$

where G_0 is the free energy of the initial phase, and α, A, β, B and D are coefficients which can be temperature and pressure dependent. The above equation has to be invariant with respect to all of the symmetry elements of the high temperature phase which, as mentioned earlier, belongs to point group $\bar{4}$2m. The generating element of

[2]In the case of the KDP crystal translational symmetry of both phases is preserved if one chooses a unit cell rotated by 45 deg with respect to a unit cell described by I$\bar{4}$2m. The space group symbol is then F$\bar{4}$d2

this point group is the four-fold symmetry axis $\bar{4}$ along the [001] direction. It consists of rotation around z axis by a 90 degree angle, followed by an inversion with respect to the center of the coordinate system. An arbitrary vector with components (x,y,z) transorms into $(-y,x,-z)$ under this symmetry operation. Therefore it can be seen that the odd power terms in Equation 2.39 are not permitted, and their respective coefficients (β and γ) are set to zero. Nonzero values of β would imply that the phase transition is of first order, and since this term is absent we have to set the coefficient B as negative. It is sufficient to truncate the expansion after the term proportional to Q^6. The Equation 2.39 can now be written as

$$\Delta G = \frac{1}{2}AQ^2 - \frac{1}{4}BQ^4 + \frac{1}{6}DQ^6 \tag{2.40}$$

where now the coefficient B is strictly positive.

It is typically assumed that only coefficient A is temperature (or pressure) dependent. In fact, A is usually written as a power series expansion around the critical temperature $\mathrm{T} = \mathrm{T}_0$ and only the first term is considered. It takes the following form

$$A = a(T - T_0) \tag{2.41}$$

where T stands for the absolute temperature of the system, and a is strictly positive. Thus the first term in the Landau free energy changes sign at T_0. The order parameter dependence of ΔG for some characteristic temperatures, which will be described later in this section, is shown in Figure 2.5.

The equilibrium value of the order parameter and its temperature dependence below the phase transition temperature can now be determined from the requirement that the stable phase is the one for which the value of the order parameter minimizes

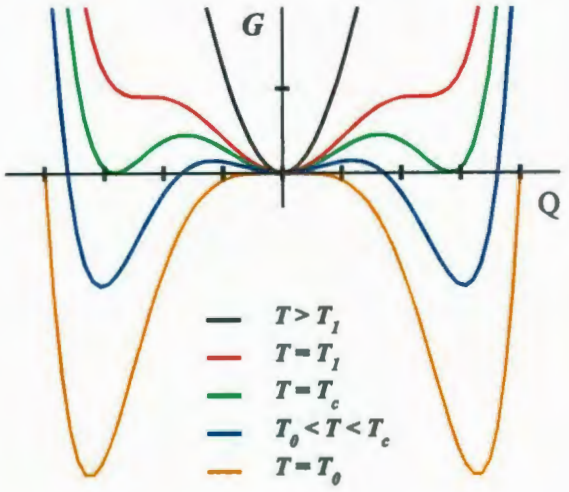

Figure 2.5: Landau free energy as a function of order parameter at different temperatures.

Equation 2.40. Therefore the conditions for the minimum of ΔG are

$$\frac{\partial G}{\partial Q} = 0 \tag{2.42}$$

$$\frac{\partial^2 G}{\partial Q^2} \geqslant 0 \tag{2.43}$$

The first of the above conditions gives us

$$\frac{\partial G}{\partial Q} = Q_0 \left[a(T - T_0') - BQ^2 + DQ^4\right] = 0. \tag{2.44}$$

One of the roots of Equation 2.44, namely $Q = 0$, by definition describes the symmetric phase. However, the term in square brackets deserves closer attention. Its roots are given by

$$Q^2 = \frac{B \pm \sqrt{B^2 - 4Da(T - T_0)}}{2D} \tag{2.45}$$

In the above equation, the solution with negative sign corresponds to a local maximum separating the two local minima (see curve $T = T_1$ in Figure 2.5) and therefore has to be rejected. We then have the following equation for the temperature dependence

of the order parameter in the low temperature phase

$$Q^2(T) = \frac{B + \sqrt{B^2 - 4Da(T - T_0)}}{2D}. \tag{2.46}$$

Clearly the value of the order parameter at T_0 is

$$Q(T_0) = \sqrt{\frac{B}{D}}. \tag{2.47}$$

Moreover, since Q is a real, physical quantity, Equation 2.46 is valid only if the expression under the square root is positive. This condition is fullfilled for temperatures lower than

$$T_1 = T_0 + \frac{B^2}{4Da}. \tag{2.48}$$

The low temperature phase becomes metastable at T_1. The value of the order parameter at that point can be readily calculated from Equation 2.46 by setting $T = T_1$ and using Equation 2.48. The result is

$$Q(T_1) = \sqrt{\frac{B}{2D}} \tag{2.49}$$

Substituting this value into Equation 2.43 shows that this point corresponds to a saddle point on the $G(Q)$ curve as expected from Figure 2.5. For temperatures higher then T_1 the order parameter vanishes as expected. The temperature range between T_0 and T_1 is the phase coexistence region and describes the maximum theoretical value for the thermal hysteresis. Although the phase transition can in principle occur at any temperature in that range, it is typically assumed that it takes place when both phases are equally stable, i.e. they are characterized by the same value of the Gibbs free energy. Inspecting Figure 2.5 it can be seen that this condition is true for $T = T_c$. By substituting the general solution for the order parameter given by Equation 2.46 into the Landau free energy 2.40 and equating the result to zero it can be shown that both phases have the same free energy at

$$T_c = T_0 + \frac{3B^2}{16Da} = T_0 + \frac{3}{4}\Delta T. \tag{2.50}$$

where $\Delta T = T_1 - T_0$. Below T_c the high symmetry phase becomes metastable until the temperature T_0 is reached. The value of the order parameter at T_c can be easily evaluated by setting $T = T_c$ in Equation 2.46 and using Equation 2.50. The result is

$$Q(T_c) = \sqrt{\frac{3B}{4D}}. \tag{2.51}$$

and corresponds to a minimum as can be ascertained by direct substitution into Equation 2.43. The temperature dependence of the order parameter, as well as all the characteristic temperatures (T_0, T_1, T_c) are schematically schown in Figure 2.6. The above results show that, in a case when B=0, all three temperatures (T_0, T_1 and T_c) will be the same. Moreover, the value of the order parameter at T_c will be zero indicating that the phase transition will change its character and become a continuous one. This in fact is the case for KDP under pressure.

The temperature dependence of the inverse susceptibility conjugate to the order parameter at constant strain (κ^ϵ) can be obtained by taking the second derivative of equation 2.40 with respect to Q. The result is

$$\frac{\partial \Delta G^2}{\partial Q^2} = \kappa^\epsilon = A - 3BQ^2 + 5DQ^4 \tag{2.52}$$

and, since by definition order parameter is zero above T_c, we obtain a linear dependence of κ^ϵ on temperature in that region

$$\kappa^\epsilon = a(T - T_0) = a(T - T_c) + \frac{3B^2}{16D} \tag{2.53}$$

The susceptibility in the low temperature phase is described by Equation 2.52 which expressed in terms of T_c gives

$$\kappa^\epsilon = 8a(T_c - T) + \frac{3B^2}{4D} \tag{2.54}$$

It should be mentioned that the dielectric susceptibility given by equations 2.53 and 2.54 correspond to a condition of constant strain or the mechanically clamped crystal.

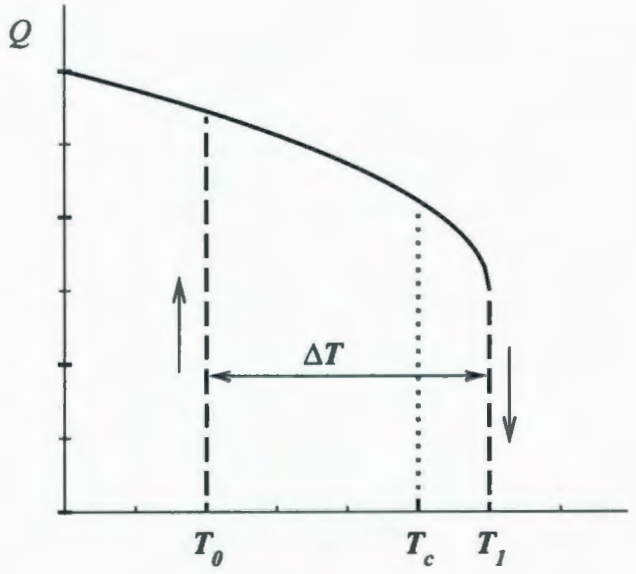

Figure 2.6: Schematic representation of temperature dependence of the order parameter.

Moreover, introducing an elastic energy term into equation 2.40 of the form

$$G_{el} = \frac{1}{2} C^{Q} \epsilon^2 \tag{2.55}$$

where C^Q and ϵ are the elastic stiffness at constant order parameter and the strain respectively, and calculating the second derivative of the resulting free energy with respect to strain would show that C^Q does not depend on temperature. This is because there is no coupling term in the Landau free energy.

The above analysis shows that the phase transition modeled by Equation 2.40 is of discontinuous character since it is characterized by a region of phase coexistence ($T_0 < T < T_c$) and a discontinuity of the order parameter at T_c.

2.3.2 Coupling to the Order Parameter

The general characteristics of the Landau model of a first order phase transition were presented in the previous section. Here it will be expanded in order to investigate the effect of coupling between order parameter and strain. Moreover, since the phase transition in pure KDP is of proper ferroelectric type, the order parameter can be identified as the polarization directed along [001] direction (P_3). Also the component of elastic strain belonging to B_2 irreducible representation of $\bar{4}$m2 is ϵ_6. Therefore, we will rewrite Equation 2.40 using those symbols. It takes the following form

$$\Delta G = \frac{1}{2}AP_3^2 - \frac{1}{4}BP_3^4 + \frac{1}{6}DP_3^6 - b\epsilon_6 P_3 + \frac{1}{2}C_{66}^P\epsilon_6^2 \tag{2.56}$$

where b, ϵ_6 and C_{66}^P are the coupling coefficient, component of elastic strain tensor, and elastic constant at constant polarization, respectively. Since P_3 and ϵ_6 transform in the same way Equation 2.56 is invariant under the symmetry operations of the $\bar{4}$2m point group. The second last term in that equation represents the coupling between e_6 and P_3. Although, in principle other coupling terms could be introduced into the model the one present in the above equation is the lowest order one sufficient to account for the changes of the C_{66} elastic constant which is of primary interest in this work. The last term in Equation 2.56 represents the elastic free energy. As before only the coefficient A depends on temperature (see Equation 2.41).

Before we proceed to evaluate the temperature dependence of the dielectric and elastic constants we will eliminate ϵ_6 from Equation 2.56 by making use of the conditions for the minimum in the form

$$\frac{\partial \Delta G}{\partial \epsilon_6} = 0 \tag{2.57}$$

which is also the condition for zero stress, i.e it describes the situation for a mechan-

ically free crystal. Expressing ϵ_6 in terms of P_3

$$\epsilon_6 = \frac{b}{C_{66}^P} P_3 \tag{2.58}$$

and substituing the above relation into Equation 2.56 gives

$$\Delta G = \frac{1}{2}\left(A - \frac{b^2}{C_{66}^P}\right) P_3^2 - \frac{1}{4} B P_3^4 + \frac{1}{6} D P_3^6 \tag{2.59}$$

As can be seen from the above equation, including the coupling term in the Landau free energy results in the appearance of an extra constant in the coefficient of the term proportional to the square of polarization. Setting

$$A - \frac{b^2}{C_{66}^P} = \tilde{A} \tag{2.60}$$

or, since the coefficents A and $\tilde{A}$ are the inverse dielectric susceptibilities for conditions of zero strain or zero stress, respectively, we arrive at the following relation between the two

$$\kappa^\epsilon - \kappa^\sigma = \frac{b^2}{C_{66}^P} \tag{2.61}$$

Equation 2.59 can be written as

$$\Delta G = \frac{1}{2} \tilde{A} P_3^2 - \frac{1}{4} B P_3^4 + \frac{1}{6} D P_3^6 \tag{2.62}$$

where

$$\tilde{A} = \tilde{a}(T - \tilde{T}_0) \tag{2.63}$$

and $\tilde{T}_0$ is the renormalized critical temperature.

As can be seen from the above considerations clamped and free inverse dielectric susceptibilities will in principle exhibit different temperature dependencies. If we now make use of the original assumption that the parameters b and C^P are temperature independent it is easy to see that the Curie-Weiss constants for free and clamped crystals will be the same. In general this does not have to be the case. Although

those parameters might not display any anomalies at the transition temperature they will, in general, be a function of temperature. Therefore the relations between the parameters appearing in the Curie-Weiss law for clamped and free crystals can, in the linear approximation, be written as [107]

$$a - \tilde{a} = M \tag{2.64}$$

and

$$T_0 - \tilde{T}_0 = -\frac{L}{\tilde{a} + M} \tag{2.65}$$

where

$$L = \frac{b^2\left(\tilde{T}_0\right)}{C_{66}^P\left(\tilde{T}_0\right)} \tag{2.66}$$

and

$$M = \frac{d}{dT}\left[\frac{b^2(T)}{C_{66}^P(T)}\right]_{T=\tilde{T}_0} \tag{2.67}$$

Therefore we can see that clamping the crystal might destroy the phase transition if $\tilde{T}_0$ becomes less then 0 K. However, the order of the phase transition will remain the same.

Since Equation 2.62 has exactly the same form as 2.40 all the results from previous section can immediately be rewritten for the case with a coupling between order parameter and strain. In particular the temperature dependence of the inverse of the dielectric susceptibility at constant stress will take the following form

$$\kappa^\sigma = \tilde{a}(T - \tilde{T}_0) \tag{2.68}$$

in paraelectric phase and

$$\kappa^\sigma = 4\tilde{a}(T - \tilde{T}_0) \tag{2.69}$$

for temperatures below T_c.

We will now proceed to the calculation of the temperature dependence of the elastic constant C_{66}^E. It can be calculated from the following formula due to Slonczewski [108]

$$C_{66}^E = \frac{\partial^2 \Delta G}{\partial e_6^2} - \frac{\left(\frac{\partial^2 G}{\partial e_6 \partial P_3}\right)^2}{\frac{\partial^2 G}{\partial P_3^2}} \tag{2.70}$$

which gives

$$C_{66}^E = C_{66}^P - \frac{b^2}{A - 3BP_3^2 + 5DP_3^4} \tag{2.71}$$

for a general expression of the temperature dependence of C_{66}^E. Since the denominator in the right hand side of Equation 2.70 is the clamped inverse dielectric susceptibility given by equation 2.52, Equation 2.71 can be rewritten as

$$C_{66}^E = C_{66}^P - \frac{b^2}{\kappa^\epsilon} \tag{2.72}$$

The above formula indicates that the value of C_{66}^E elastic constant will decrease hyperbolically in the vicinity of the phase transition. Therefore one will observe a softening of the transverse acoustic mode of which velocity is proportional to that component of the elastic constant (see equation 2.16). Moreover, from Equation 2.61 and 2.72 it can be seen immediately that

$$\frac{\kappa^\sigma}{\kappa^\epsilon} = \frac{C_{66}^E}{C_{66}^P} = 1 - \frac{b^2}{C_{66}^P \kappa^\epsilon} = 1 - k^2 \tag{2.73}$$

In the above analysis, the polarization P and strain ϵ were chosen as the independent thermodynamic variables. However, by choosing another set, different relations between material constants can be derived by analysing the resulting equations of state. In particular, choosing stress σ and the electric field E as independent vari-

ables it can be shown that the following relations are true

$$\chi^{\epsilon} - \chi^{\sigma} = -\frac{d^2}{S_{66}^E} \tag{2.74}$$

$$S_{66}^P - S_{66}^E = -\frac{d^2}{\chi^{\sigma}} \tag{2.75}$$

where χ is the dielectric susceptibility as defined in Equation 2.18, S stands for a component of the elastic compliance matrix, d is the piezoelectric coeficient as defined in Equation 4.10, and superscripts indicate appropriate thermodynamic variables held constant. From the last two equations it is easy to see that the ratios of the dielectric susceptibilities and the elastic compliance components in this case can be written as

$$\frac{\chi^{\epsilon}}{\chi^{\sigma}} = \frac{S_{66}^P}{S_{66}^E} = 1 - \frac{d^2}{\chi^{\sigma} S_{66}^E} = 1 - p^2 \tag{2.76}$$

where all of the symbols were already defined earlier. In both equations 2.73 and 2.76 the constants k and p are called the coupling coeficients in the piezoelectric transducer literature. They are a function of different material parameters, appropriate for a given choice of the independent thermodynamical variables used in the theoretical analysis. As dimensionless quantities, they are very well suited for comparing two different materials and characterize a given material's ability to convert stored energy (mechanical or electrical) into work.

The above considerations show that in cases of bilinear coupling between strain and the polarization, the coupling constant in the Landau free energy can be identified as a component of the piezoelectric tensor. Its anomalous temperature behaviour brings about changes of the sound velocity manifested as the softening of acoustic phonon branch. Moreover, by choosing appropriate measurement conditions, and using appropriate relations between the material constants obtained from the experiments, considerable amount of information about the thermodynamics of those materials can be acquired.

NEWTON'S THREE LAWS OF GRADUATION

First published in 1679, Isaac Newton's ***"Procrastinare Unnaturalis Principia Mathematica"*** is often considered one of the most important single works in the history of science. Its Second Law is the most powerful of the three, allowing mathematical calculation of the duration of a doctoral degree.

SECOND LAW

"The age, a, of a doctoral process is directly proportional to the flexibility, f, given by the advisor and inversely proportional to the student's motivation, m"

Mathematically, this postulate translates to:

$$age_{PhD} = \frac{flexibility}{motivation}$$

$$a = F / m$$

$$\therefore F = m\,a$$

This Law is a quantitative description of the effect of the forces experienced by a grad student. A highly motivated student may still remain in grad school given enough flexibility. As motivation goes to zero, the duration of the PhD goes to infinity.

PHD.STANFORD.EDU

Pile Higher and Deeper
by Jorge Cham
www.phdcomics.com

Chapter 3

Crystal Growth and Characterization

3.1 Introductory Remarks

Studying materials in the form of a single crystal allows one to investigate the anisotropy of a given physical property, i.e its dependence on the measurement direction with respect to crystallographic axes. A vast number of methods for growing single crystals are known and have been used in industry as well as in research institutions. Based on the mother phase they can be divided into three groups: growth from vapor, liquid, and from a solid. The method chosen for this work, a slow evaporation, belongs to the second group and is probably the most widely used method of growing single crystals for research purposes.

From a thermodynamics point of view crystal growth is a first order phase transition with all of its characteristics, i.e a latent heat or a nucleation barrier and the existence of a phase front, or interface, between a growing crystal and a solution. Standard thermodynamic considerations can be applied to study this process. In

particular if we consider, for simplicity, a system composed of two, solid and liquid phases the change of Gibbs free energy of each phase can be expressed as

$$dG_i = -S_i dT + V_i dp + \mu_i dN_i \tag{3.1}$$

where S is the entropy, V a total volume of the system, T its temperature, p its pressure and μ_i is a chemical potential of i-th phase[1]. Because G is a state function and as such it is an additive quantity one can express an infinitesimal change in free energy of the system by a sum of the changes of the Gibbs energies of its phases as

$$dG = dG_1 + dG_2 \tag{3.2}$$

and because at equilibrium $dG = 0$ we have

$$dG_1 = -dG_2 \tag{3.3}$$

Using Equation 3.1 we arrive at the condition for equilibrium at constant temperature and pressure in the following form

$$\mu_1 dN_1 + \mu_2 dN_2 = 0. \tag{3.4}$$

Since the total number of moles in the system is constant, therefore

$$dN_1 = -dN_2 \tag{3.5}$$

and the change of the amount of one phase is equal to the negative change of the amount of the other. Using Equation 3.5 in 3.4 we have

$$\mu_1 dN_1 - \mu_2 dN_1 = 0 \tag{3.6}$$

$$(\mu_1 - \mu_2) dN_1 = 0 \tag{3.7}$$

[1]Strictly speaking the chemical potential is defined for each component of each phase, therefore for crystal growth from a solution one needs to distinguish between the chemical potentials of each ions. However for the purposes of this thesis the definition as given in the text is sufficient.

which leads directly to the new expression for the equilibrium condition in the form

$$\mu_1 = \mu_2 \tag{3.8}$$

Equation 3.8 is a very important one. It is the condition for the existence of thermodynamic as well as chemical equilibrium. It tells us that if the chemical potential of a given chemical species is not equal in two adjacent phases there will be a flow of matter from the phase of higher chemical potential into a phase of lower chemical potential until an equilibrium is reached. The above result can be generalized to systems composed of several phases and chemical species [109]. In this case the chemical potential of each species has to be equal for each pair of phases.

The difference of chemical potential of a given substance in two different phases is therefore a fundamental driving force for crystallization. Writing the chemical potential as

$$\mu = \mu^* + RT \ln x \tag{3.9}$$

where R is the gas constant, x is a mole fraction and μ^* is the chemical potential of the pure substance, the chemical potential difference $\Delta\mu$ can now be written as

$$\Delta\mu = RT \ln \left(\frac{x}{x^*}\right) \tag{3.10}$$

where x^* is the mole fraction of a solute in saturated solution. Clearly the equilibrium condition 3.8 is fulfilled only if $x = x^*$. Any deviation causes crystallization or dissolution. The quantity x/x^* is called the fundamental supersaturation ratio (S_x). There are other ways of expressing the supersaturation condition. The most common are: concentration driving force Δc given by

$$\Delta c = c - c^*, \tag{3.11}$$

and relative supersaturation σ given by

$$\sigma = \frac{\Delta c}{c^*} = S - 1 \tag{3.12}$$

In all of the above formulas c stands for concentration which can be expressed in many different units [110], and c^* is the saturation concentration.

Clearly it is of outmost importance to know the values of c^*, which while plotted as a function of temperature constitutes the solubility curve. An example of the temperature dependence of c^* for the KDP crystal is shown in Figure 3.1 (solid line). Three different regions are indicated on that diagram. First, located below the

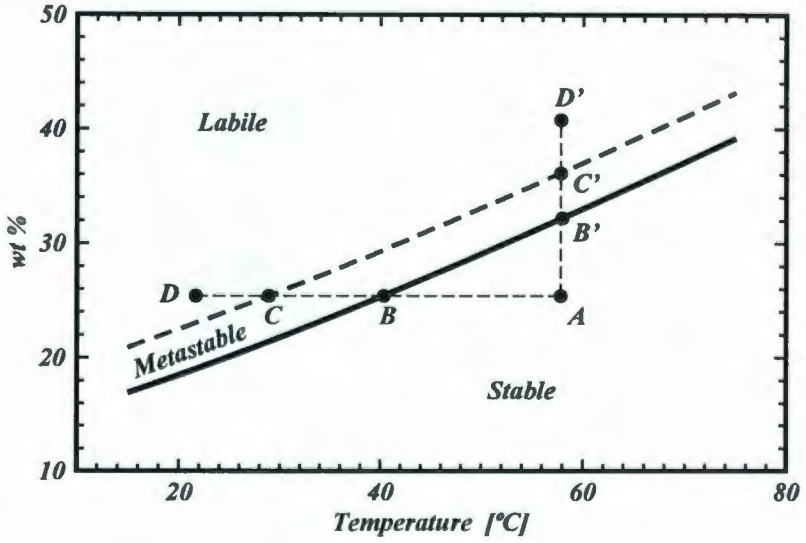

Figure 3.1: Solubility-supersolubility diagram.

solubility curve, is the stable region. The growth process does not take place there, and any new material introduced into the solution will dissolve until the concentration reaches the saturation point. A second, metastable region, is located above the solubility curve and below the dashed line. This is a region in which crystals are always grown. However, the growth process has to be initiated externally, typically by seeding, because the supersaturation value is not high enough to produce a stable nucleus. The critical radius of a spherical nucleus is related to the supersaturation by

$$r_c = \frac{2\gamma\nu}{kT \ln S} \tag{3.13}$$

where γ is the interfacial tension and ν a molecular volume [110]. For different shapes the above formula will differ by a constant geometrical factor. Therefore the metastable zone provides ideal conditions for crystal growth because no new crystallization centers will appear inside the crystallizer after the seed has been introduced.

In the third region, called labile, spontaneous nucleation will most probably occur but is not inevitable. The location of the dashed line in Figure 3.1 is ill-defined because its location is very strongly dependent on many factors, like: solution agitation, temperature, impurity content etc. The three regions were initially identified and named in 1897 by Ostwald [111].

There are two ways of creating a state of supersaturation in crystal growth from a solution. First one is a very slow temperature lowering. This process is represented in Figure 3.1 by line ABCD. It is not unusual for the rate of cooling to be of the order of 0.02 K per day. Second, the one used in this thesis, is represented by line AB'C'D' and relies on slow removal of solvent from the crystal growing vessel to maintain the state of supersaturation as the crystal grows. Traditionally the rate of solvent evaporation was controlled by means of heated condenser mounted on top of the crystal growing vessel [112]. Its temperature could be adjusted allowing for a faster or slower evaporation rate.

Once the nucleus (or a seed) is present in the supersaturated solution the crystal growth process begins. This process can be described, based on the adsorption layer theory of crystal growth [110], as follows. At first a two dimensional nucleus has to be formed on a perfectly flat crystal surface. In general it requires less energy to do so, i.e a lower supersaturation level is required, than that to form a 3D nucleus. Once this step is completed the two dimensional island grows by means of a surface diffusion process until an entire surface is covered, and the process starts over. Obviously, due to local supersaturation fluctuations it can happen that a new nucleus will be formed

on an unfinished layer. The surface of a growing crystal can therefore be schematically represented as shown in Figure 3.2. A single incomplete layer of ad-atoms is shown on

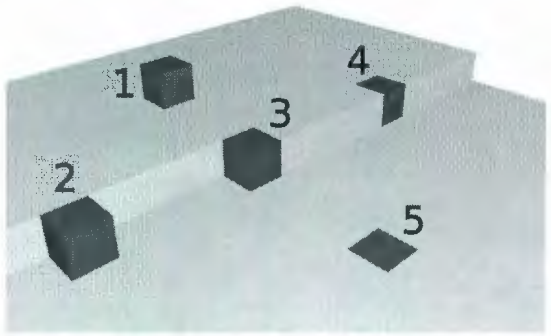

Figure 3.2: Surface of a growing crystal.

this figure. The dark blocks represent crystal building units (atoms, molecules, ions). A single surface of each of the blocks represents a single bond which would have to be broken in order to detach a given unit from the surface. The block 1 represents a 2D nucleus. Since it is attached only by a single bond it would be more stable if it was surrounded by more ad-atoms, i.e. if it was a part of critical radius nucleus. The block 5 represents an atom incorporated into the crystal face and in contrary to the block 1 has only one unsaturated dangling bond. The blocks 2 through 4 represent all intermediate situations with 4, 3 and 2 unsaturated bonds respectively. However, position 3 has an equal number of saturated and unsaturated bonds. It is called a half-crystal position or a kink. The removal of an atom or molecule from this position does not change the number of unsaturated bonds, therefore it does not influence the surface energy.

This simple model has one major problem. Experiments showed that crystals grow even if the supersaturation level is lower then that required for the surface nucleation. To resolve this discrepancy Frank [113] suggested that a dislocation present

on the surface of a crystal is an uninterrupted source of kinks in which molecules can be attached. Indeed the growth of crystals on dislocations, and formation of the dislocation hillock or spiral, was observed experimentally for KDP and ADP crystals [114].

It is not difficult to imagine that any impurities present in the solution will have an effect on the growth of the crystal. Some of them may enhance the growth, others can slow it down or act selectively on different faces of the crystal. They can have an effect on the solution (changing the supersaturation level) or on a crystal surface (blocking active sites, for example kinks). In fact even the solvent used can be regarded as an impurity. It is not uncommon therefore to observe a crystal developing a different habit if grown from a solution with a different solvent. In the case of the KDP and ADP crystals it has been shown that trace quantities (as low as 5ppm) of Cr^{3+} and Fe^{3+} affect the face growth rates and result in tapering of the prism faces of those crystals [115, 116].

In the case of growth of mixed crystals the situation is a little more complicated since that process can be viewed as a growth of one end member in the presence of an enormous amount of impurities (the other member of the solid solution). The presence of the other salt in the solution influences the solubility of the first one and vice versa. Therefore the concept of a solubility curve for mixed crystal is also a tricky one. Typically, however, two salts with a common ion will form a solid solution in the entire concentration range. It is not necessarily true though that the composition of the growing crystal will be the same as the composition of the solution. In fact this is very rarely the case and for the KADP solid solution this has been determined experimentally by Ono [2]. The relation is schematically shown in Figure 3.3. If the relation between crystal and solution composition was a straight line the solution would be ideal. Since it is not, the solid solution of KDP and ADP crystals can be

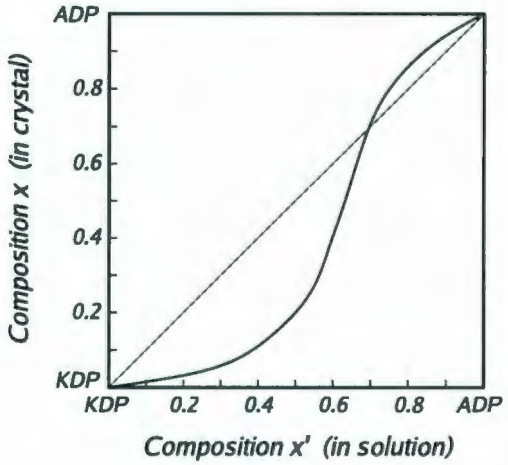

Figure 3.3: Composition x of a crystal *vs.* composition x' of a solution used to grow it (after [2]).

regarded as non-ideal. Nonetheless the two crystals form a solid solution in the entire concentration range. It is interesting to note that the experimental curve is very close to the ideal one for concentrations greater then x'=0.7. This would indicate that it is easier to grow mixed crystals of KDP and ADP on the ADP rich side of the phase diagram. This fact can be explained by considering the size of the interchanged ions. We will consider here three crystals RDP, ADP and KDP. The radii of the cations in those three crystals are: $R_{K^+} = 1.33$ Å, $R_{Rb^+} = 1.48$ Å, and $R_{NH_4^+} = 1.48$ Å [117]. Clearly substituting ammonium with rubidium does not cause any internal strains in the structure. However the ionic radius of NH_4^+ is about 10% bigger then that of potassium. Since it is easier to fit smaller ions in place of the bigger ones the solid solution of KDP and ADP is closer to ideal on the ADP side. Another measure of the strain induced by ion substitution is the relative difference in unit cell volume. Using the data from Table 1.1 it can be seen that the unit cell size mismatch is about 8% between KDP and ADP crystals and less then 1% for RDP-ADP system. As a rule of thumb, less than 15% difference in ionic radius or unit cell volume is

acceptable. Beyond that the solid solution will most likely not form. This is known as the Goldschmidt rule in inorganic chemistry.

3.2 Crystal Growing Setup

All measuring techniques used to investigate phase transitions in KDP-ADP solid solutions require relatively large, oriented samples in a single crystalline form. A seeded growth method was chosen to achieve this. It relies on the introduction of a small crystal, the seed, into a supersaturated solution. The free energy barrier, i.e. the difference in chemical potential, between ions in the solution and the seed is much lower than between the dissolved salt and any other parts of the apparatus in contact with the solution. Therefore deposition of new material occurs preferentially on the seed, thereby reducing the possibility of unwanted crystal deposition on the bottom of the crystal growing vessel, which when it occurs reduces crystal growth rate for a given supersaturation level due to large surface area of growing crystal.

As previously noted, in this work the slow evaporation technique of crystal growth was used. A photograph of the crystal growing apparatus is shown in Figure 3.4 and an accompanying schematic diagram in Figure 3.5. It consisted of a water bath built out of a thick walled glass tube (G), 21.6 cm outside diameter and 38.5 cm long, glued into a grove in a Plexiglas plate (B) by means of silicone sealant. In operating conditions it contained about 7.6 liters of distilled water. Its temperature was controlled with a MICROMEGA CN77000 Series Controller (model CN77R353) equipped with an 0 - 10 volts analog output which was proportional to the difference between the set point and the actual bath temperature which was determined using a platinum resistor (T). This signal was detected by an Internal Analog Programming Interface card installed in a HPD 30-10 Xantrex Power Supply. It was used as a power

source for a home made immersion heater (H) made of Nickel-Chromium heater wire (NI-60-032-50) in a form of a coil inserted in a glass tube. At the maximum output it was capable of delivering approximately 280 Watts.

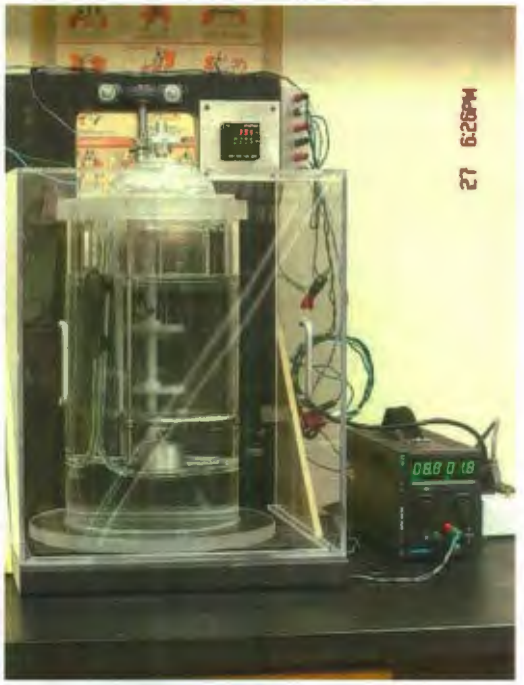

Figure 3.4: Crystal growing setup.

A layer of silicone oil (L1) was poured on top of the water bath to prevent excess evaporation. The large specific heat of water helps to achieve good temperature stability during the growth process. It was estimated that the temperature fluctuations were not greater then $\pm 0.025^{\circ}$ over a period of a week. To make the temperature distribution as uniform as possible a stainless steel stirrer (S) was used in the water. Its rotation speed was approximately 200 rpm.

A thick (1 inch) plexiglas lid (A) was tightly fitted on top of the thermostat container. It had a large opening in the middle to facilitate the removal of the crystal growing vessel (V). This hole was enclosed by a dome shaped lid (D) with a pulley (P1) arrangement mounted on top of it. P1 was used to transfer the rotational motion

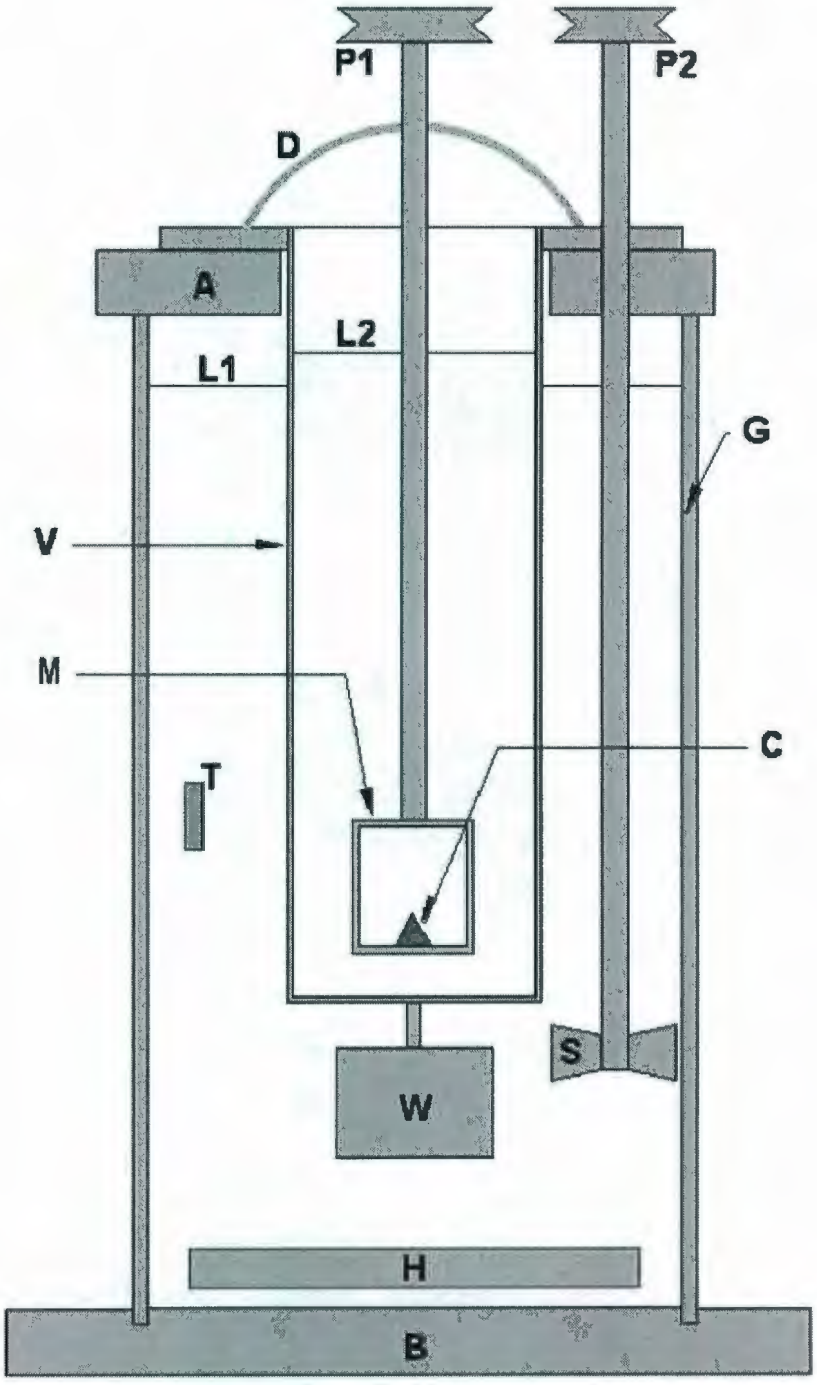

Figure 3.5: Schematic of crystal growing setup

from a motor to a stirrer which was temporarily installed during the overheating stage of the run (prior to seeding) and was also later used to rotate the crystal mounting stage (S) during the growth process (see below). The dome was perforated with several small holes to allow evaporated solvent to permanently escape the system while at the same time permitting solvent condensate to flow back into the crystal growth solution under gravity.

A saturated solution was placed in a 26 cm high beaker (V) made of a 10 cm diameter glass tube. Care was taken to use scratch free glass for that purpose since surface imperfections can act as nuclei for heterogeneous nucleation. It was supported by a triangular platform made of stainless steel and suspended in the thermostated water bath on three threaded rods (not shown in Figure 3.5). Its vertical position could therefore be adjusted. The vessel V was also stabilized against possible floatation by a weight (W) hung from its bottom surface. Typically about 2.5 liters of solution was used. Its level (L2) was always kept above the level (L1) of surrounding water bath.

After the solution was seeded a small DC electrical motor, driven by a PIC controller, was mounted directly on top of the plexiglas dome. It was used to rotate the seed holder (S) during the growth process at a speed of approximately 60 rpm. The direction of rotation was changed in a cyclic way. The seed was rotated one way for 15 seconds. The sense of rotation was then reversed over a period of 5 s and the seed was rotating in the opposite direction for another 15 s. This approach reduces the chance of development of a nutrient depleted zone near the surface of the seed which results in uneven growth rate.

3.3 Solution Preparation and Crystal Growth Procedure

All chemicals used in this work were purchased from Sigma-Aldrich company. They were all of ACS grade. Selected information regarding impurity content, as claimed by the supplier, density and formula weights are collected in Table 3.1. To overcome certain problems with crystal cracking during growth, believed to be caused by trivalent metal cation impurities, high purity ADP starting material was used in one case. It contained less then 100 ppm of all metal impurities. However, it did not make a significant difference. However it is still believed that using very high purity materials would solve that problem.

	KH_2PO_4	$(NH_4)H_2PO_4$
Assay	$\geqslant$99.0%	$\geqslant$98.0%
ρ $[g/cm^3]$	2.338	1.803
FW $[g/mol]$	136.09	115.03
K	-	$\leqslant$0.005%
Fe	$\leqslant$0.002%	$\leqslant$0.001%
Na	$\leqslant$0.005%	$\leqslant$0.005%
Cl-	$\leqslant$0.001%	$\leqslant$5 ppm
Heavy metals	$\leqslant$0.001%	$\leqslant$5 ppm
Insolubles	$\leqslant$0.01%	$\leqslant$0.005%

Table 3.1: Physical data and impurity content of chemicals used for crystal growth.

Every crystal growth run started with the preparation of a solution. The goal was to use approximately correct amounts of salts and water so that the resulting solution would be as close to the state of supersaturation as possible. Since the solubility data

for mixed $K_{1-x}(NH_4)_xH_2PO_4$ crystals was not available, the saturation point was determined experimentally each and every time prior to the beginning of a growth run.

Approximate amounts of ACS grade KH_2PO_4 and $(NH_4)H_2PO_4$ were dissolved in hot nanopure water. An attempt was made to purify the salts by means of the recrystallization. A hot solution was vigorously stirred until small crystals precipitated spontaneously. The solid was then separated from the solution and the process was repeated until there was no more then 200 ml of solution left. The leftover solution was discarded. In that process materials which were more soluble then the original salts were, at least partially, removed from the system. Purified material was also dissolved again for the second recrystallization stage. This time, after about 200 g of salt precipitated on the bottom of the beaker, the solid was discarded. In this case less soluble material was removed from solution. In principle this procedure should be repeated about five times to achieve high purity material. However, because it is a very wastefull process, it was decided against multiple recrystallization. It was carried just once for each composition. Finally, purified material was dissolved again and filtered while hot through a fritted funnel with fine pores.

Purified salt was dissolved again and poured into the crystallizer, which was preheated to the growth temperature. After several hours, when the temperature of the solution reached that of the thermostat, a small test crystal was introduced to determine if the solution is saturated. The level of solution was recorded at the point when the test crystals stopped dissolving. Then the temperature of the solution was raised by 10 K and the solution was preheated at that temperature for at least 24 hours. This process assured that even the smallest crystals present in the solution were dissolved prior to the seeding and growth phase.

The solution preparation procedure as described above was repeated twice, each

time for a solution containing different relative amounts of KDP and ADP. The ratio of KDP to ADP by weight was 5:1 for solution 1 and 1.875:1 for Solution 2. Assuming that the recrystallization process did not influence the solution composition the mole fraction of ADP in the solution was: $x_1 = 0.19$ and $x_2 = 0.39$.

The preheated solution was subsequently seeded with previously prepared small crystals. One particular batch of seeding material of a mixed composition was prepared by leaving saturated solution with ADP mol fraction $x_1 = 0.19$ at room temperature in a fume hood for several weeks. Spontaneously precipitated seed crystals were collected from the bottom of a beaker in this case. Pure KDP seeds were also used for growing crystals with small ADP content. The same seed preparation method, used for the solution with $x_2 = 0.39$ resulted in small crystals with a lot of visible cracks inside. They were not used for further crystal growth. Seeds for the solution with higher ADP content were prepared from mixed single crystals grown earlier.

Seeds in a form shown schematically in Figure 3.6 were mounted in a plexiglas platform which could be suspended in the solution from the axis of the DC motor. This arrangement mechanically isolated the seed's head from any residual stress resulting from hardened glue used to mount them. Stycast epoxy was used for that purposes. It was hard when dry and did not soften in hot water. At least 24 hours was allowed for the epoxy to dry. The platform was thoroughly washed prior to seed mounting.

Each solution was seeded at temperature few degrees higher then the saturation temperature. To avoid thermal shock all seeds were preheated just before being introduced into the solution. The simple equipment used for that purpose is shown in Figure 3.7. It consisted of a large beaker with a Plexiglas lid. The seed platform and a mercury thermometer were suspended from that lid as shown. The entire arrangement was placed on a hot plate. Approximately 500 ml of distilled water

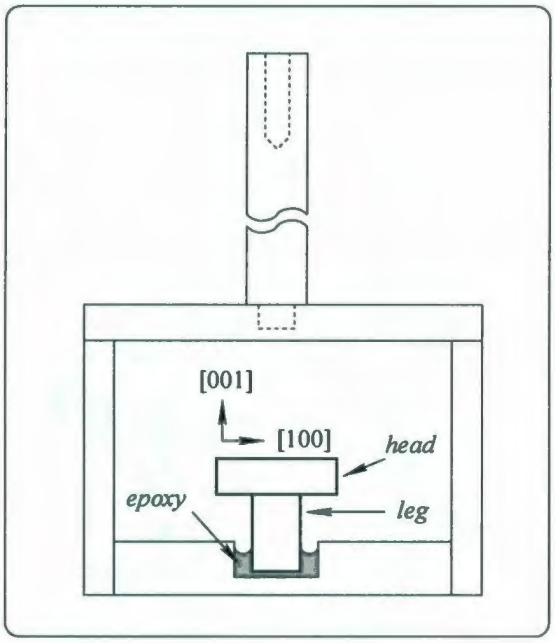

Figure 3.6: Crystal seed mounted in a plexiglass platform (schematic).

was placed in the beaker and brought almost to a boil. Hot water vapor was used to preheat the seed to about 56°C, which is about 6 degrees higher then the temperature at which the seed was introduced to the solution. The 6 degrees margin was applied to allow for cooling during transfer. A small glass cup was used to cover the seed to prevent any dissolution due to condensation. Every seed was allowed to dissolve to some extent prior to initiating crystal growth by lowering the temperature to the previously determined saturation point. This procedure removed any impurities present on the seed's surface. It also allowed for removal of the strained outer layer of material resulting from prior cutting and grinding.

After seeding the solution, its temperature was reduced to about 1 degree above the saturation point. The platform was not rotating during that process to avoid excessive seed dissolution. Then the solution was slowly cooled down in steps of 0.2 degrees. The seed was observed for any signs of growth for about 30 minutes. Once

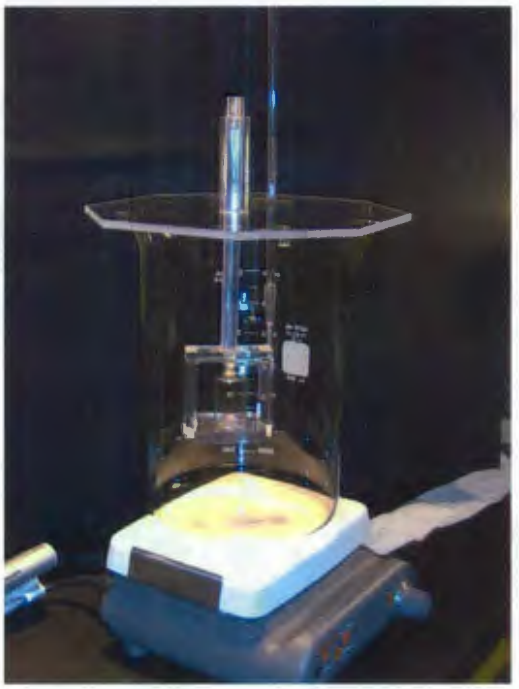

Figure 3.7: Seed preheating setup.

the growth was initiated the temperature was further lowered by about 0.2°. The seed was allowed to regenerate at that temperature. Typically it took anywhere from 10 to 48 hours to complete that process depending on the supersaturation level. The regeneration was completed when all natural crystal faces were fully developed at which point the growth started. Depending on the required size, the growth process took from 4 to 6 weeks. The growth rate was estimated to be approximately 0.5 mm per day in the [001] direction.

After the crystal reached sufficient size it was taken out of the crystallizer for further experiments. KADP mixed crystals grow in the form of a tetragonal bipyramid elongated in the [001] direction. The morphology of growing KDP crystal (the same as for KADP) is schematically shown in Figure 3.8. The growth rate of prism faces is approximately 10 times lower then that of pyramid faces. This difference is attributed to the rather large affinity of trivalent metal cations (Cr^{3+}, Al^{3+} and Fe^{3+})

for attachment to prism faces. Those inclusions modify crystal growth habit rather dramatically as shown in [115, 116]. The most visible effect of the existence of those defects is a tapering of prismatic faces. The amount of those cations required to cause them can be as small as few parts per million. The estimated concentration of Fe^{3+} cations in the present growth solutions, based on chemical supplier information (see Table 3.1), is between 50 and 70 ppm. Despite the fact that the supersaturation level

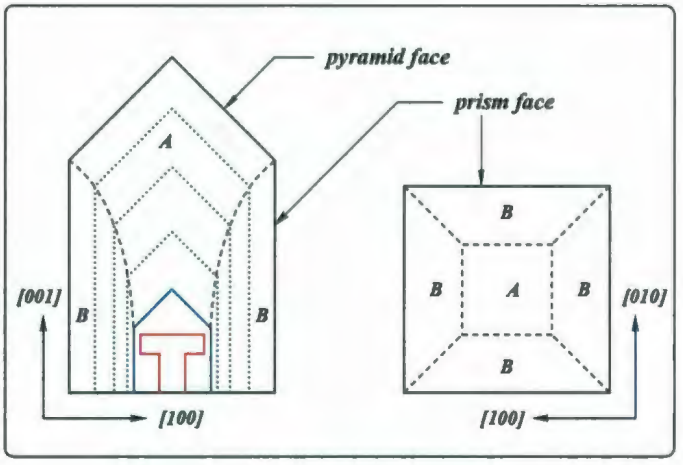

Figure 3.8: Schematic representation of subsequent growth stages of KDP type crystals. Red outline indicates original seed, blue outline indicates regenerated seed. Pyramid (A) and prismatic (B) growth sectors are also indicated.

was kept low at all times to reduce chances of cracking it could not be avoided. Only in one case was a single crystal without any visible defects obtained. It was grown from a solution with $x = 0.19$. The severity of damage was larger at higher ADP concentrations. Typically first cracks would appear at the growth sector boundaries after the newly grown layer reached a few millimeters in thickness. It is believed that chemical impurities were its main cause. However it is also possible that a slight difference in composition between seed and the grown crystal could also result in mechanical damage to the crystals. Fortunately, it was always possible to find clear,

good quality regions of sufficient size from which samples for subsequent studies could be prepared. It was not unusual for the cracks to propagate into the clear undamaged regions in the process of crystal cutting (described later). Due to the above mentioned difficulties in obtaining crack-free crystals only two compositions of the KDP-ADP solid solutions were prepared for this thesis.

3.4 Crystal Composition

The composition of the mixed crystal is the most important parameter which has to be determined in order to compare any other experimental results with published work. As already mentioned, KADP mixed crystals do not have the same composition as the solution from which they were grown. Moreover, the process of recrystallization described earlier changes the relative amounts of both salts in the solution. Although this effect was minimized by the relatively large volume of solution used it was decided to determine the relative concentration of the two end members in the solid solution experimentally. For the purposes of this thesis the concentration was measured in two separate ways. The first was a chemical analysis performed by Canadian Microanalytical Service Ltd (CMS) located in Delta, British Columbia. Two samples were analyzed. One grown from a solution prepared from dissolving KDP and ADP crystals in a ratio 5:1 by weight (referred here as KADP1) and another one with KDP to ADP ratio 1.875:1 (referred here as KADP2). The samples were analyzed by combusting them at about 1050°C, reduction of NO_x gasses, and separation of the resultant N_2, CO_2, and H_2O by gas chromatography. The above procedure was used to measure N and H content. Acetanilide (C_8H_9NO) and 4-Nitroanaline ($C_6H_6N_2O_2$) were used as standards.

The amount of K, on the other hand, was determind by means of a Inductively

Coupled Plasma Atomic Emission Spectroscopy (ICP-AES) technique. It measures the intensity of a characteristic radiation emitted from a sample, prepared in the form of a solution.

The results obtained are presented in Table 3.2. They are expressed in weight percent and the absolute experimental uncertainty associated with those measurements is 0.3%. Using the values presented in Table 3.2, the composition of the crystals can

	N	K	H
KADP1	< 0.3	29.0	1.55
KADP2	1.39	26.0	1.95

Table 3.2: Weight percent content of nitrogen, potassium and hydrogen in two of the studied mixed crystals.

be expressed in mole fractions. In principle, data from each column of Table 3.2 can be used for that calculation. However, the weight fraction of K in the pure KDP crystal is 28.7% which is smaller then the amount of potassium in the KADP1 crystal determined experimentally. Clearly the method used was not accurate enough to give reliable values for small x. Therefore for this crystal only the hydrogen data can be used for determination of the crystal composition. The molar mass of a solid solution $K_{1-x}(NH_4)_xH_2PO_4$ can be written as

$$M_{\mathrm{KADP}} = (1-x)M_{\mathrm{K}} + xM_{\mathrm{NH_4}} + 2M_{\mathrm{H}} + M_{\mathrm{PO_4}} \tag{3.14}$$

where M_{X} stands for molar mass of chemical entity X. The weight fraction of hydrogen for example can now be written as

$$W_{\mathrm{H}} = \frac{4xM_{\mathrm{H}} + 2M_{\mathrm{H}}}{M_{\mathrm{KADP}}} \tag{3.15}$$

The above relation can be solved for x. Equations similar to Equation 3.15 can be constructed for each element in the chemical formula of the crystal. The results of

this calculation, together with similar data for the solution from which a given crystal was grown, are shown in Table 3.3. The estimated relative uncertainty in those values is not greater then 10%.

	N	K	H
KADP1	< 0.029	-	0.020
KADP2	0.132	0.111	0.142

Table 3.3: Mole fractions calculated from weight fractions for different mixed crystals studied.

Because of the limitations of the methods used to obtain data presented above, and relatively large uncertainties associated with those measurements, as indicated above, it was decided to collect X-ray powder diffraction spectra for the crystals used in this study and to determine their unit cell parameters. In addition to the mixed crystals, spectra for pure end members were also collected. Composition determination from those data relies on a linear dependence of the c unit cell parameter on x as shown by Ono et al. [2]. The analysis is simplified by the fact that KADP crystallizes in the same crystallographic system as pure KDP.

The samples used for X-ray data collection were prepared in a form of a fine powder by means of manually grinding them under methanol. They were then mounted in a holder which consisted of an aluminum plate with a $20 \times 20 \times 2$ mm cavity. This mounting technique maximizes scattered beam intensity and reduces any background resulting from X-ray scattering from Aluminum [118]. Diffraction patterns were collected using $\mathrm{Cu}-K\alpha$ radiation ($\lambda = 1.5406$ Å) from a Rigaku RU-200 rotating anode, automated diffractometer operated at 40 kV and 100 mA in the Department of Earth Science (Memorial University of Newfoundland). It was operated in a continuous scan mode at scanning rate of $1\,^\circ$/min. in a range $15\,^\circ < 2\theta < 100\,^\circ$. Figure 3.9 shows

the X-ray diffraction patterns obtained. Full Rietveld refinement [119] of the crystal structures was attempted using the MAUD (Material Analysis Using Diffraction) program [120]. This technique is a fitting routine which, based on the assumed model of a structure, adjusts the unit cell parameters and the atomic positions to minimize the residual function defined as

$$WSS = \sum_{i=1}^{N} \left[w_i \left(I_i^{exp} - I_i^{calc} \right) \right]^2 \tag{3.16}$$

where I_i^{exp} and I_i^{exp} are the experimental and calculated intensity profiles respectively and the weight factors is $w_i = 1/I_i^{exp}$. The sum runs over the number of data points collected for a given diffraction pattern. The calculated intensity is expressed as

$$I_i^{calc} = S_F \sum_k L_k |F_k|^2 S\left(2\theta_i - 2\theta_k\right) P_k A + I_{bkg} \tag{3.17}$$

where S_F is the beam intensity, L_k - a Lorenz polarization factor, F_k - a structure factor, $S\left(2\theta_i - 2\theta_k\right)$ - peak shape profile, P_k describes texture, A is an absorption factor and I_{bkg} is a background factor typically approximated by a simple polynomial. Parameters S_F, L_k, and $S\left(2\theta_i - 2\theta_k\right)$ are specific for a given instrument. The F_k factor depends on the position of atoms in the unit cell, their kind, reflection multiplicity and the temperature factor. The P_k term accounts for the difference in calculated and experimental intensity due to the preferred orientation, if any, of the crystalline grains in the sample and becomes especially important if the material studied has a cleavage plane.

Two parameters are defined for the purpose of describing how well a given structural model represents collected dataset. First

$$R_{wp} = \sqrt{\frac{WSS}{\sum_{i=1}^{N} \left[w_i I_i^{exp} \right]^2}} \tag{3.18}$$

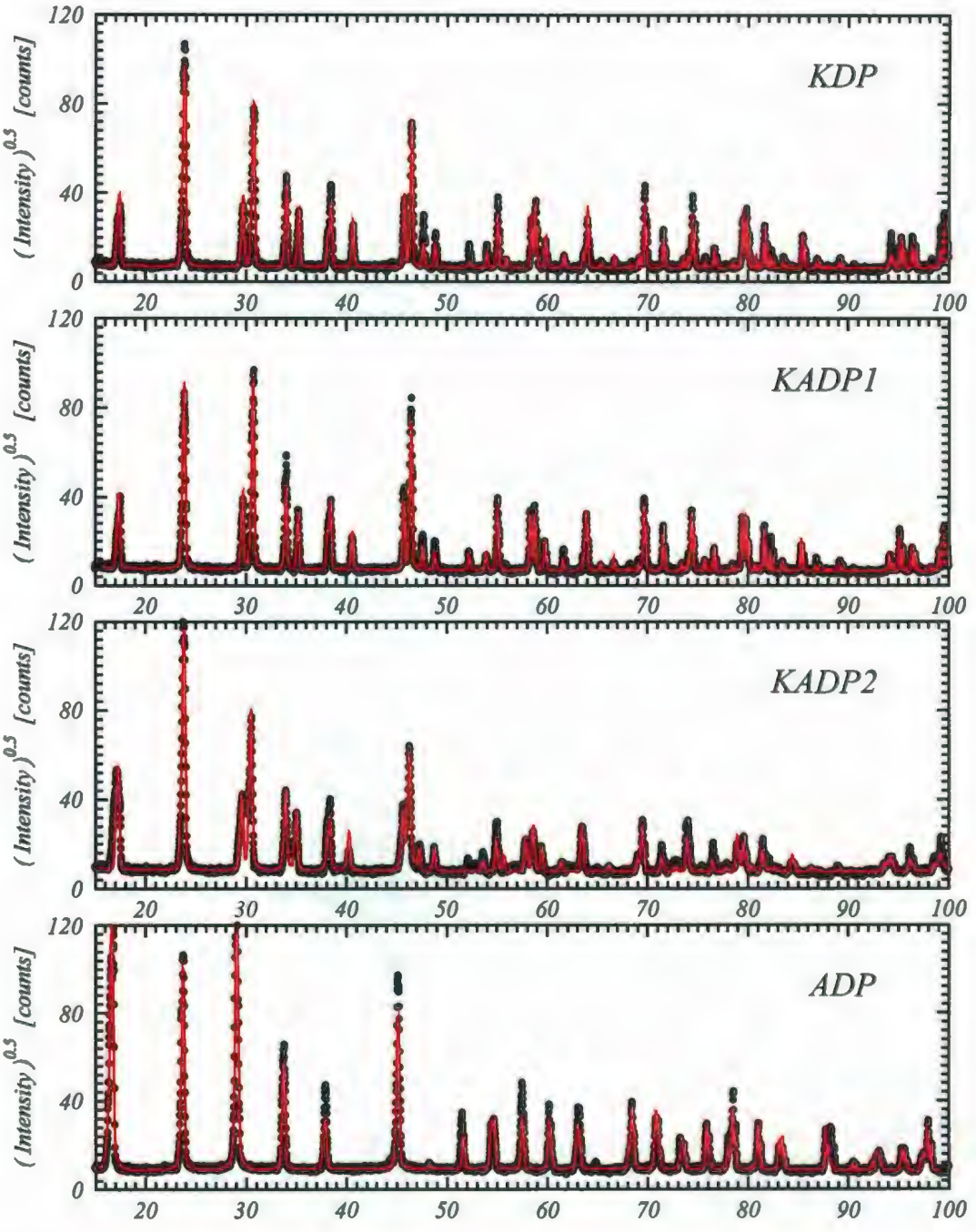

Figure 3.9: X-ray diffraction patterns for all crystals studied. Solid lines represent the refinement results.

in which all the parameters has been already defined, and second

$$R_{exp} = \sqrt{\frac{(N-P)}{\sum_{i=1}^{N}[w_i I_i^{exp}]^2}} \tag{3.19}$$

where P is the number of adjustable parameters in the model. The overall goodness of fit is described by

$$GofF = \frac{R_{wp}}{R_{exp}} \tag{3.20}$$

It is generally accepted that $GofF$ values of 2 and less indicate good refinement. However it cannot be smaller then 1.

Refinement of the unit cell parameters for pure KDP and ADP crystals was performed based on well known structural data available for those two compounds. Most of recorder reflections (87 for KDP and 96 for ADP) were accounted for by the model. For the mixed crystals studied KDP structure was also used as a starting point but the occupancy of potassium site was set as a parameter. The results of the refinement are presented in Table 3.4. Parameters describing the quality of the refinement, as well as K site occupancy x are also included.

Crystal	a [Å]	c [Å]	ρ [g/cm^3]	R_{wp} [%]	R_{exp} [%]	$GofF$
KDP	7.454	6.975	2.306	24.7	7.4	3.3
KADP1	7.458	6.987	2.270	23.6	7.2	3.3
KADP2	7.467	7.044	2.216	33.5	6.4	5.2
ADP	7.502	7.546	1.831	30.9	5.3	5.8

Table 3.4: Unit cell parameters and densities of crystals studied as determined by X-ray analysis. Some parameters describing goodness of fit are also included.

As can be seen from above table the quality of the fit was rather low. This is attributed to the existence of another phase in our samples. This hypothesis is sup-

ported by the fact that certain reflections did show splitting indicating the symmetry of that phase to be lower than tetragonal. In fact, its existence in pure KDP crystals has been reported by Suvorova [121, 122] based on the transmission electron microscope experiments. She showed the existence of regions, up to 4500 Å in diameter and located near lattice defects, the symmetry of which is most likely orthorhombic. They are a direct consequence of the strain field associated with the foreign atoms incorporated randomly in the crystal structure during the growth process [123]. The amount of that phase, as reported by Suvorova in [121], can be between 1.5% and 5% of the sample volume. The proposed space group symmetry of those inclusions is Aba2 or Ama2. Both of them were tried in an attempt to improve the refinement of our difraction data but all attempts were unsuccessful. It is believed however that the data presented in Table 3.4 adequately represent the tetragonal phase which is of primary interest for this work. It should be mentioned that, to the best of our knowledge, there is no reports available in the scientific literature indicating the existence of such regions in pure ADP crystals.

Using data from Table 3.4 for KDP and ADP crystals only, and assuming linear relation between c and crystal composition we arrive at the following empirical relation between those two quantities

$$c = 0.571x + 6.975 \tag{3.21}$$

Using the above equation the molar fraction of the mixed crystals was calculated. The results are: $x_1 = 0.021$ and $x_1 = 0.121$ for KADP1 and KADP2 crystals, respectively. Those values agree reasonably well with the data obtained from chemical analysis presented in Table 3.3.

In the following sections of this thesis a new designation of the samples of the KDP-ADP solid solution of the form KADP : x will be adopted. In that symbol the

percent mole fraction of the NH_4 ions will be substituted for x. Therefore KADP1 gets replaced with KADP:2.1 and KADP2 - with KADP:12. Those symbols are more convenient because they explicitly reflect the composition of the samples as determined experimentally.

NEWTON'S THREE LAWS OF GRADUATION

Having postulated the first two Laws of Graduation, Isaac Newton the grad student was still perplexed by this paradox: If indeed the first two Laws accounted for the forces which delayed graduation, why doesn't explicit awareness of these forces allow a grad student to graduate?

It is believed that Newton practically abandoned his graduate research in Celestial Mechanics to pursue this paradox and develop his Third Law.

THIRD LAW

"For every action towards graduation there is an equal and opposite distraction"

This Law states that, regardless of the nature of the interaction with the advisor, every force for productivity acting on a grad student is accompanied by an equal and opposing useless activity such that the net advancement in thesis progress is zero.

Newton's Laws of Graduation were ultimately shown to be an approximation of the more complete description of Graduation Mechanics given by Einstein's Special Theory of Research Inactivity.

Einstein's theory, developed during his graduate work in Zurich, explains the general phenomena that, relative to the grad student, time slows down to nearly a standstill.

PHD.STANFORD.EDU

JORGE CHAM ©THE STANFORD DAILY

Pile Higher and Deeper

by Jorge Cham

www.phdcomics.com

Chapter 4

Experimental Details

4.1 Sample Preparation

Pure KDP crystals were kindly provided by Dr. Bogusław Mróz from the Department of Physics, Adam Mickiewicz University in Poznań, Poland whereas the KDP-ADP solid solutions were grown by the author. All of the crystals were of good quality. There were no visible defects or inclusions present.

For Brillouin spectroscopic measurements all the samples were prepared in the shape of a cuboid with the edges several millimeters in length. They were cut from a single crystal with a wire saw. Their orientation was chosen so that the soft acoustic mode could be observed and was based on the morphology of the crystals. It is believed not to deviate from that assumed by more than 1 degree. Sample faces were initially ground flat with #600 and #1200 grit abrasive powder mixed with glycerin and subsequently polished manually to optical quality to minimize scattering of incident light at surface imperfections. Samples were placed in the cryostat (described below) and held at a given temperature for 20 - 30 minutes prior to the beginning of spectrum accumulation.

The same samples were used for dielectric constant and for piezoelectric resonance measurements. They were in a form of rectangular or circular plates with the largest faces perpendicular to the [001] crystallographic direction. Rectangular plates had edges parallel to the [100] and [010] crystallographic directions or at 45 degrees to them. All of the samples were at most 1 mm thick. Their largest faces were gold coated to provide electrical contact. Care was taken to remove any gold from the edges of the samples to avoid short circuit between two electrodes.

4.2 Cryogenic System

For all experiments a commercial, two-stage, closed-cycle helium refrigeration system was used to cool samples to the desired temperature. For Brillouin measurements it consisted of a compressor model HC-2 coupled with a two stage expander unit model DE202 by *Air Products*. Its first stage was fitted with a highly polished copper radiation shield. It was all enclosed in a brass vacuum shroud equipped with four windows on two orthogonal axes to allow for the passage of the incident and scattered light. A specially made brass sample holder, schematically represented in Figure 4.1, was mounted at the end of the second stage of the expander module. Good thermal contact between the two was maintained by means of thin indium washer and a copper infused vacuum grease applied between the two. During the experiment the sample was kept in high vacuum provided by a mechanical pump connected in series with a diffusion pump. The pressure maintained inside the chamber was of the order of 10^{-6} torr. A cryogenic temperature controller (LakeShore Cryotronics, model DTC-500) was used to stabilize sample temperature throughout the spectrum accumulation time. A silicon diode (DT-470) served as the temperature sensor and was mounted in the base of the sample holder. The power output from the controller was connected to

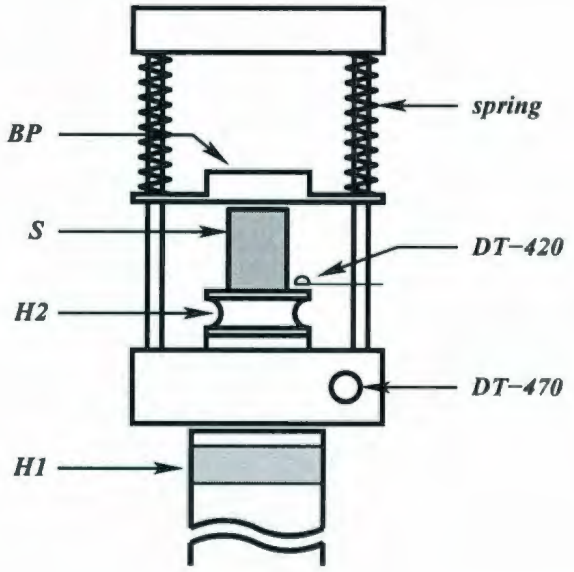

Figure 4.1: Sample holder for Brillouin spectroscopy.

a home made, miniature, 10 ohm heater (H2) wound from manganin wire on a small brass bobbin. It was placed directly below the sample (S). An additional heater (H1), mounted already by the manufacturer at the end of the second stage of the expander module, was used to bring the sample close to the desired temperature. It was powered directly from a Xantrex Power supply (model 30-10) capable of delivering 10 A at 30 V with an appropriate load. Moreover, an additional miniature silicon diode (DT-420) was mounted a few millimeters away from the crystal to measure its temperature. Its very small size assured very fast response time. Long term temperature stability was achieved with that system. It was not unusual to observe an overnight sample temperature drift of less than 0.05 K. The crystal was held in place by clamping it with a spring loaded brass plate (BP). This was necessary to prevent it from falling off the sample holder due to vibrations of the expander module.

4.3 Brillouin Spectrometer

Two setups were used to collect Brillouin data presented in this thesis. First, in the Department of Physics and Physical Oceanography at Memorial University of Newfoundland employed piezoelectrically scanned, five-pass Fabry-Perot interferometer (FP) (Burleigh RC 110). It was equipped with two dielectric mirrors with 93% reflectivity coefficient and flat to $\lambda/200$. The green line of an Ar^+ ion laser (Spectra Physics Series 2000, λ=514.5 nm) operating in a single mode arrangement was used as an excitation source.

Second, in the Department of Physics at Adam Mickiewicz University in Poznań (Poland) was based on the commercial 3+3 pass tandem system originally designed by J. R. Sandercock [124]. It provided better contrast which allowed data collection for the KADP2 sample below 50 K as discussed in Section 5.2. It was impossible to collect data below that temperature with the original setup due to very intense elastically scattered light. The light of a wavelength 532 nm from a diode pumped solid state Nd : YAG laser by Coherent (model DPSS 532 - 100) was used as an excitation source in this case. In both cases the output power was maintained below 100 mW to avoid heating of the sample at low temperatures.

The schematic drawing of the optical setup at Memorial University is shown in Figure 4.2. Its general features are common to both experimental setups mentioned earlier and the differences will be described later. The laser beam was first passed through a thick, good optical quality glass blank (represented in Figure 4.2 as two beam splitters BS for clarity). This resulted in the appearance of multiple reflections of the different surfaces of the slab of progressively weaker intensity. The transmitted beam (B1) served as the excitation source since it had the highest intensity. The first reflection (not showed in Figure 4.2) served as a reference beam for initial alignment

purposes and was co-linear with the optical axis of the spectrometer. Two other reflections were used for monitoring laser output for single mode operation (B2) and as a reference beam (B3). The intensity of the central spectral line of B3 is used in a feedback loop to help keep the two Fabry-Perot mirrors parallel to each other during long hours of spectrum acquisition. Therefore it is important that the power level of the reference beam is constant. The Computerized Data Acquisition System (CDAS) used for operating the interferometer and data collection was capable of driving two external shutters SH1 and SH2. SH1 blocked the incident beam (B1), while SH2 simultaneously admitted the reference beam (B3) in the middle of the Fabry-Perot mirror scan, i.e. when the unshifted Rayleigh line was analyzed. This allowed for continuous operation of the system even without a sample in place. The single mode operation of the argon ion laser was continuously monitored by a Model 470 Optical Spectrum Analyzer (OSA) (confocal Fabry-Perot) with 8 GHz spectral free range, connected to an oscilloscope (OSC) and driven by Model 476 scanning interferometer driver both by Spectra Physics Inc.

The main laser beam (B1) was always polarized perpendicular to the scattering plane. This direction coincided always with the [010] crystallographic direction inside the specimen and allowed for the observation of the soft mode as discussed earlier. The incident beam was focused on the sample by lens L_1 (f=25 cm). The beam was directed to the beam trap (BT) after passing through the sample. Light scattered at right angles to the incident beam was collected by a lens L_2 (f=10 cm) positioned at its focal length away from the scattering volume. This produced a parallel beam whose diameter was controlled by a diaphragm (D) set directly behind the collecting lens. Changing its diameter allowed for changing the collection angle if necessary. Most of the time it was set to 10 mm. This collimated beam of scattered light was passed through a special filter consisting of lens L_3 (f=20 cm), a pinhole P_1 (d=400 microns)

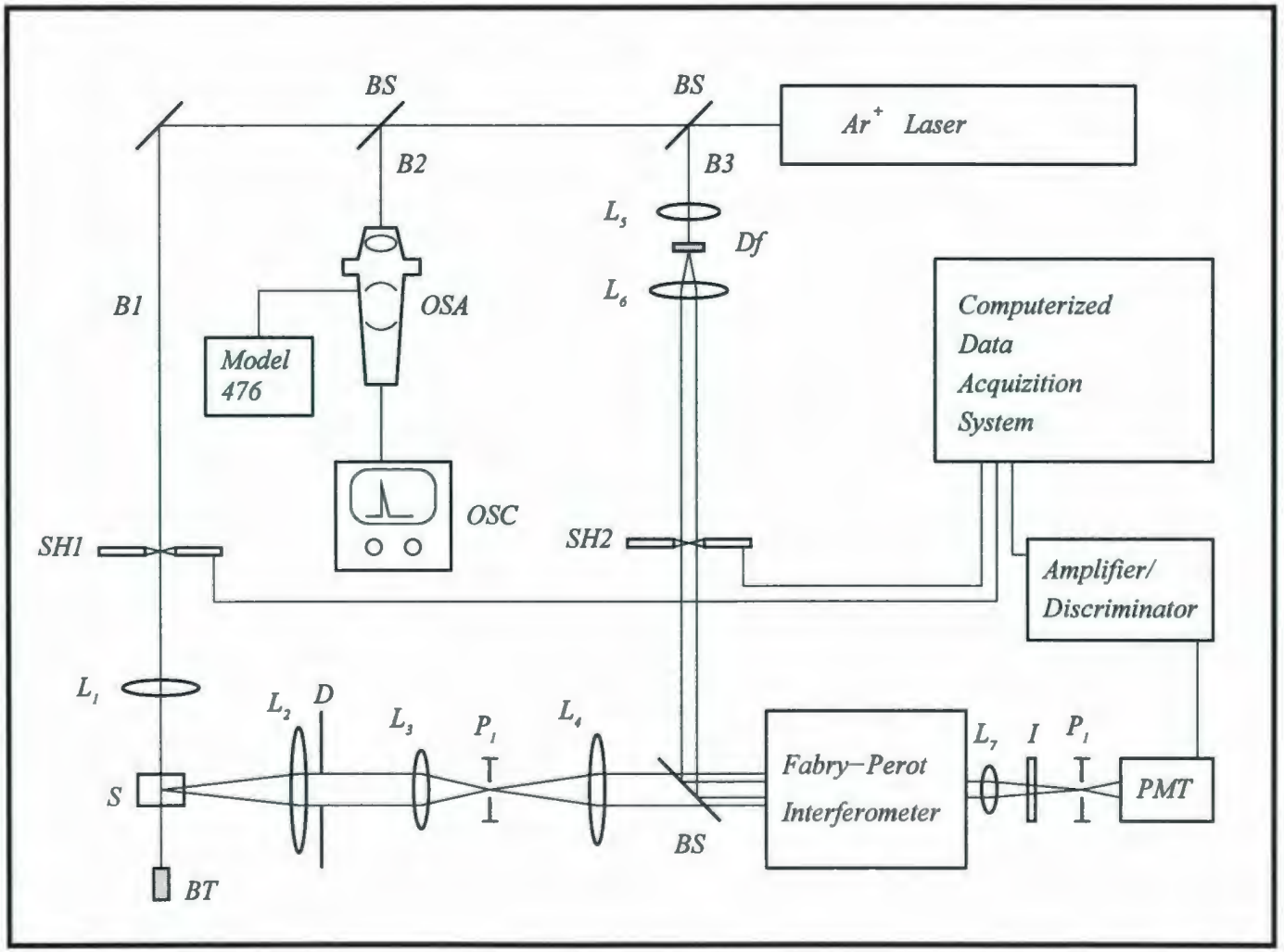

Figure 4.2: Experimental setup for Brillouin spectroscopy

and a lens L_4 (f=10 cm). A sharp image of the beam inside the sample could be obtained on the pinhole P_1 which helped to achieve accurate alignment. The scattered light passed through the Fabry-Perot interferometer and was subsequently focused by lens L_7 (f=9 cm) on the entrance pinhole P_1 (d=200 microns) of the water cooled photomultiplier tube (PMT) (ITT FW 130) operating in a photon counting mode. A narrow band pass filter (I) (band width = ±10nm) was positioned right after the interferometer to eliminate any light outside of the Brillouin spectral range. Each photon impacting a photocathode produces a pulse of electrons. This pulse train is then selectively amplified in Amplifier/Discriminator (Princeton Applied Research SSR 1120). Only pulses of certain height determined by manually adjusted discrimination level, appear on its output. This signal is sent to a digital counter controlled by a computer and synchronized with the Fabry-Perot mirror scan. The spectrum is stored in a 640 multichannel memory. Various parameters controlling the interferometer can be set up using FPDACS software. Some of them include the duration of the mirror scan (dwell time), the position and width of a control window for active feedback control, the step size in which the mirror tilt is adjusted etc.

The entire optical setup was positioned on a $1/2''$ steel table. All optical components were mounted on magnetic bases or on a optical track, to prevent accidental misplacement. Moreover, the interferometer, the lens L_7, pinhole P_2, and a PMT were shielded from the ambient light to minimize the background count.

4.4 Fabry-Perot Interferometer

The principles of operation of the Fabry-Perot interferometer are based on the phenomenon of multiple beam interference. The active element in this case is a set of two mirrors characterized by a reflectivity $\mathcal{R}$ and transmission coefficient $\mathcal{T}$. The

interfering beams are of diminishing intensity and result from multiple reflections between the mirrors. It can be shown [125] that the transmitted intensity of light can be described by the formula

$$\frac{I_t}{I_0} = \frac{1}{1 + F\sin^2\left(\frac{\delta}{2}\right)} \tag{4.1}$$

where I_t and I_0 represent the transmitted and incident intensities respectively, δ is a phase difference between subsequent transmitted beams, and F is the coefficient of finesse and is only a function of the surface reflectivity. It is equal to

$$F = \frac{4\mathcal{R}}{(1-\mathcal{R})^2} \tag{4.2}$$

It is clearly evident that the higher the reflectivity the narrower the transmission peaks. The transmission maxima appear when

$$\frac{\delta}{2} = m\pi \tag{4.3}$$

for integer values of m. The phase difference, δ, due to optical path difference between two consecutive transmitted beams can be expressed as

$$\delta = \frac{4\pi nd\cos(\theta)}{\lambda} \tag{4.4}$$

where n is the index of refraction of the material between the mirrors, d is the mirror separation and θ is the angle of incidence. Substituting this into Equation 4.1 and assuming normal incidence we obtain

$$\frac{I_t}{I_0} = \frac{1}{1 + F\sin^2\left(\frac{2\pi nd}{\lambda}\right)} \tag{4.5}$$

The above formula shows that by changing the index of refraction or the separation between the plates we can create a constructive interference condition for different wavelengths.

An example spectrum calculated using Equation 4.5 for a case when the incident light consists of three wavelengths (λ, $\lambda+\delta\lambda$ and $\lambda-\delta\lambda$) is shown in Figure 4.3. The distance between two subsequent transmission maxima in frequency (or wavelength) units is called the *Free Spectral Range* (FSR) and can be determined from Equations 4.3 and 4.4. The result is

$$FSR = \frac{c}{2nd} \tag{4.6}$$

where normal incidence was assumed.

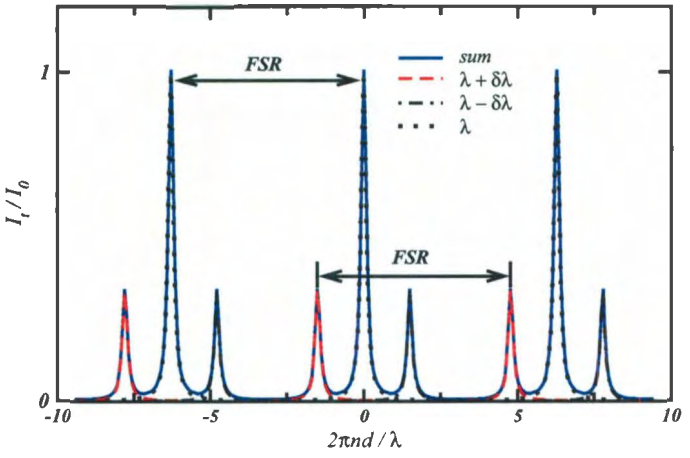

Figure 4.3: Theoretical Brillouin spectrum consisting of three different wavelengths (F = 400).

Two other parameters are used to describe the performance of the FP interferometer. Contrast, defined as the ratio of maximum and minimum transmission i.e

$$C = \frac{\left(\frac{I_t}{I_0}\right)_{max}}{\left(\frac{I_t}{I_0}\right)_{min}} = 1 + F = \left(\frac{1+\mathcal{R}}{1-\mathcal{R}}\right)^2, \tag{4.7}$$

and finesse $\mathcal{F}$ which is defined as a ratio of FSR to the *full width at half maximum* (FWHM) of the transmission peak and is given by

$$\mathcal{F} = \frac{\pi\sqrt{F}}{2} = \frac{\pi\sqrt{\mathcal{R}}}{1-\mathcal{R}}. \tag{4.8}$$

It is clear from the above discussion that a spectrometer with higher finesse will have better resolving power. The most commonly used technique to improve a single spectrometer's finesse for a given mirror reflectivity is to arrange it in a multipass mode. If m is the number of passes then the finesse and contrast parameters are the m-th power of the appropriate values of the instrument operating in a single pass. The increase in resolving power was demonstrated for the first time in 1961 by Hariharan *et al.* for m=2 [126].

Much superior performance of the Fabry-Perot interferometer is achieved by arranging two FP etalons in series. However, it is difficult to synchronize the scans of the two sets of mirrors [127]. This problem was solved by Sandercock [128] by mounting the two moving mirrors on a common stage and arranging them in such a way that their optical axis make an angle ϕ. Scanning the common stage results then in different scan amplitude for the two FP interferometers which in turn increases the effective FSR [129]. It should be mentioned that the above formulas are for an ideal case of perfectly flat mirrors and without an absorption effects. It is easy to imagine that imperfections of the surface will change interference conditions locally inside FP etalon. This will introduce a limit for the finesse of the instrument. The details are outside of the scope of this thesis and can be found in the literature [130]. In practice interferometer performance parameters are determined experimentally.

4.5 Dielectric and Piezoelectric Measurements

4.5.1 Dielectric Measurements

Measurements of the dielectric constant presented in this thesis were performed in Molecular Crystal Division of the Institute of Physics in Poznań (Poland) with the

permission of Dr. Piotr Czarnecki, its head, and under the supervision and with a great help from Dr. Maciej Wiesner. The measurements were fully automated and consisted of measuring sample capacitance as well as the tangent of the loss angle. Those parameters were measured using a low frequency Impedance Analyzer (HP 4192A) capable of measuring in a frequency range between 5 Hz and 13 MHz. The sample was cooled inside a closed cycle He refrigerator. All the experimental conditions (measuring field, frequencies, temperature ranges, rates of cooling or heating) were set in a computer program which was interfaced with the temperature controller and the impedance meter through a GPIB interface.

The capacitance of a parallel plate capacitor filled with a material with dielectric constant ε_r is given by

$$C = \frac{\varepsilon_0 \varepsilon_r A}{d} \tag{4.9}$$

where A is the area of the electrodes and d is the capacitor thickness. The above formula is used to calculate the values of ε_r at each temperature.

4.5.2 Piezoelectric Measurements

It was discovered in 1880 by the brothers Curie [131] that an electric charge appears on the surfaces of certain crystals while applying an elastic stress to them. One year later it was proposed by Lippmann [132] on a thermodynamics basis that the same crystals should deform under the application of an electric field. The former phenomenon is known as a direct, and the latter as a converse, piezoelectric effect which can be described by the following tensor formulas

$$P_i = d_{ijk}\sigma_{jk} \tag{4.10}$$

$$\epsilon_{jk} = d_{ijk}E_i \tag{4.11}$$

where d_{ijk}, σ_{jk}, and ϵ_{jk} are components of piezoelectric modulus, stress and strain tensors, respectively. It is the converse effect which is frequently employed to measure elastic properties of crystals in the kHz range simply because it is easier to apply an electric field to a sample rather than elastic stress. Because the strain tensor is symmetric under the exchange of the indices so is the d tensor and that means that it has 18 independent components. Moreover, crystal symmetry reduces that number even further. Therefore, Equation 4.11 can be written as

$$\epsilon_j = d_{ij} E_i \tag{4.12}$$

where the index i has a range from 1 to 3 and j from 1 to 6. The piezoelectric tensor for the point group $\bar{4}$2m takes the following form

$$\mathrm{d}_{\bar{4}2\mathrm{m}} = \begin{bmatrix} 0 & 0 & 0 & d_{14} & 0 & 0 \\ 0 & 0 & 0 & 0 & d_{14} & 0 \\ 0 & 0 & 0 & 0 & 0 & d_{36} \end{bmatrix}. \tag{4.13}$$

Therefore application of an electric field parallel to the [001] direction gives

$$\epsilon_6 = d_{36} E_3, \tag{4.14}$$

and application of a time varying electric field in that direction will induce a time varying elastic wave associated with the ϵ_6 stress component. The principle of piezoelectric measurements relies on the fact that for a sample cut in the shape of a rod, when any of the dimensions of the sample are a multiple of $\lambda/2$ (λ is an acoustic wavelength) the system will show a resonant behaviour. Therefore using an appropriate solution to the Cristoffel's Equation 2.8 it can be shown that the resonant frequency is given by

$$f_r = \frac{1}{2l}\sqrt{\frac{c_{66}}{\rho}} \tag{4.15}$$

where l is an appropriate sample dimension. Since the resonance frequency f_r is inversely proportional to the sample dimension the lowest resonance will correspond to an acoustic wave propagating along the longest sample dimension. Therefore the acoustic wave velocity can be easly determined.

The behaviour of a piezoelectric transducer driven by a sinusoidal electric field can be analyzed by an equivalent electrical circuit which is shown in Figure 4.4 [3, 133, 134]. The equation describing its behaviour has the form of a driven, damped harmonic oscillator, i.e.

$$L\frac{d^2I}{dt^2} + R\frac{dI}{dt} + \frac{I}{C} = \omega V \cos(\omega t) \tag{4.16}$$

where L, R, C, I and V are the inductance, resistance, capacitance, current flowing through the circuit and the driving voltage amplitude respectively. All those parameters can be expressed by a combination of material constants like elastic and dielectric constants, density etc. Figure 4.4 shows that the equivalent circuit is a

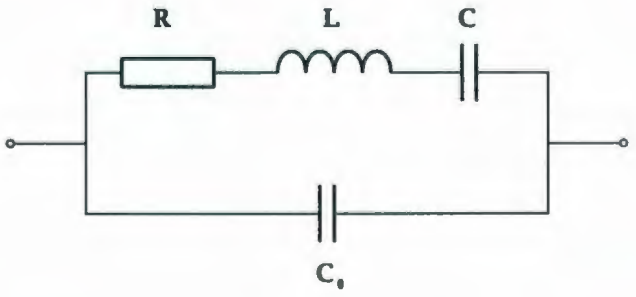

Figure 4.4: Equivalent circuit of the pizoelectric resonator.

combination of the parallel and series LC resonant circuits. Standard analysis can be applied to study its behaviour. The current flowing through the network will be at its maximum value when its reactance is zero and will have a minimum when its admittance is zero. Those two conditions give the expressions for the resonance, and

antiresonance frequency in the following form

$$\omega_r = \sqrt{\frac{1}{LC}} \tag{4.17}$$

$$\omega_a = \sqrt{\frac{C + C_0}{LCC_0}} \tag{4.18}$$

where C_0 represents the resonator's capacitance far away from any resonances. The frequency dependence of the electrical current flowing in the equivalent circuit is schematically shown in Figure 4.5 [135]. In principle it is possible to measure all

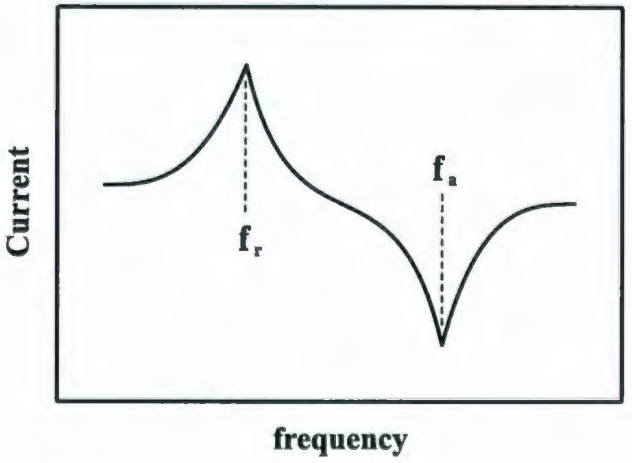

Figure 4.5: Current flowing through a piezoelectric resonator as a function of frequency.

the values of the parameters characterizing all the elements of the equivalent circuit which in turn allows one to calculate certain material parameters characteristic of the material used as a resonator. More than one experiment is needed for the determination of all the components of the material tensors involved. Details of the procedure are outside of the scope of this thesis and can be found in appropriate literature [136, 137].

As a device converting electrical into mechanical energies, the piezoelectric transducer is also characterized by a coupling coefficient k, which is defined as a ratio of

mechanical to electrical energies, namely

$$k^2 = \frac{\mathcal{E}_m}{\mathcal{E}_e} = \frac{\frac{1}{2}\sigma_{jk}\epsilon_{jk}}{\frac{1}{2}D_i E_i} = \frac{c_{jkjk}\epsilon_{jk}^2}{\varepsilon_{ii}E_i^2} = \frac{c_{jkjk}d_{ijk}^2}{\varepsilon_{ii}} \tag{4.19}$$

which can also be expressed in terms of f_r and f_a in the following way

$$k^2 = \frac{\pi^2}{4}\left(\frac{f_a - f_r}{f_r}\right) \tag{4.20}$$

Equation 4.19 allows the determination of the temperature dependence of the component of the piezoelectric tensor involved in a particular mode of vibration.

The measurements of the resonance and antiresonance frequencies were also done using the HP 4192A Impedance Analyzer operating in an amplitude-gain mode. They were performed on the same samples as used for dielectric constant measurements. Initially the lowest resonance was found by scanning a range of frequencies. A computer controlled setup repeatedly scanned a frequency range around this resonance as the temperature was slowly lowered. The temperature data were continuously recorded in a file together with the resonator response as measured by the Impedance Analyzer. Therefore, in general a given scan contained data for the determination of f_r and f_a at slightly different temperatures. Simple linear interpolation was used to correctly determine both of the characteristic frequencies at a given temperature.

Pile Higher and Deeper
by Jorge Cham
www.phdcomics.com

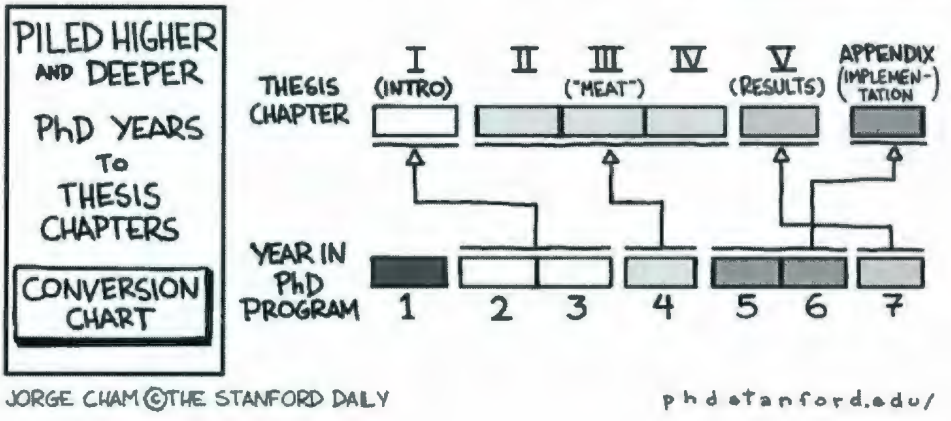

Chapter 5

Results and Discussion

5.1 Dielectric Properties

Dielectric constant measurement is the primary technique for studying phase transitions in ferroelectric crystals as well as in dipolar glasses. It can be performed over a wide range of frequencies using commercially available impedance analyzers (IA). In a typical experiment the sample is prepared in the form of a parallel plate capacitor of known area and thickness. It is then suitably mounted in a cryostat and connected to the input terminals of the IA. The meter then measures the complex impedance of the network and can be programmed to return the capacitance and the tangent of the phase angle between current and voltage on its digital output. Those values are then recorded by a computer and the real part of the dielectric constant is calculated from Equation 4.9. Since the tangent of the loss angle is the ratio of the imaginary to the real part of the dielectric constant the former can be also easily calculated from

$$\tan\delta = \frac{\mathrm{Im}[\varepsilon]}{\mathrm{Re}[\varepsilon]} \tag{5.1}$$

The analysis of the data is always based on the Debye model of dielectric relaxation which considers the response of a collection of noninteracting dipoles to the applied alternating electric field. Very important information about the nature and dynamics of the underlying process can be obtained by analyzing those data. The details of the analysis performed on the data obtained for this thesis will be described along with the results in the following sections.

5.1.1 KDP

Dielectric constant measurements of pure KDP were performed primarily for comparison purposes with KDP-ADP solid solutions. The sample used was in the shape of a disk 6.9 mm in diameter and 0.72 mm thick. Gold electrodes were evaporated on sample's largest surfaces which were perpendicular to c crystallographic axis. Measuring voltage was set to 0.1 V therefore the values of measuring electric field did not exceed 2.8 V/cm during the experiment. The rate of change of temperature was set to 0.2 K/min in the region of the phase transition. Cooling and heating runs were performed, however no appreciable thermal hysteresis was detected. Although measurements were performed at 40 different frequencies ranging from 40 Hz to 10 MHz equally spaced on a logarithmic scale, not all of the data are suitable for analysis due to high levels of noise at very low frequencies and very large signal distortions due to piezoelectric resonances at intermediate frequencies. The details will be discussed later in this section.

Typical results for the real part of the dielectric constant Re[ε] are shown in Figure 5.1. They illustrate all of the most important characteristic features of this type of measurement in KDP crystals. As can be seen, initially Re[ε] increases with decreasing temperature at all frequencies and reaches its maximum value of about

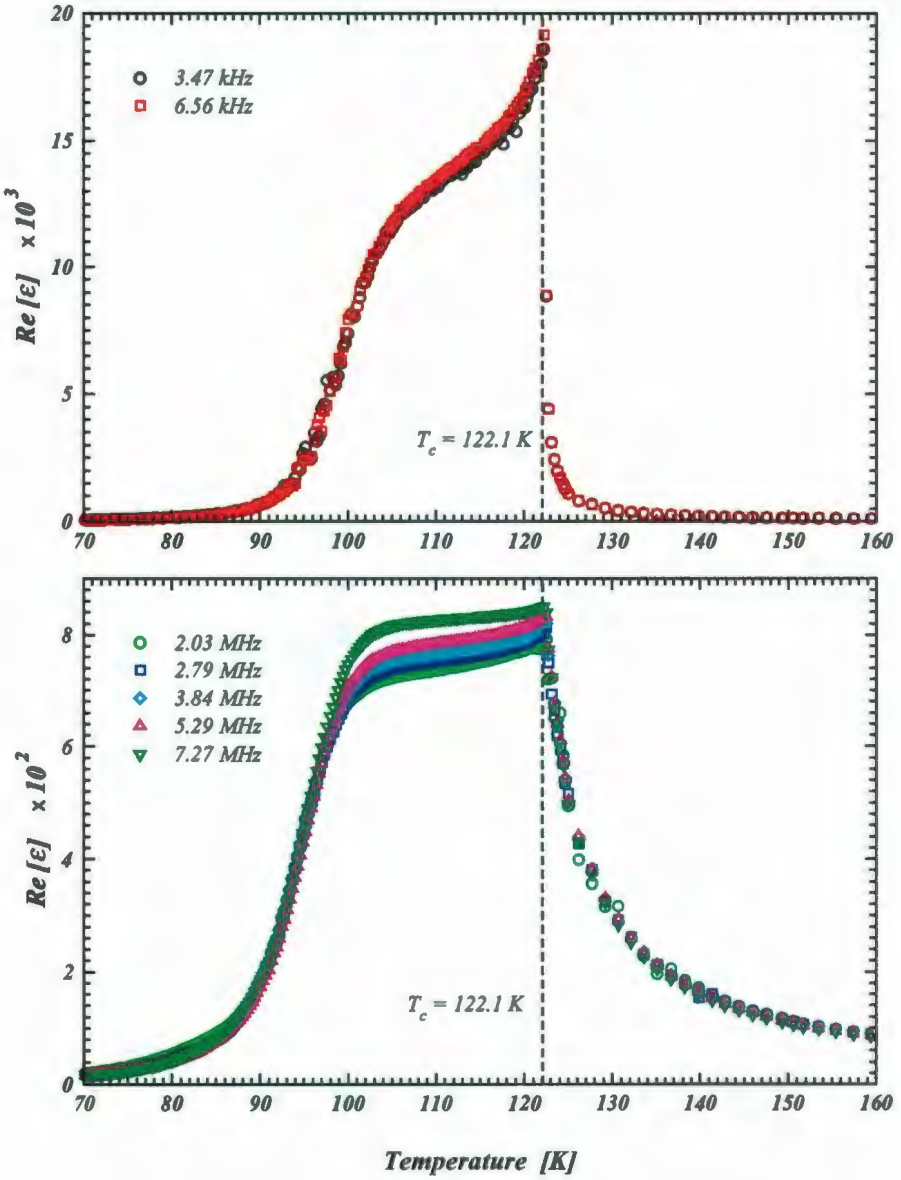

Figure 5.1: Temperature dependence of Re[ε] of KDP single crystal measured along its polar axis (selected frequencies).

20000 at $T_c = (122.1 \pm 0.3)$ K. This phase transition temperature agrees very well with literature data. Upon further cooling the value of Re[ε] remains high (of the order of 15000) down to about 105 K. This is the *plateau* region. Below that temperature it starts to decrease faster and reaches its room temperature value approximately at 90 K. Further temperature lowering results in gradual decrease of Re[ε] which approaches the value of 8 at 20 K.

It is generally accepted that the decrease of the Re[ε] around 95 K is related to the phenomena commonly referred to as *domain freezing*, i.e a cessation of the domain wall motion under the influence of the external electric field. The characteristic freezing temperature (denoted T_f) for that process can be deduced from the temperature dependence of the imaginary part of the dielectric constant shown in Figure 5.2. It corresponds to its maximum located approximately at 100 K. It agrees very well with the data reported by Bornarel [138] who studied the dependence of T_f on the magnitude of applied electric field.

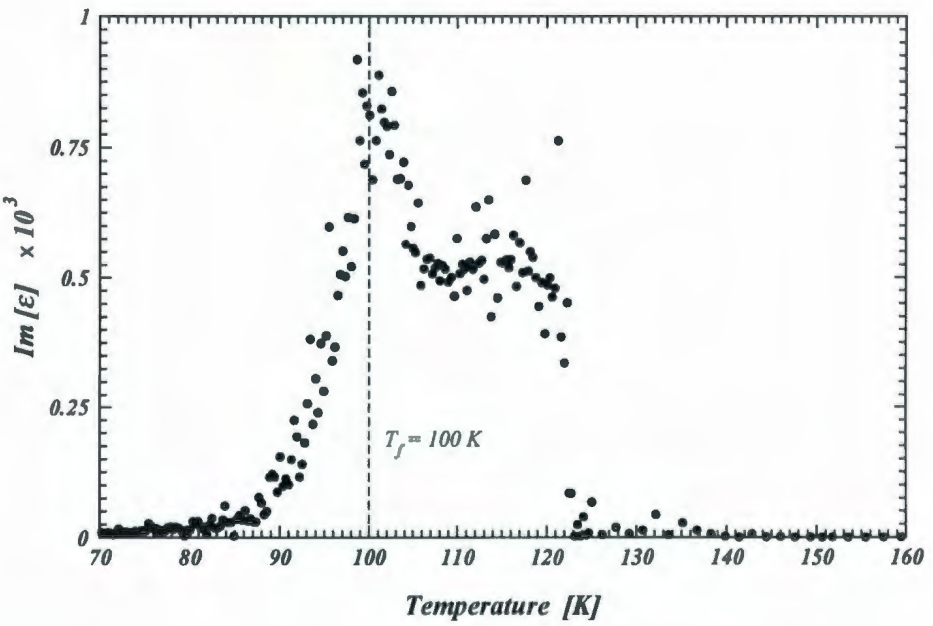

Figure 5.2: Temperature dependence of Im[ε] of KDP single crystal at 12.4 kHz.

Until recently crystals belonging to the KDP family were the only ones known to possess unusually high values of Re[ε] over a range of several tens of degrees below T_c. However, recent investigations of the temperature dependence of the dielectric constant in $(NH_2CH_2COOH)_3 \cdot H_2SO_4$ (triglycine sulfate) and CuAlZnNi single crystals [139] showed the existence of the domain freezing phenomena in those materials. This is expected result since all ferroelectric crystals, by definition, will possess a domain structure in their low temperature phase. If it is easy to move a domain wall inside a crystal by applying an electric field parallel to the direction of spontaneous polarization one can see that it will be reflected in the higher values of the dielectric constant below T_c. This is in fact observed in all ferroelectrics as a wing in the Re[ε] *vs.* T curve below T_c but never results in the *plateau* as in KDP type crystals. Moreover, the electric field threshold to move domain walls in KDP is of the order of 5-10 V/cm for longitudinal (movement of a tip of a needle like shaped domain parallel to its wall), and of the order of 100 V/cm for lateral motion (expansion of a width of the domain) [138] of domain walls. Those values were determined experimentally and later calculated theoretically [140] based on a model taking into account the pinning of domain walls by defects and a long range mutual interaction between domains. Given that the data presented in Figure 5.1 were collected with a measuring field smaller in magnitude then the threshold values, it is difficult to explain the existence of the plateau region.

Two other plausible explanations were developed in order to account for the existence of the plateau region in KDP type crystals. First, due to Fedosov [141], employs a two dimensional transverse Ising Hamiltonian, originally developed by Moore [142], to model a thin domain wall. According to his calculations the lattice energy barrier (an energy required to move the domain wall) is small in the plateau region and results in high domain wall mobilities. It vanishes at T_f at which temperature a structural

transformation between two configurations of pseudospins inside the wall takes place. Further temperature lowering results in an increase of the lattice energy barrier and is responsible for the domain freezing. Second, proposed by Kuramoto [143], attributes the domain freezing to the anomalous increase of the relaxation time around T_f (in his paper denoted by T_0). He studied the dielectric dispersion of KDP in a wide frequency range (from 110 Hz to 1 GHz) and observed two types of relaxations: resonant, related to the piezoelectric resonance, and a relaxational characterized by a wide distribution of relaxation times. In the plateau region the orientational contribution to the relaxation is enhanced by the piezoelectric vibration of the crystal plate. Below the freezing temperature they decouple resulting in a decrease of the Re[ε].

All of the three models outlined above correctly account for major experimental results observed in the plateau region in KDP. However, only the ones proposed by Bornarel and Kuramoto provide an explanation of another peculiar phenomena, namely the dependence of the value of Re[ε] in the plateau region on the sample thickness, d [144]. The phenomenon of image forces [145] in the former and the dependence of the resonant frequency on the sample size in the latter are the two mechanisms which could be responsible for this behavior. Although our data are qualitatively consistent with both models they do not support the validity of one over the other.

It should be mentioned that the data presented in this thesis show clearly the existence of the resonant dispersion in the plateau region as can be seen in Figure 5.3. It is interesting to note that its strength starts to increase about 0.5 K above T_c. This effect is a typical behavior for a continuous phase transition in which the fluctuations of the order parameter are responsible for that behavior. Therefore, our data indicate that the structural change in KDP, although of discontinuous character, displays some

characteristics of 2nd order phase transition as well.

As can also be seen from Figure 5.1 the decrease of the dielectric constant associated with the domain freezing occurs at the same temperature for all frequencies. This indicates that the relaxation time is independent of temperature, in contrary to the results presented by Kuramoto [143] and others [22, 146]. According to those authors the temperature dependence of the relaxation time associated with the domain freezing is governed by the Vogel-Fulcher law of the form

$$\tau = \tau_0 \exp\left(\frac{E}{T - T_f}\right) \tag{5.2}$$

where E is the activation energy and T_f is the freezing temperature. On the other hand, dielectric measurements in the frequency range from 2×10^{-3} to 10^3 Hz reported by Paul [20] revealed the existence of three different thermally activated relaxation phenomena with the relaxation time described accurately by the Arrhenius relation of the form

$$\tau = \tau_0 \exp\left(\frac{E}{T}\right) \tag{5.3}$$

where the parameters have the same meaning as above. Motegi [147] drawn the same conclusion from the analysis of the frequency dependence of the loss maxima. The source of those discrepancies, as well as the lack of any temperature dependence of the relaxation time in our results is not known at present. However, a very peculiar ferroelectric aging effect recently discovered by Mueller [148, 149], as well as the dependence of the parameters characterizing the low frequency dispersion in KDP on the type and the amount of impurities or defects present in the crystal [150] any conclusions regarding this phenomenon should be regarded with caution. Detailed investigations of the domain walls dynamics correlating their motion with the defect structure deserves further scientific attention.

Finally we present the temperature dependence of the inverse of the real part

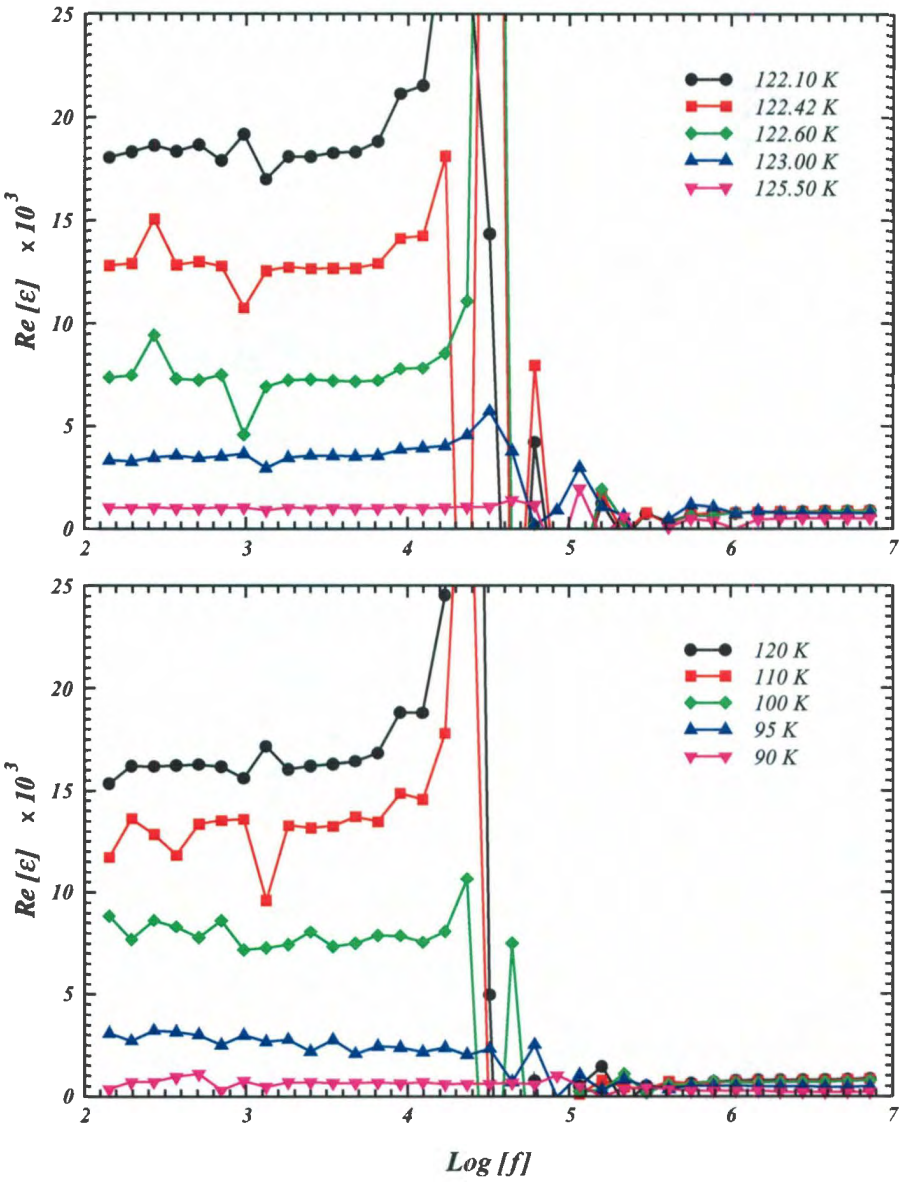

Figure 5.3: Frequency dependence of the real part of the dielectric constant of KDP single crystal at selected temperatures: a) just before T_c, b) below T_c.

of the dielectric constant in Figure 5.4. Two sets of curves can be identified in that figure. The ones collected at frequencies lower then the piezoelectric resonance frequency correspond to the constant stress condition and represent the free dielectric susceptibility κ^{σ}. In that regime, the sample changes its shape under the influence of the measuring electric field due to the piezoelectric effect resulting in the development of stress on its surface. On the other hand, at frequencies higher then the fundamental resonance, i.e. in the MHz range, the field variation is too fast for the sample to respond to it. Therefore the sample is inertially clamped. Those curves represent the value of κ^{ϵ}. As can be seen in Figure 5.4 both sets of curves are very well approximated by the Curie-Weiss law of the form

$$\kappa = \frac{(T - T_c)}{C_{C-W}} + A \tag{5.4}$$

where C_{C-W} and T_c are the Curie-Weiss constant and the Curie temperature respectively. The phase transition temperature, T_c=122.1 K was adjusted manually to obtain the best correlation coefficient for the fit. Experimental data deviate from the best fit line at temperatures above approximately 160 K. The Curie-Weiss constants determined from that analysis are: $C^{\sigma}_{C-W} = (3520 \pm 25)$ K for the free and $C^{\epsilon}_{C-W} = (3620 \pm 20)$ for the clamped dielectric susceptibilities respectively. The points where the fitted lines cross the horizontal axis designates the Curie-Weiss temperature T_0 below which the ferroelectric phase is the only stable one (see section 2.3.2). They are: $\tilde{T}_0 = (122 \pm 0.3)$ K and $T_0 = (118 \pm 0.5)$ K for free and clamped samples respectively. They differ by 4 K which is in agreement with previously published results [151].

The results of the temperature dependence of the ε_{33} dielectric constant for KDP crystal presented above show most of the general features of the ferroelectric phase transition in this crystal. The phenomenological parameters determined are in good

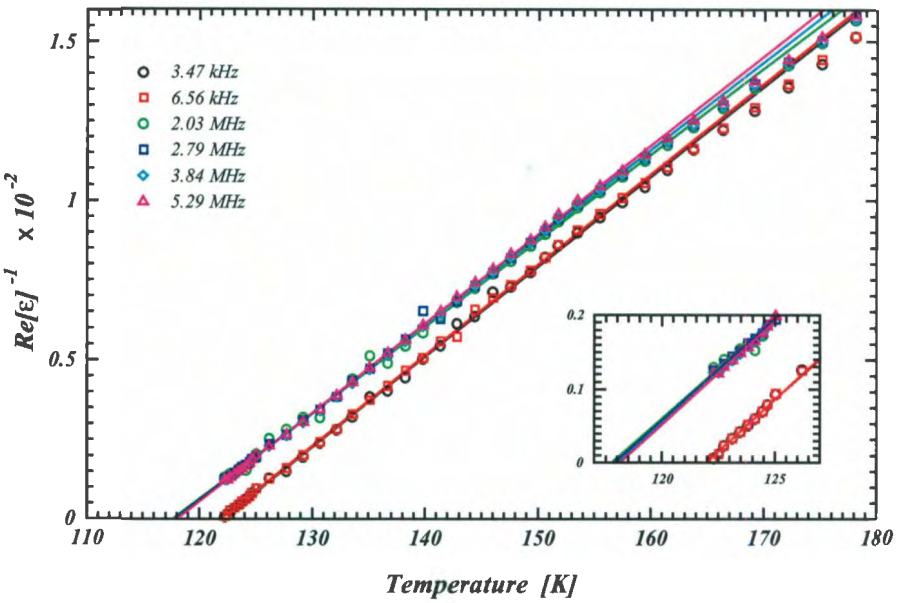

Figure 5.4: Inverse dielectric constant as a function of temperature for KDP in the paraelectric phase. The solid lines represent Curie-Weiss law fits to the data sets with the same color of the symbols.

agreement with the literature data. Considering the complexity of the polarization relaxation processes present in this material, and their sensitivity to the presence of defects and impurities it will be interesting to see how the substitution of NH_4 ions into the crystal lattice influences its dielectric properties.

5.1.2 KADP1

Samples of the KADP:2.1 single crystal for the measurements of the temperature dependence of the dielectric constant were also prepared in a shape of a disk of 8.0 mm in diameter and 1.12 mm thick. Its largest surface was gold plated in vacuum. The measurements were performed in *Crystal Physics Division* of the Institute of Physics in Poznań, Poland. The measurements were performed at 17 different frequencies ranging from 100 Hz up to 1 MHz. This somewhat limited range was dictated by the

fact that different Impedance Analyzer was used in this case. Similarly as in the case of the KDP, data collected in the vicinity of the piezoelectric resonance frequencies had to be excluded from the analysis.

The plot of Re[ε] *vs.* T, for selected frequencies for KADP:2.1 single crystal is presented in Figure 5.5. The dielectric constant increases with decreasing temperature and reaches its highest value at the phase transition temperature $T_c = (112.5 \pm 0.3)$ K. This value is lower than for pure KDP by 10 K. This is in agreement with the fact that in general T_c decreases with increasing concentration of NH_4 ions [81, 87, 152, 153]. Korotkov [153] proposed a Vegard[1] type rule describing the composition dependence of the Curie temperature of the following form

$$T_c(x) \approx T_c - x[T_c - (-T_N)] \tag{5.5}$$

where T_c and T_N are the phase transition temperatures of the parent compounds. The above relation gives $T_c = 116.6$ K for x=0.02.

With further temperature lowering the dielectric constant decreases in value and displays the plateau region where it stays at a relatively high level. It is qualitatively similar to the temperature behavior of the Re[ε] for pure KDP presented in previous section. Although there is no direct evidence for the existence of ferroelastic domains in KDP-ADP solid solutions, the assumption of their existence is certainly very plausible. Therefore the anomalously high values of the real part of the dielectric constant below T_c can be attributed to the same mechanisms as in KDP.

Upon further cooling the value of Re[ε] starts to decrease more rapidly at around 90 K and attains the room temperature value at about 80 K. This decrease is ac-

[1]Vegard's rule, originally proposed in 1921 [154] allows one to write down the relation between the volume of the solid solution V and the volumes of the end members V^A and V^B as: $V(A_{1-x}B_x) = V^A(1-x) + V^B x$. Its applicability to the phase transition temperatures can not be justified based on the fact that T_c for solid solution does not follow a straight line connecting the phase transition temperatures of the end members.

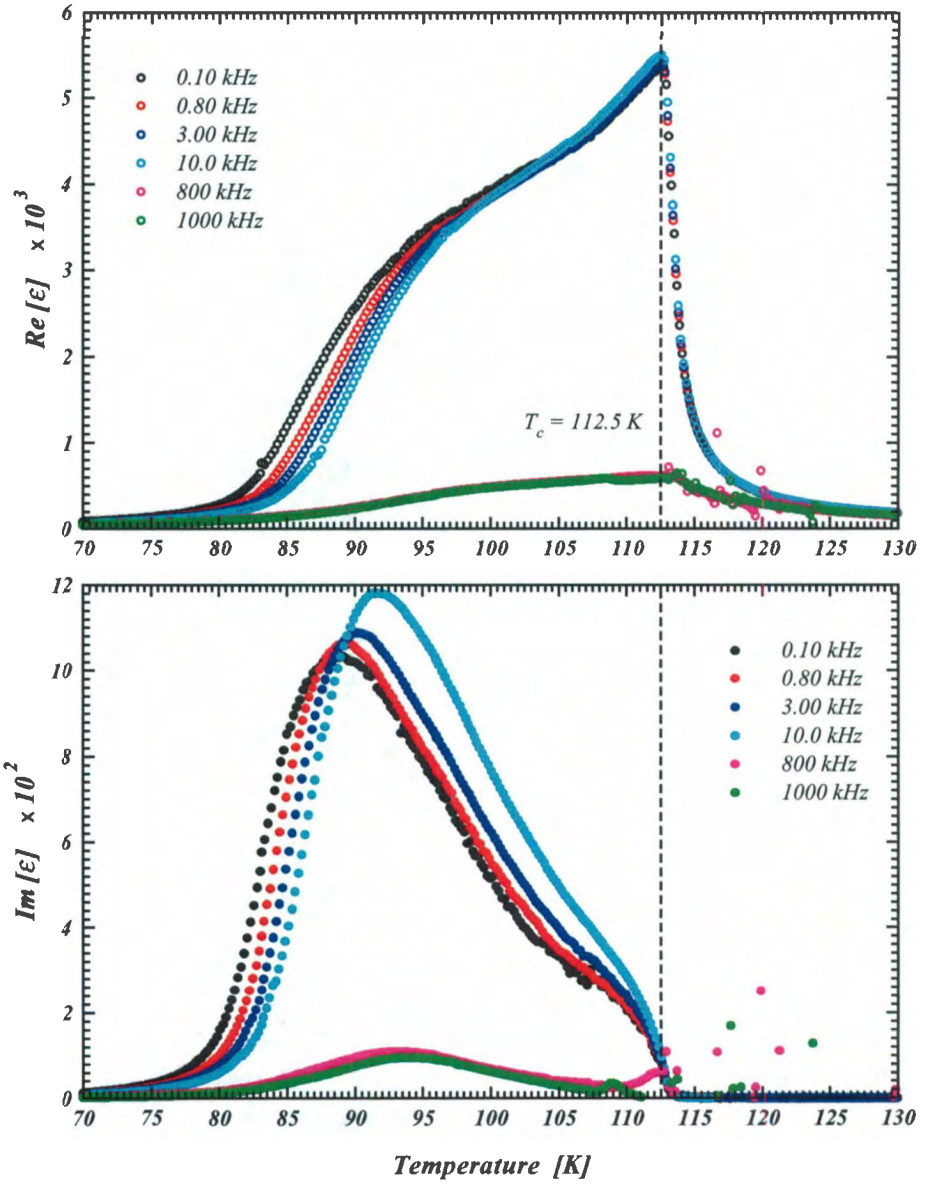

Figure 5.5: Temperature dependence of the real (top) and imaginary (bottom) parts of the dielectric constant of the KADP:2.1 single crystal at selected frequencies.

companied by a peak in the temperature dependence of the imaginary part of the dielectric constant.

Clearly the general features of the temperature dependence of the dielectric constant for KADP:2.1 sample are very similar to those already discussed for pure KDP. However, by comparing Figure 5.1 and 5.5 several differences can be identified. For example, although the room temperature value of the dielectric constant was higher than in the case of KDP (of the order of 55), the peak value at T_c was only of the order of 5400, i.e about 30% of the maximum value recorded for KDP. Moreover, the peak of Re[ε] *vs.* T curve just above T_c is rounded as can be clearly seen in the inset in Figure 5.6 where the dielectric susceptibility is plotted as a function of temperature. The phase transition becomes more diffuse. This type of behavior has already been

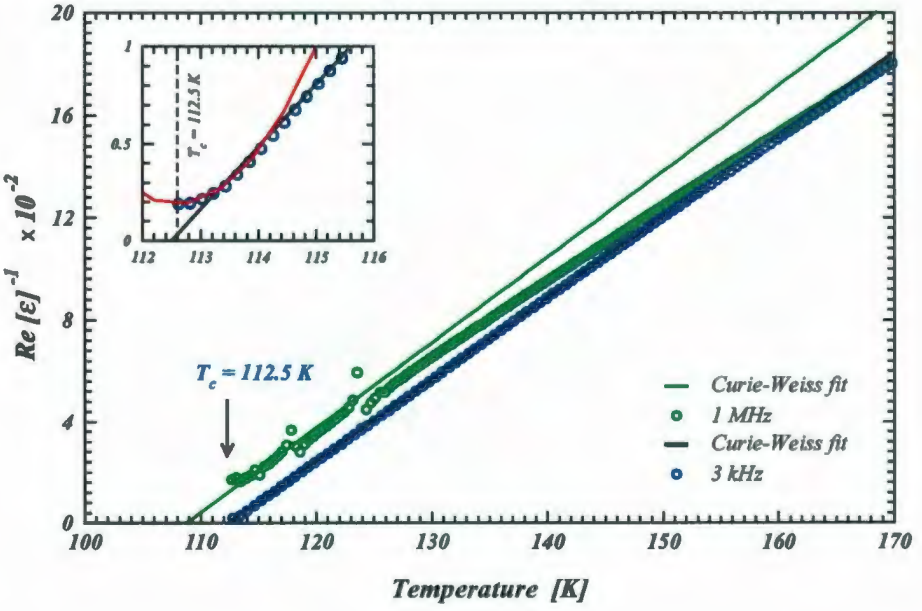

Figure 5.6: Temperature dependence of the inverse of the real part of the dielectric constant above T_c for the KADP:2.1 crystal. The inset shows the temperature region close to T_c and a quadratic fit to the data based on equation 5.7.

observed in KADP crystals by Korotkov [153]. This smearing of the phase transi-

tion resembles the behavior of a group of materials called relaxor ferroelectrics [155] of which mixed-cation ferroelectrics of the perovskite structure with general formula $A_{1-x}A'_xB_{1-y}B'_yO_3$ are the primary and most studied examples [2]. The diffuse phase transition is their central characteristic and is attributed to the presence of structural inhomogeneities resulting in the development of a polar micro regions characterized by their own, size dependent, transition temperature [156]. Their existence was determined experimentally in PST (see footnote) relaxor ferroelectric [157–159] and others [160, 161]. Assuming after Kirillov [162] that the distribution of the transition temperatures for regions of various sizes can be approximated by a Gaussian function of the form

$$\varphi = \frac{1}{\delta\sqrt{2\pi}} \exp\left[\frac{-(T-\widehat{T}_0)^2}{2\delta^2}\right] \tag{5.6}$$

where $\widehat{T}_0$ and δ are the average Curie-Weiss temperature and the width of the distribution describing the diffuseness of the transition, the temperature dependence of the dielectric susceptibility can be written as [162, 163]

$$\frac{1}{\varepsilon' - \varepsilon_\infty} = \frac{1}{\varepsilon'_m} + \frac{(T-\widehat{T}_0)^2}{2\varepsilon'_m\delta^2} \tag{5.7}$$

where ε'_m is the peak value of the real part of the dielectric constant. The above relation was successfully used to analyze compounds of the KADP system [164]. Moreover, an empirical formula for the composition dependence of the diffuseness parameter δ was established [165]. It has the following form

$$\delta \cong \delta_0 \exp\left[qx(1-x)\right] \tag{5.8}$$

with $\delta_0 \cong 0.27$ K and $q \cong 23$. An attempt was made to determine the value of the parameter δ from data presented in Figure 5.6. However, as can be clearly seen on that

[2]Specific examples include: $PbMg_{1/3}Nb_{2/3}O_3$ (PMN), $PbSc_{1/2}Ta_{1/2}O_3$ (PST), $Pb_{1/2}Sc_{1/2}Nb_{1/2}O_3$ (PSN), $Pb_{1-x}La_xZr_{1-y}Ti_yO_3$ (PLZT)

graph, it is best approximated by a typical linear Curie-Weiss law with C_{C-W} constant equal to (3100±22) K and $\tilde{T}_0 = (112.0 \pm 0.6)$ K. The value of that constant for clamped dielectric susceptibility is (2980 ± 25) K and was determined by a straight line fit to the data collected at the highest measuring frequency. The fit was performed based on the data points lying in the very narrow temperature interval close to T_c because even at that frequency there are piezoelectric resonances present which influence the overall temperature dependence of κ^{ϵ}. The result of the fit is shown in Figure 5.6 as a green line. The value of Curie-Weiss temperature obtained from that analysis is $T_0 = (108.8 \pm 0.6)$ K. It is interesting to note that the difference $T_c - T_0 \cong 4$ K and is similar to that obtained for KDP. Also the difference between Curie-Weiss constant for the mechanically clamped and mechanically free conditions is approximately 100 K, i.e. of the same order of magnitude as in the case of KDP.

Although the analysis of the dielectric susceptibility data did not yield any support for the existence of the polar micro regions in our samples the analysis of the frequency dependence of Re[ε], shown in Figure 5.7, clearly shows the existence of the resonant dispersion in a temperature interval from 112.0 K up to the phase transition temperature for pure KDP, i.e. 122.0 K. This result is consistent with the fact that, similarly as in the case of relaxor ferroelectrics, there exist a wide temperature interval above the peak of the dielectric constant in which fluctuating spontaneous polarization appears. On the average $P_s = 0$, therefore its values can be extracted from measurements of optical birefringence, or thermal expansion data because those quantities depend on the square of the polarization through electrostriction. Such measurements were conducted for numerous relaxor ferroelectrics, revealing the existence of a high temperature tail of P_s above T_c. The existence of the remnant polarization was also discovered in KDP-ADP solid solutions [165].

The most interesting difference between the pure KDP and mixed KADP:2.1 sam-

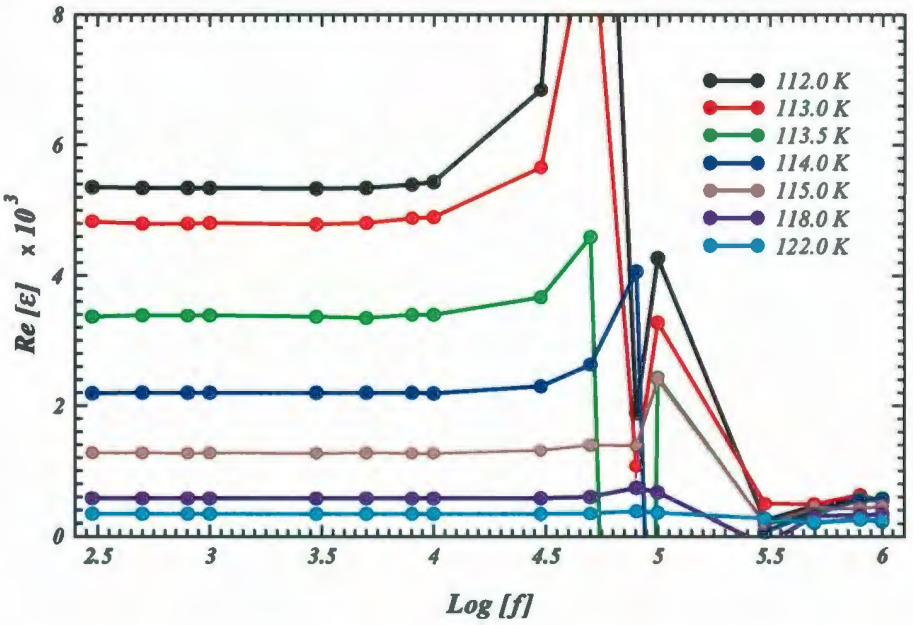

Figure 5.7: Frequency dependence of the the real part of the dielectric constant above T_c for the KADP:2.1 crystal.

ples, revealed by dielectric constant measurements, is the appearance of a temperature dependent dispersion in the vicinity of the domain freezing temperature. As can be seen in Figure 5.5 the higher the frequency the sooner the domain walls stop responding to the AC measuring field. This behavior is also visible in the Im[ε] *vs.* T curves, where the maxima appear at higher temperatures for higher measuring frequency. To further investigate the relaxation processes present in the KADP:2.1 crystal below T_c a plot of Re[ε] *vs.* logarithm of the measuring frequency, shown in Figure 5.8, was prepared. Two dispersive processes can be easily identified. First, (marked as P_1) one of the resonant type, with resonance frequency of the order of 10^5 Hz, is the result of the piezoelectric effect present in the sample. Its position weakly depends on temperature. It should be noted that there is more then one resonance present on all the curves shown in Figure 5.8. They are located very close to each other, and are

a result of vibrations of different parts of the sample due to its uneven width. Due to the limited number of frequencies available in the Impedance Analyzer used for those measurements it was impossible to resolve them. The second dispersive process (marked as P_2) is relaxational in nature and can be identified from a variations of the dielectric constant as a function of frequency at frequencies below the piezoelectric resonances. It is very wide, which is characteristic of a wide distribution of relaxation times. It is also characterized by a very strong dependence on temperature. This is clearly visible as a broad feature moving towards lower frequencies (longer relaxation times) region as the temperature is lowered on the graph of the Im[ε] *vs.* Log[f].

It is interesting to note that very similar dielectric spectra were observed by Kuramoto in pure KDP [143, 166] while investigating the nature of the domain freezing phenomenon. He was able to determine the temperature dependencies of the mean relaxation time τ_0 and the width of the relaxation time distribution function (approximated by a Gaussian peak) by modeling his dielectric spectra with the following formula

$$\varepsilon(\omega) = [\varepsilon_1 - \varepsilon_2]\, A + [\varepsilon_2 - \varepsilon_\infty]\, B + \varepsilon_\infty \tag{5.9}$$

with

$$A = \frac{\omega_0^2}{\omega_0^2 - \omega^2 + i\gamma\omega} \tag{5.10}$$

and

$$B = \int_0^\infty \frac{g(\tau)}{1 + i\omega\tau} d\ln(\tau) \tag{5.11}$$

where A describes the resonant dispersion centered at ω_0 with damping coefficient γ, and B is the relaxational dispersion characterized by a broad distribution of the relaxation times $g(\tau)$. However, his measurements span seven decades on the frequency scale. Unfortunately, an attempt at conducting similar analysis on the data presented here failed due to the limited frequency range and a lack of sufficient resolution (on

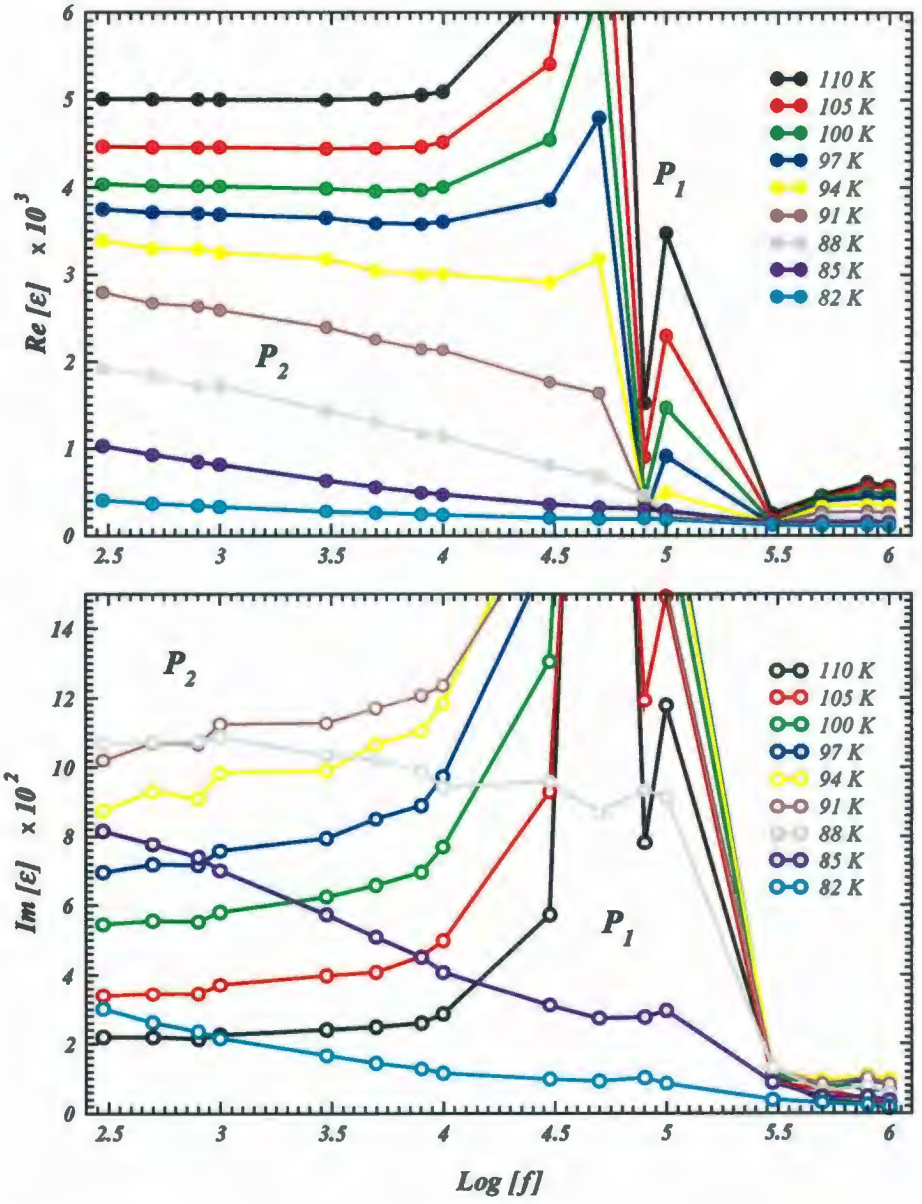

Figure 5.8: Frequency dependence of the the real (top) and the imaginary (bottom) part of the dielectric constant below T_c for the KADP:2.1 crystal.

the frequency scale) to account for the details of the resonances.

However, the schematic representation of the anomalous dispersions present in our data is shown in Figure 5.9. The top row shows plots of the real part of the dielectric constant *vs.* frequency in three different temperature regions. The labels P_1 and P_2 indicate the dispersion regions as discussed above. The parameters describing those processes were chosen somewhat arbitrarily. The relaxational one was modeled using Equation 2.32 with $h < 1$ to account for the distribution of the relaxation times. τ_0 is the mean relaxation time. The resonant dispersion was modeled with Equation 5.10. The resonant frequency, and the damping constant are the same for all graphs except for the third column where the resonant dispersion was heavily damped. The bottom row of plots in Figure 5.9 shows corresponding Cole-Cole diagrams. Clearly all the general features of our dielectric spectra shown on Figure 5.8 are qualitatively represented there which provides supporting evidence for our claims regarding the relaxation phenomena present in our sample. The existence of the dipolar glass phase in our samples is the most likely origin of such behavior.

To further corroborate our findings regarding the dielectric spectra the Cole-Cole diagrams were prepared for selected temperatures below T_c. They are shown on Figure 5.10. They were prepared by interpolating the temperature data with a linear function and plotting the $Im[\varepsilon]$ *vs.* $Re[\varepsilon]$ for a given temperature. They include data recorded at all frequencies including those not shown in Figure 5.5. The graphs confirm the existence of two dispersions in our data. The top graph in Figure 5.10 shows data in the temperature range of 30 K below T_c. Each of the curves shown consists of a part of a semi-circular pattern on the low frequency side. This is due to the relaxational dispersion discussed above. From the angle those arcs make with the Re[ε], at T close to T_c, it can be inferred that the process is characterized by a very narrow distribution of relaxation times (see the dashed green line on Figure 5.10).

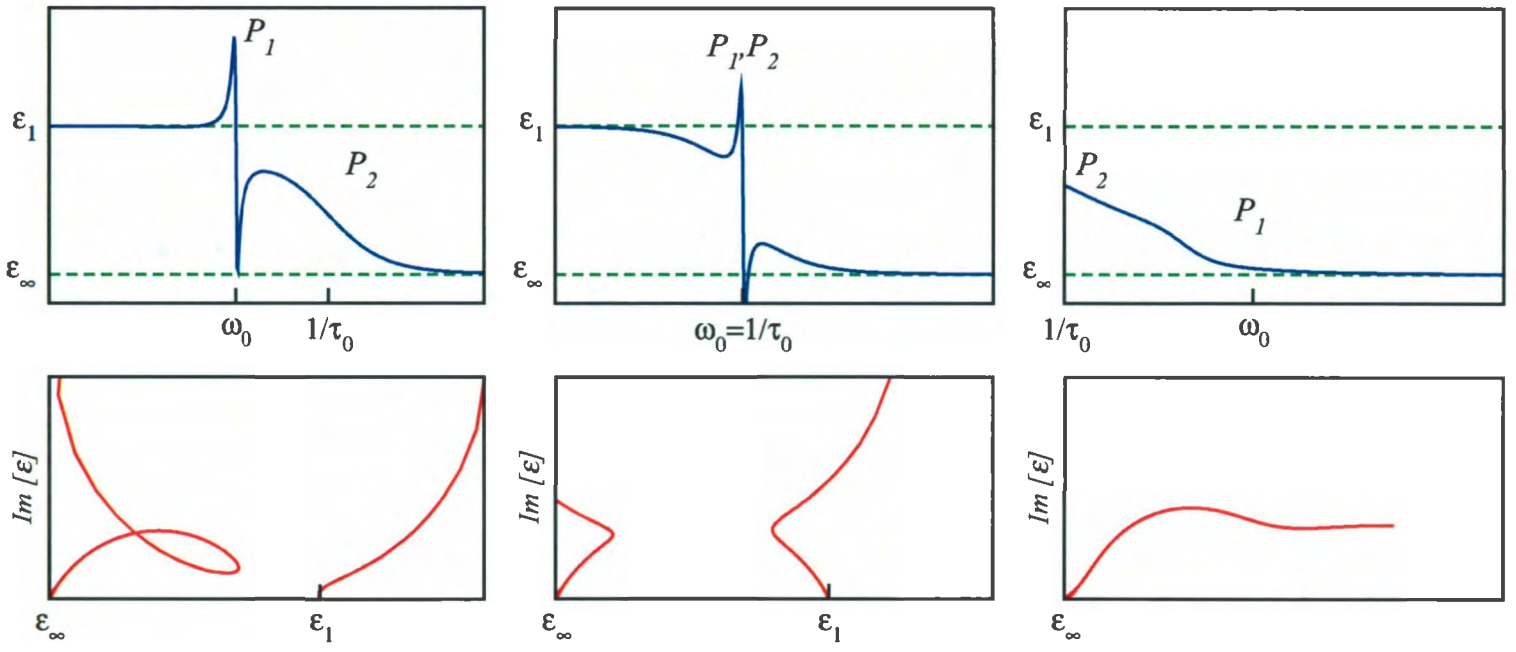

Figure 5.9: Schematic representation of the frequency dependence of the real part of the dielectric constant (top row) and the corresponding Cole-Cole diagrams (bottom row) in the case of two dispersions: resonant (P_1), and relaxational (P_2) (see text for details).

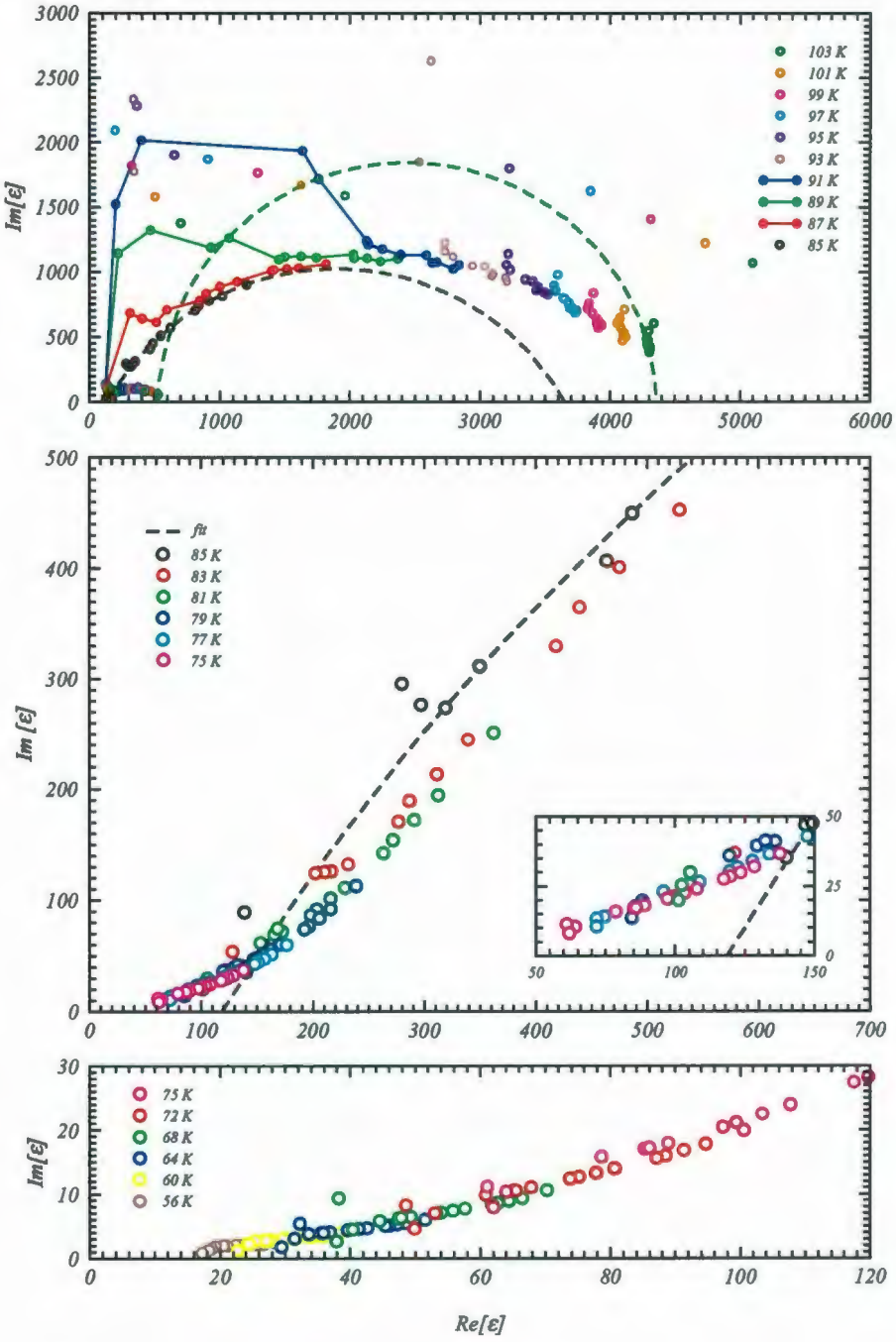

Figure 5.10: Cole-Cole diagram for the KADP:2.1 crystal at selected temperatures below the transition temperature.

Therefore it is almost Debye-like in character. As the temperature is lowered the center of the semi-circular arcs moves further below the abscissa (see the black dashed line on Figure 5.10), thereby indicating gradual broadening of the distribution function. The very narrow range of frequencies used in the experiment did not allow for a successful fitting of the circular arcs to the data at all temperatures. It was possible only in the range from 80 K to 85 K. The dashed line on the figure which crosses the data at 85 K is an example of such a fit, however the line at 103 K is drawn only as a guide. The temperature change of the mean relaxation time is reflected by the fact that for different temperatures the low frequency portion of the data lays on a different segment of the arc.

The resonant dispersion is also clearly visible on the top graph in Figure 5.10. It is represented by those portions of the data which deviate strongly from the semi-circular arcs at the low frequency ends. In principle they trace a circle the radius of which indicates the value of the damping constant γ, the smaller the radius the larger the value of γ. Therefore it can be inferred from our data that the damping constant increases as the temperature decreases. It should be noted that all of the data sets meet in the lower left hand corner of the graph. This is the high frequency end of the resonances, completing the circle which is largely located outside of the scale of the graph. The apparent gap in the data along the semicircular arcs representing the relaxational dispersion, projected on the Re[ε] axis designates the strength of the resonant dispersion, i.e the value of $[\varepsilon_1 - \varepsilon_2]$ in Equation 5.9. It is clear that it decreases with decreasing temperature.

The general features of the dispersion processes present in KADP:2.1 crystal seem to be confirmed by the dielectric data shown on the two bottom plots in Figure 5.10. For example, at the lowest temperatures the semicircular arcs are extremely flat, indicating a very broad distribution of relaxation times. The resonances are prac-

tically nonexistent due to their small strength and large attenuation. However, in order to conduct more quantitative analysis, it appears to be necessary to extend the measurements towards ultra low and very high frequency regions.

5.1.3 KADP2

A sample of the KADP:12 single crystal for the dielectric measurements was prepared in the shape of rectangular slab with dimensions $9.5 \times 2.1 \times 0.62$ mm^3. Gold electrodes were evaporated on its larger surface which was normal to [001] crystallographic direction. The edges were parallel to [100] and [010] directions. The measurements were performed in the temperature range from 15 K to 290 K at 30 different frequencies ranging from 100 Hz up to 10 MHz. The measuring field used was of the order of 1.6 V/cm and the rate of temperature change in the region of the anomalous temperature dependence of Re[ε] was set to 0.2 K/min. Typical data at selected frequencies are shown in Figure 5.11. Clearly, the data display the same qualitative features as for the two samples already discussed in previous sections.

Upon cooling the sample the dielectric constant value gradually increases, from its room temperature value of 12 to its maximum at $T_m = (71 \pm 2)$ K. This temperature will be referred to as T_m since it is not clear if it is the equivalent of the Curie temperature typically observed in the dielectric spectra of crystalline materials described by Landau theory. Its value of 470 is smaller than in all previous crystals studied. Therefore it can be concluded that the introduction of NH_4 ions into the lattice structure greatly influences its polarization reversal properties. The temperatures at which the maximum value of Re[ε] is observed is different for free and clamped conditions as indicated on the insert in Figure 5.12. The values are: $T_{m1} = (70 \pm 0.5)$ K and $T_{m2} = (73.5 \pm 0.5)$ K for constant stress and constant strain conditions, respectively.

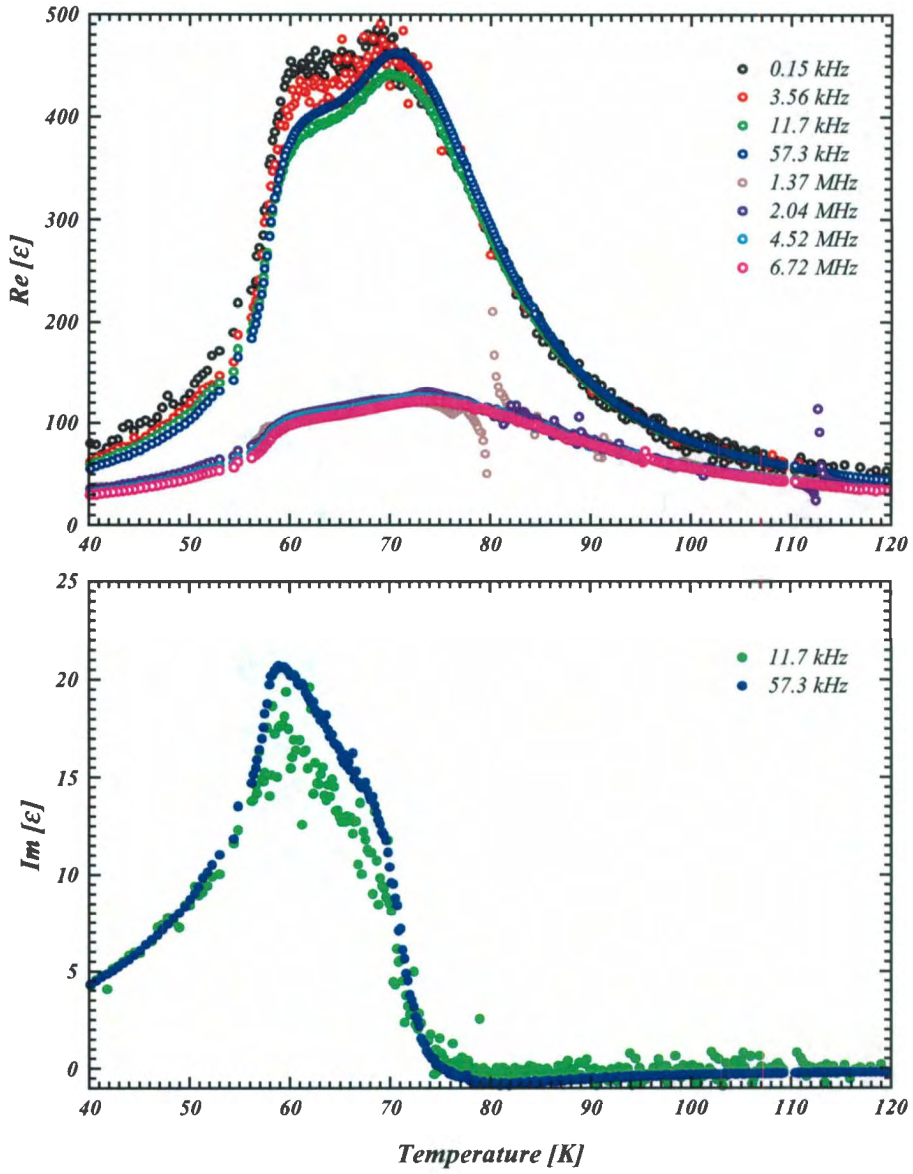

Figure 5.11: Real and Imaginary parts of the relative dielectric constant as a function of temperature for selected frequencies for the KADP:12 crystal.

The roundness of the maximum indicates a diffuseness of the phase transition.

Below T_m the plateau region can be clearly observed. However, it should be noted that it spans only a region of approximately 10 K which is smaller then in pure KDP and KADP:2.1 in which this region was extending for approximately 20 K below the phase transition temperature. Moreover, the decrease of Re[ε] on the low temperature side of the plateau region is more abrupt then in the case of the KDP and KADP:2.1 samples. It takes place just below 60 K, the freezing temperature, and over a 4 K range decreases by more then 50 %. Further temperature lowering results in its more gradual decrease resulting in the value of approximately 22 at 15 K. This behavior is present at frequencies lower then the piezoelectric resonance frequency. The imaginary part of the dielectric constant shows a maximum at $T_f = 60$ K. Another important difference is also clearly identified in Figure 5.11, namely the fact that the value of T_f does not depend on the frequency of the measuring field. Therefore the situation is similar to that discovered in pure KDP. This, rather unexpected result only confirms the complicated nature of the domain freezing process. No explanation of that fact can be offered without conducting more thorough investigations, specifically, measurements on crystals with different compositions in the range $0 < x < 30$.

As can also be seen in Figure 5.11 the curves recorded at frequencies lower then 10 kHz are characterized by a considerable amount of noise. The same is true for the Im[ε] *vs.* T data (not shown in Figure 5.11 for clarity). Although equipment problems cannot be excluded as a source of this noise it is rather unusual that it is not present at higher frequencies. Moreover, the curve recorded at 7.88 kHz (not shown in Figure 5.11) displays characteristics which are typically observed in the frequency region influenced by the piezoelectric resonances. Because the structure and the dynamics of the polarization reversal of the KDP-ADP solid solution becomes progressively more complex with increasing concentrations of ammonium ions the possibility of the exis-

tence of regions with different elastic properties resulting in much lower piezoelectric resonances should not be excluded. However, this hypothesis should be a subject of more detailed experimental studies and remains purely speculative at present.

In order to investigate further the dielectric properties of the KADP:12 crystal in the temperature range above the transition temperature the plots of the temperature dependence of the inverse of the dielectric constant were prepared. They are shown in Figure 5.12. The two frequencies plotted are representative of the low (constant stress region) and high (constant strain region) frequency ranges. The presence of the piezoelectric resonances even at 6.72 MHz is obvious. For the purposes of comparison with

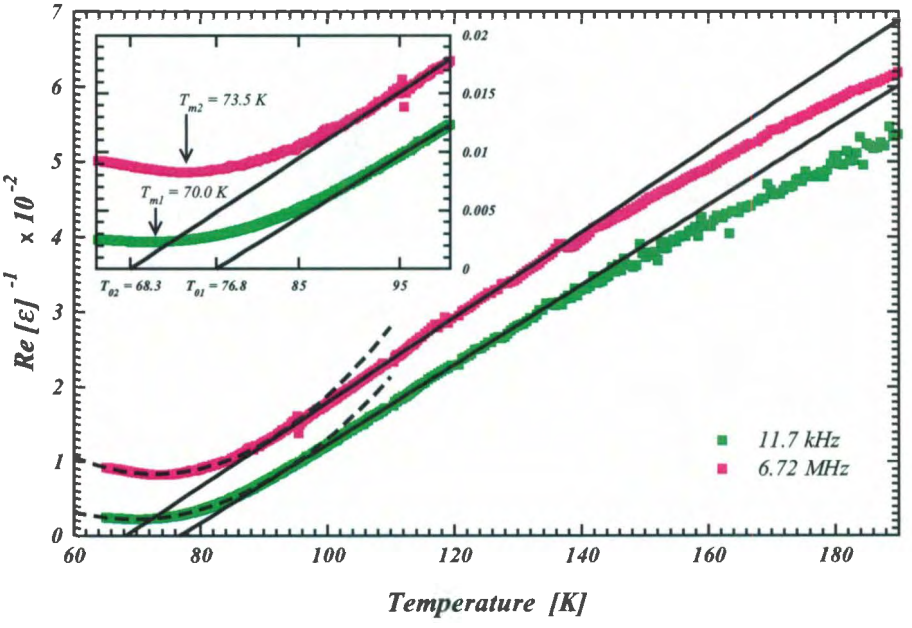

Figure 5.12: The inverse of the dielectric constant as a function of temperature for the KADP:12 crystal.

the KADP:2.1 results reported in the previous section a Curie-Weiss law was fitted to the data in the 90 K to 120 K range. The fits are represented as black solid lines in Figure 5.12. The Curie-Weiss constants obtained are: (1880±30) K and (1765±30) K

for the free and clamped cases, respectively. Those values are considerably lower than for the pure KDP and KADP:2.1 samples. As can be seen from Figure 5.12 the data points deviate considerably from the theoretical lines around 140 K. Moreover, the Curie Weiss law is also not obeyed in the immediate vicinity of T_m. This is due to the diffuse character of the phase transition. The diffuse region is considerably wider then in the case of KADP:2.1 sample and covers a range of approximately 15 degrees above T_m. Equation 5.7 was fitted to the data in this temperature interval. The results of this analysis are shown as dashed lines in Figure 5.12. The diffuseness parameters are: $\delta_1 = 9.88$ and $\delta_2 = 17.05$ for free and clamped conditions, respectively. They do not agree with similar values calculated from Equation 5.8 which gives $\delta = 3.06$.

Although the temperature dependence of Re[ε] indicates that the domain freezing temperature is independent of the frequency of the measuring field it is instructive to look at the frequency dependence of this parameter. These data, in the temperature range above T_m are shown in Figure 5.13. The resonant dispersion is clearly identifiable. It is located at frequencies of the order of 10^5 Hz and is related to the piezoelectric activity of the sample. Moreover, its strength gradually increases starting at 120 K and reaches its maximum at the temperature where the peak of Re[ε] *vs.* T is located. This behavior is in agreement with our hypothesis of the existence of the polar microregions in KADP:12 in that temperature interval. This dispersion is observable also at all temperatures below T_m, although its strength gradually decreases in that temperature range as can be seen in Figure 5.14.

In addition, there is yet another anomaly visible on the Re[ε] *vs.* Log[f] curves. It is located at lower frequencies (approximately 10^4 Hz) and becomes visible only for temperatures lower then about 80 K. It is smaller than the previously discussed one, and appears to disappear below 55 K. Its origin is currently not known. It may indicate an existence of another phase in the sample with very different elastic

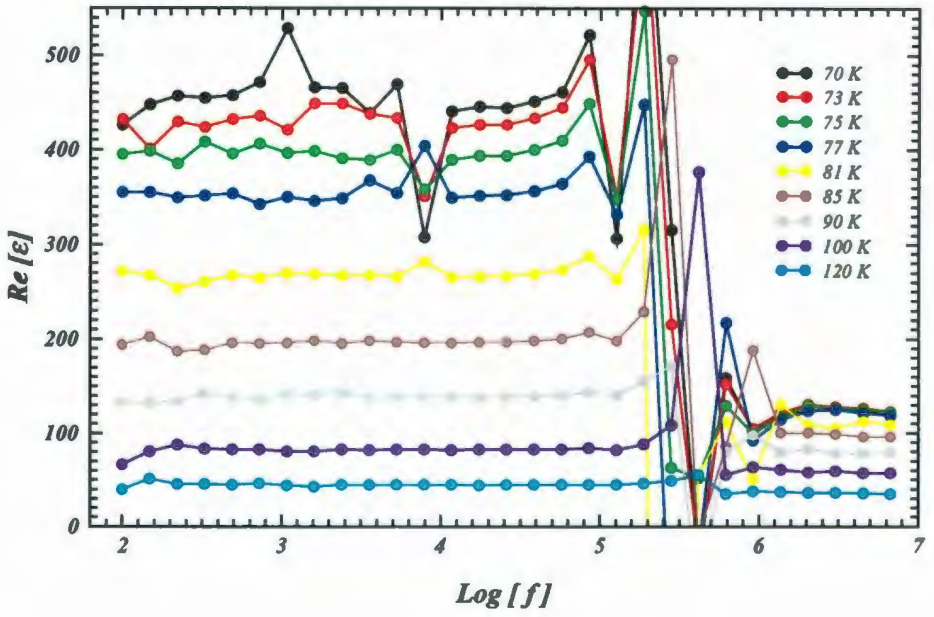

Figure 5.13: The dielectric constant as a function of the logarithm of the frequency for the KADP:12 crystal at temperatures above T_m.

properties resulting in lower resonant frequencies. Although the coexistence of glass and ferroelectric phases in KDP-ADP solid solution has been reported in the scientific literature no reports on the elastic properties of the glass phase are available at present.

It is interesting to note that the relaxational dispersion already discussed during the analysis of the dielectric data for the KADP:2.1 sample is also present in the KADP:12 crystal. It is observed as a gradually increasing values of Re[ε] with lowering measuring frequency in the region below the main resonances as shown in Figure 5.14. Its rather gentle slope is indicative of an even broader distribution of relaxation times then in a case of the KADP:2.1 crystal.

Unfortunately the noisy low frequency data for Im[ε], and limited range of frequencies used in our experiments, did not permit the extraction of any more details of the dispersion processes present in the data. It was also difficult to construct

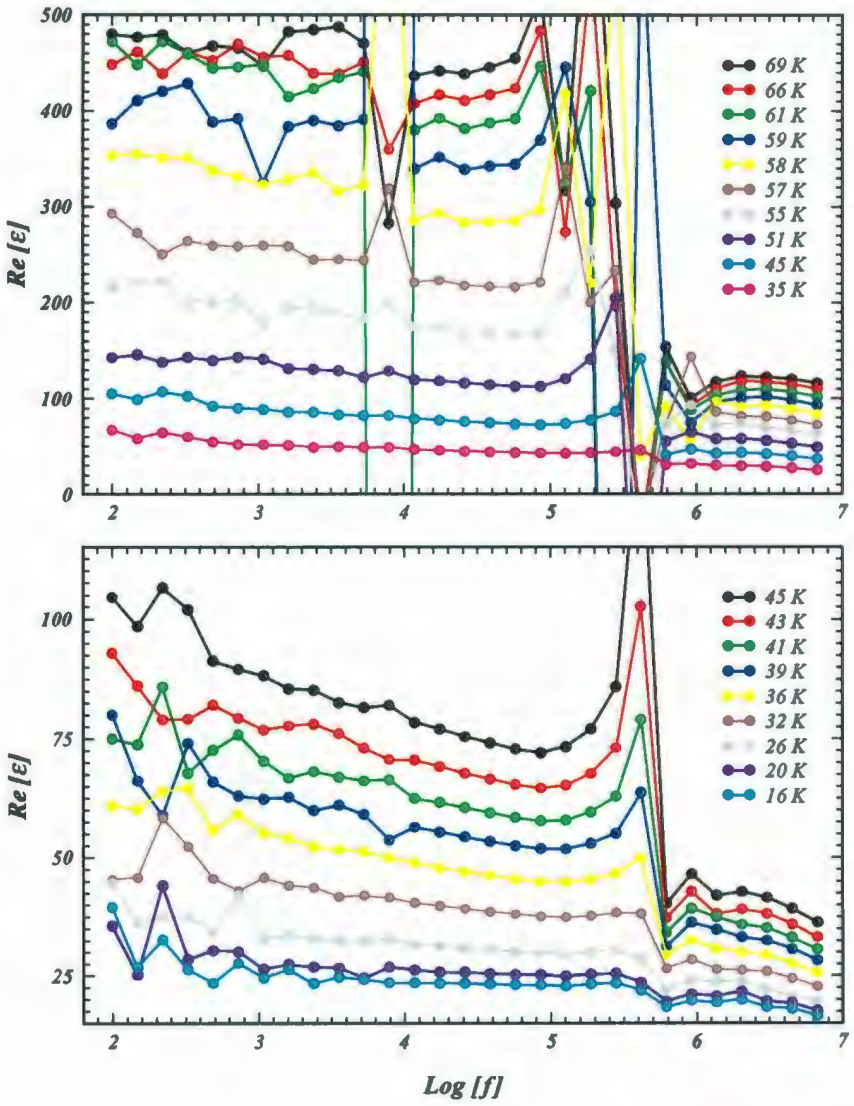

Figure 5.14: The dielectric constant as a function of the logarithm of the frequency for the KADP:12 crystal at temperatures below T_m.

meaningful Cole -Cole diagrams to confirm further if the width of the distribution of relaxation times is temperature dependent or not.

5.2 Elastic Properties

It is rather surprising that there are no reports regarding the temperature dependence of the elastic properties of KDP-ADP solid solutions in the scientific literature. In an attempt to fill that gap Brillouin spectroscopic as well as piezoelectric resonance investigations were conducted in a wide temperature range. The emphasis was placed on the transverse acoustic mode for which velocity is proportional to the C_{66}^{E} elastic constant, i.e. the mode which becomes soft in pure KDP due to piezoelectric coupling between the electric and elastic degrees of freedom.

The details of the experimental procedure were outlined in Section 4.1. For the light scattering experiments the sample orientation was that shown in Figure 2.2 b) as it is the only one which allows observation of the soft mode in crystals with $\bar{4}2m$ symmetry. However, in the same experimental geometry a longitudinal mode propagating in the [100] direction is also observable. Its velocity is proportional to the C_{11}^{E} elastic constant therefore its temperature dependence will also be discussed in this section.

Prior to the beginning of each temperature run the FSR of the FP interferometer was measured by collecting a spectrum of a fused silica block for which the Brillouin shifts are well known. The mirror spacing was adjusted when the overlap of the interference orders precluded the resolution of all peaks present in the spectrum. That procedure was facilitated by mounting the cryostat on special adjustable mount which allowed its removal from the laser beam. After each change of FSR the alignment and calibration procedures were repeated.

The time necessary for acquiring a good quality spectrum varied depending on the temperature of the sample. It ranged from approximately 2 hours to 4 hours in most cases, except at low temperatures where it was as high as 8 hours. To account for any temperature drifts the sample temperature was recorded at the beginning and at the end of each acquisition period. In most cases the difference was of the order of 0.05 K. The values reported here are the averages of the two. Certain difficulties with temperature stabilization were encountered in the immediate vicinity of the phase transition and at temperatures below 25 K. In the former case they are attributed to an increased specific heat of our samples close to T_c, and in the latter - to the cyclic nature of the operation of the closed cycle refrigeration unit.

The analysis of the spectra was performed using *Mathematica* [167] software. Specifically for that purpose a *Mathematica* package was written, which consisted of a collection of functions allowing an automatic location of the peaks in the spectra and fitting them to the sum of Gaussian line shapes of the form

$$I(\nu) = I_0 \exp\left[-\frac{(\nu - \nu_0)^2}{2w^2}\right] \tag{5.12}$$

where I_0, ν, ν_0 and w are the peak intensity, frequency, the Brillouin peak center frequency, and the width of the Gaussian profile respectively. The parameter w is related to the full width at half maximum, FWHM or Γ, by

$$\Gamma \approx 2.3548\ w. \tag{5.13}$$

The peak location was detected based on the second derivative of the intensity *vs.* channel number. At the same time the approximate width of the peaks was obtained. Those values were used as the initial guesses for the fitting parameters. Although initially the data were smoothed to facilitate peak location the fit was always performed on the original dataset. The number of peaks in each spectrum varied from

7 up to 13 depending on the analyzer settings and the temperature. Therefore up to 39 free parameters were fitted simultaneously. They were subsequently saved in a separate file for further processing. This procedure allowed for very rapid analysis of large numbers of data sets.

An example Brillouin spectrum collected from the KDP crystal at room temperature is shown in Figure 5.15. A conventional 5-pass interferometer was used in this case and the collection time was approximately 1 hour. The peaks marked as R (Rayleigh) correspond to unshifted, elastically scattered laser light. The difference between their positions is the Free Spectral Range which in this case was set to 18.51 GHz. Both, longitudinal (L) and transverse (T) acoustic modes propagating in the [100] direction are clearly identifiable. Their corresponding Brillouin shifts are also indicated in that figure. Thanks to the overlapping orders of interference both peaks could be observed simultaneously at that FSR. In the case of Sandercok's tandem Fabry-Perot interferometer [124], for the same mirror spacing the longitudinal modes would not be observable. However, in the case of 5 - pass system, if the acoustic mode's velocity depends strongly on temperature resulting in the shifting positions of corresponding Brillouin lines, the peaks will overlap in certain temperature intervals and it is necessary to change the FSR in order to resolve them. A systematic difference of the Brillouin shifts between Stokes and anti-Stokes lines was present in all spectra. It was of the order of 3 channels and was a result of nonlinearities in the response of the piezoelectric mirror actuators to the voltage ramp which was applied to them in order to scan the interferometer. The average values of the line centers were used to calculate acoustic phonon velocities and elastic constants. The estimated uncertainty in the values reported is not greater then 6%.

The value of the index of refraction used to calculate acoustic phonon velocities from the Equation 2.5 was $n = 1.49$. It is an average of the ordinary ($n_o = 1.51352$)

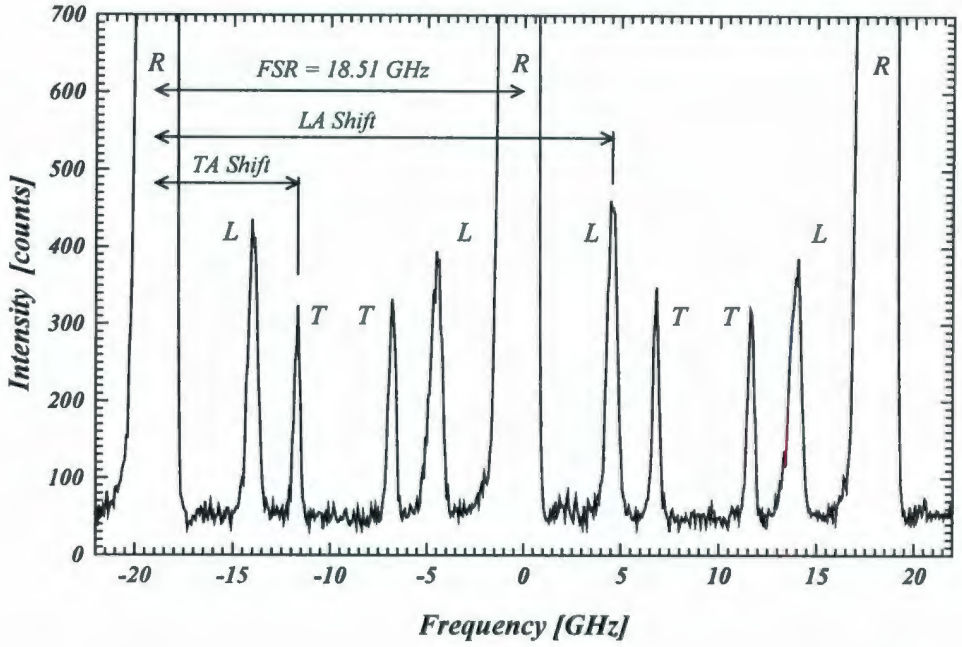

Figure 5.15: A typical Brillouin spectrum collected from KDP single crystal at room temperature.

and extraordinary ($n_e = 1.47131$) indices for KDP. Because the indices of refraction for KADP mixed crystals are not available the same value was used to analyze all the spectra for KDP-ADP solid solution as well. The error in absolute values of the phonon velocities introduced by this assumption is believed to be minimal and the temperatures of any anomalies observed is not affected at all. The densities of the crystals studied, and which were used to obtain the elastic constant values, were those determined from our X-ray analysis. They are reported in Table 3.4.

The primary purpose of conducting the measurements of the elastic properties of KDP-ADP solid solution by the piezoelectric resonance method was to confirm the findings of the Brillouin spectroscopic investigation. No experiments were conducted for pure KDP samples. For crystals of tetragonal symmetry there is only one way of measuring the C_{66}^{E} elastic constant by this method. The sample has to be prepared

in the shape of a plate with the largest surface normal to the [001] direction and with its edges parallel to the [100] and [010] directions. Application of the electric field along the z direction causes the plate to vibrate in the face-shearing mode. Suitable samples of the KADP:2.1 and KADP:12 crystals were prepared. Their dimensions are given in table 5.1. In the case of the KADP:12 crystal the sample used was the same one used earlier for dielectric constant measurements.

The experiments were conducted using the same setup as the dielectric constant measurements. The rate of temperature change was set to 0.5 K/min in the vicinity of the phase transition and the measuring voltage was set to 0.05 V. The lowest resonance observed at 296 K was tracked while the temperature was lowered. Its position was taken as the frequency at which the highest value of the output signal was recorded. Cooling and heating runs were conducted to observe any thermal hysteresis phenomena. The value of C_{66}^{E} was calculated using the following formula

$$f_r = \frac{1}{2}\sqrt{\frac{1}{w^2} + \frac{1}{l^2}}\sqrt{\frac{C_{66}^{E}}{\rho}} \tag{5.14}$$

where f_r, w, l and ρ are the resonant frequency of the face-shearing mode, width, length and the density of the sample, respectively. This equation takes into account the dependence of the resonant frequency on the ratio of the sample's width to its length as originally proposed by Mason [168].

Crystal	l [mm]	w [mm]	t [mm]	w/l
KADP:2.1	8.10	4.30	1.05	0.53
KADP:12	9.55	2.10	0.62	0.22

Table 5.1: Sample dimensions used for piezoelectric resonance studies.

5.2.1 KDP

In the process of sample preparation for the measurements of the elastic properties of KDP crystal two different samples were prepared with different orientation with respect to the crystallographic axis. Moreover, the sample used for temperature studies of the soft acoustic phonon, when rotated by 90 degrees, also allowed us to measure elastic constants associated with phonons propagating in the [001] direction. Room temperature Brillouin spectra were collected from all of those samples and allowed calculation of 4 elastic constants. The results are presented in Table 5.2. Values of the elastic constants previously reported in the literature are also included. As can be seen our results agree reasonably well with most of the published results. Any discrepancies could be attributed to small differences in sample orientation.

C_{11}	C_{33}	C_{44}	C_{66}	Ref.	Experimental
[GPa]					method
73.1	57.7	12.5	6.4	this work	BLS
80.0	80.0	12.8	6.1	[62]	PR
69.1	55.6	12.9	6.0	[169]	DL
71.4	56.2	12.7	6.2	[170]	UPE
74.0	68.0	13.5	6.3	[171]	PR
71.7	56.4	12.5	6.2	[172]	DL
71.7	56.8	12.7	6.4	[173]	BLS

Table 5.2: Room temperature values of elastic constants for KDP as determined by Brillouin spectroscopy compared with previously published results (BLS - Brillouin light scattering, UPE - ultrasonic pulse-echo method, PR - piezoelectric resonance method, DL - diffraction of light).

The temperature dependence of the C_{66}^E and C_{11}^E elastic constant for KDP crystal determined from Brillouin spectroscopy measurements are shown in Figure 5.16. Those data were collected upon cooling the sample from room temperature down to approximately 10 K. The C_{66}^E elastic constant displays a typical soft mode behavior as demonstrated earlier by Brody and Cummins [37]. Initially it increases slightly in the range from 300 K to 180 K and then sharply decreases to reach its minimum at the phase transition temperature. In the ferroelectric phase it initially sharply increases with decreasing temperature and reaches its room temperature value about 10 K below T_c. Upon further cooling its value remains approximately constant at the level of 7 GPa down to the lowest temperatures. The scatter of the experimental data points in the range from 100 K to 10 K is a result of very weak intensities of the Brillouin lines corresponding to the transverse acoustic phonon which made the determination of its position somewhat difficult. The existence of ferroelastic domains, and their dynamics, in the low temperature phase could result in the scattering volume being located in different regions of the sample at different temperatures. Since KDP belongs to the orthorhombic point group below T_c, with nonequivalent [100] and [010] directions this could result in different elastic constants. To clarify this situation it is necessary to bring the sample into a monodomain state by application of an external electric field or appropriate stress. However, this procedure will smear out the phase transition and shift it towards higher temperatures [37].

The analysis of the experimental data was performed based on Equation 2.72 from section 2.3.2. Combined with Equation 2.53 we see that the C_{66}^E elastic constant should obey the following relation in the vicinity of the phase transition in the paraelectric phase

$$C_{66}^E = C_{66}^P - \frac{b^2}{a(T - T_0)} \tag{5.15}$$

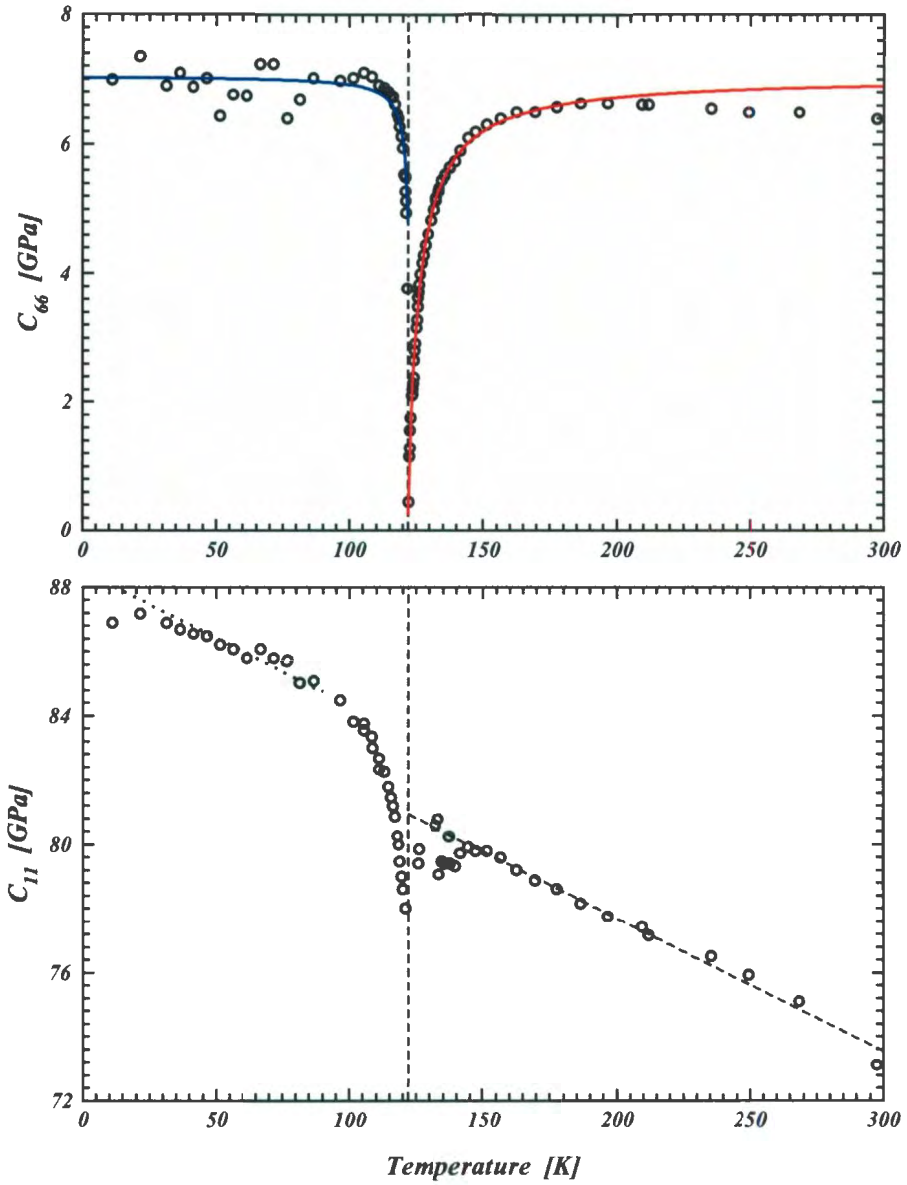

Figure 5.16: The temperature dependence of the C_{66} and C_{11} elastic constants for KDP as determined by the Brillouin spectroscopy method.

where the constant a is the inverse of the Curie-Weiss constant for the clamped crystal and was determined during the analysis of the high frequency dielectric constant. Its value taken for the purposes of this analysis was $a = 0.0002755\ \mathrm{K}^{-1}$. Also the value of $T_0 = 118$ K as determined previously was used in the analysis. Therefore there are only two remaining free parameters to be determined. The result of the fit of the Equation 5.15 to the temperature dependence of the C_{66}^E above T_c is shown in Figure 5.16. Data points in the range from T_c to 165 K were used for the fit. The results of this analysis indicate that the value of the elastic constant at constant polarization is $C_{66}^P = (7.05 \pm 0.20)$ GPa which is in excellent agreement with published results [62].

Combining Equation 2.72 with the expression for the clamped inverse susceptibility (Equation 2.54) we obtain the following formula describing the temperature behavior of the C_{66}^E elastic constant below T_c

$$C_{66}^E = C_{66}^P - \frac{b^2}{8a(T_c - T) + \frac{3B^2}{4D}} \tag{5.16}$$

All of the parameters in the above equation were already known from previous analysis. The constant in the denominator $(3B^2/4D)$ was estimated from Equation 2.50 where the difference $T_0 - T_c = 4$ K as determined from the dielectric constant data. Equation 5.16 is plotted on Figure 5.16 as a solid blue line. It can be seen that it approximates the experimental data very well with the values of the coefficients chosen. The small deviations of th edata from the model above 160 K as well as below 100 K are most likely a result of the assumption of the temperature independence of the C_{66}^P and b constants.

The temperature dependence of the C_{11}^E also displays an anomalous behavior in the vicinity of the transition temperature as can be seen in Figure 5.16. In the paraelectric phase its value increases linearly with decreasing temperature at a rate of

0.0416 GPa/K as shown. Then it decreases from the value of approximately 81 GPa at 135 K down to 78 GPa at T_c. In the ferroelectric phase it increases from its minimum value initially in a nonlinear fashion. In the temperature range between 90 K and 10 K it continues to increase at the rate approximately equal to that in the paraelectric phase as shown by the dotted line in Figure 5.16 which is just a guide, not a fit. This fact indicates that its value at constant polarization is probably linearly dependent on temperature in the entire range of temperatures studied. Since the Landau model introduced in section 2.3.2 accounts only for the temperature dependence of the C_{66}^E elastic constant no quantitative analysis was performed on the data for C_{11}^E.

5.2.2 KADP1

The temperature dependence of the C_{66}^E and C_{11}^E elastic constants as determined by Brillouin spectroscopy for the KADP:2.1 crystal is shown in Figure 5.17. The room temperature value of the C_{66}^E elastic constant is essentially the same as in the case of KDP and equals 6.35 GPa. However, the addition of only 2.1 mol % of ADP seems to affect slightly the C_{11}^E constant which in this case is 74.7 GPa at room temperature. Overall the curves shown in Figure 5.17 display qualitatively similar behavior to those presented in the previous section. However there are important differences, in particular in the immediate vicinity of the phase transition. The analysis of the elastic constant data, in particular the temperature dependence of the soft mode, was conducted in the similar fashion as in the case of KDP, i.e. by means of the Landau model presented in Section 2.3.2. The results are shown in Figure 5.17. The solid red line is a fit of the equation

$$C_{66}^E = C_{66}^P - \frac{b^2}{a(T - T_c) + \frac{3B^2}{16D}} \tag{5.17}$$

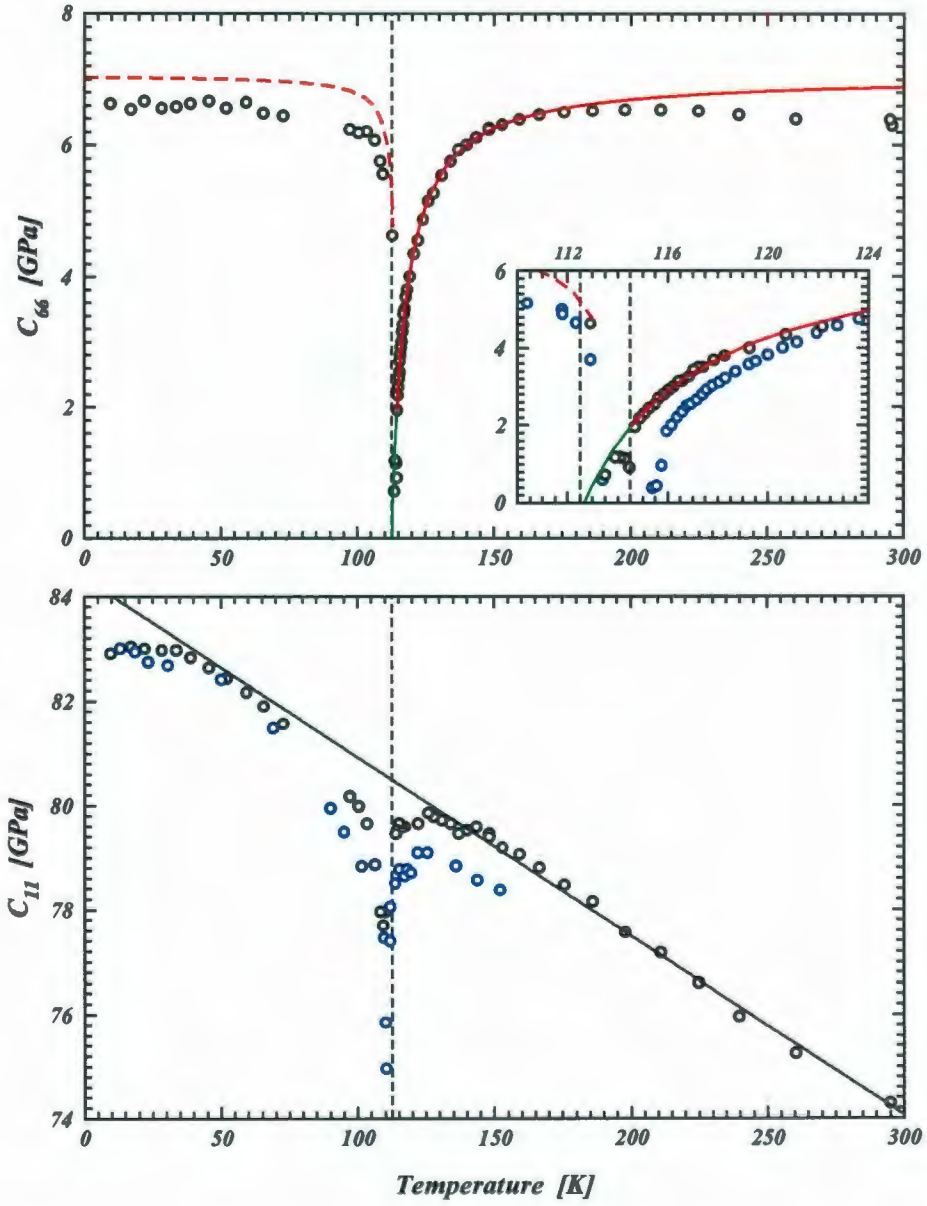

Figure 5.17: The temperature dependence of the C_{66} and C_{11} elastic constants for the KADP:2.1 crystal as determined by the Brillouin spectroscopy method. Black and blue open circles designate cooling and heating runs respectively.

with T_c and a coefficients set to 112.5 K and 3.35×10^{-4} K^{-1} as determined from the dielectric constant experiments. Only data points in the range from 114.5 K up to 160 K were used for that analysis. The solid green line in Figure 5.17 is the extrapolation line down to T_c. The parameters predicted by the fit were used to plot the temperature dependence of the C_{66}^E in the low temperature region (dashed red line). It can be seen that the model correctly predicts its behavior although the value of C_{66}^P, determined from that analysis to be 7.06 GPa, assumed to be a constant, appears to be overestimated by a small amount. The possibility that the C_{66}^P is a slowly varying function of T is a plausible reason for that discrepancy. Moreover, as can be seen in the insert in the Figure 5.17 there exists a small temperature interval, between 112.5 K and 114.5 K, where the experimental data points do not follow the theoretical curve. The appearance of a new phase in KADP:2.1 crystal could be a reason for that deviation. The C_{66}^E *vs.* T data show a discontinuous jump at 114.5 K. This feature, as well as the existence of measurable thermal hysteresis, is clearly visible in the data collected during heating of the sample (blue circles in the insert in Figure 5.17). Although the temperature span where the new phase is visible is very narrow it is consistent with already published results indicating a phase coexistence phenomenon in mixed crystals of KDP type [93]. Brillouin spectroscopy is therefore a better measuring technique for investigating the KDP-ADP solid solution phase diagram in the region of small ADP concentration since any possible new phase transitions appear to be clearly identifiable from those results. It should also be mentioned that the results presented above are the first of their kind. The only elastic properties measurements results present in the scientific literature are those published for RADP single crystals in the ammonium concentration region where only the glassy phase forms.

The appearance of the new phase in the KADP:2.1 crystal in the temperature

region between 112.5 K and 114.5 K was associated with a dramatic increase in the intensity of the elastically scattered light. A photograph of the image of the laser beam passing through the crystal as projected on the pinhole P_1 (see Figure 4.2) inside the spatial filter, taken at the temperature of 114 K is shown in Figure 5.18. It can be seen

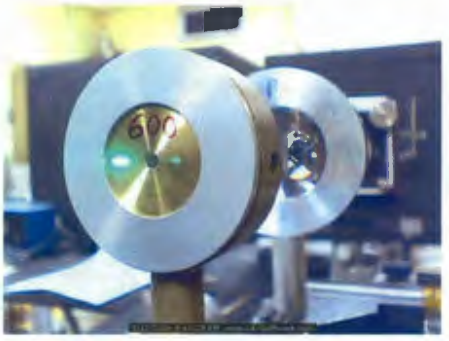

Figure 5.18: An image of the laser beam passing through a crystal on a pinhole inside a spatial filter.

that the entire volume of the sample was not involved in that process. Upon lowering the temperature below 112 K the sample returned to normal. Warming up the sample resulted in the reappearance of the strongly scattered Rayleigh light. Therefore the phenomenon was confirmed to be reproducible. No quantitative analysis of that phenomenon was performed. The fact that it was also observed during measurements performed on KADP:12 crystal, as will be discussed in the next section, indicates that it can be correlated with the amount of NH_4 ions incorporated into the crystal structure.

The temperature dependence of the C_{66}^E elastic constant for the KADP:2.1 crystal obtained from the piezoelectric resonance measurements is shown in Figure 5.19. For comparison purposes the results of the Brillouin spectroscopy measurements are also included. It can be seen that the C_{66}^E *vs.* T data resemble closely that obtained from the analysis of the Brillouin spectra. It displays a minimum at a $T_c = 114.5$ K

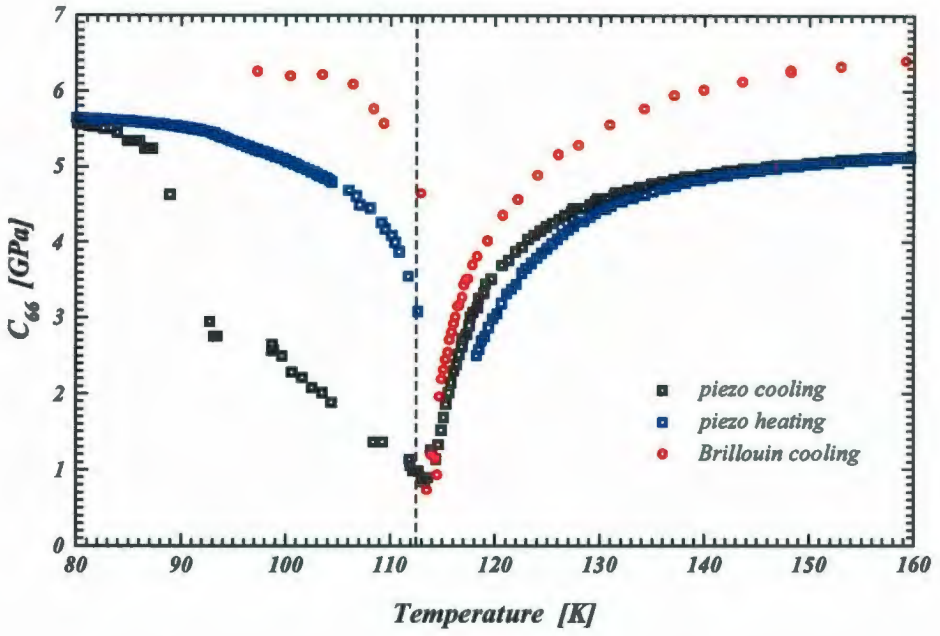

Figure 5.19: A comparison between the temperature dependence of the C_{66} elastic constant for KADP:2.1 crystal as determined by the piezoelectric resonance method and Brillouin spectroscopy.

in agreement with previous results. The differences in the rate of change of the C_{66}^{E} elastic constant in the high temperature phase can be attributed to structural inhomogeneities present in the sample. They would influence the frequency of the mechanical resonance of a crystal plate resulting in small differences in the values of the elastic constant obtained. The existence of the ferroelastic domains, as well as domain wall mobility, would have a similar effect. In fact the results presented in Figure 5.19 confirm this hypothesis. The values of the C_{66}^{E} elastic constant are very different from those obtained by Brillouin spectroscopy in the temperature range corresponding to the plateau region. At the same time is is interesting to notice that this discrepancy is much smaller in the heating run. Since no repeated measurements were conducted it cannot be concluded whether this behavior is reproducible or not.

However, it should be pointed out that the domain structure could be different for the cooling and heating runs due to the aging effect [149].

It can also be noticed in Figure 5.19 that the values of the C_{66}^{E} elastic constant obtained from the resonant frequency are considerably lower than those obtained from the spectroscopic investigation in the regions far from the phase transition. Although the elastic dispersion cannot be excluded as a possible reason for this discrepancy, the phenomenon of mode coupling is the most likely cause of it. The face-shear mode is known to couple with a flexular mode of vibration. The coupling is a consequence of the fact that in both cases the resulting deformation of the sample is very similar. To illustrate its effect the frequency spectrum of a Y-cut[3] quartz crystal recorded by W. Mason [3] are shown in Figure 5.20. Although the data shown in that figure are for a different material the general principles of mode coupling are applicable to any sample vibrating in the face-shear mode. Similar curves were reported for an ADP crystal by Mason [62] however the graph shown in Figure 5.20 is more suitable for illustration purposes since it shows the flexural modes as well as the face-shear modes. The four dashed lines originating from a point (0,0) in that graph represent the dependence of the frequencies of the flexural modes on sample dimensions. The other dashed line is a plot of Equation 5.14 representing the dependence of the face-shear mode on sample dimensions. The solid lines indicate the resulting coupled resonances that are observed. It is evident that subsequent harmonics are coupled to an even-order flexular modes. It can be seen that this mechanism greatly affects the f_r. The magnitude of the effect depends on the sample dimensions. The difference between the experimental and the theoretical frequencies for the first resonance (lowest solid line) for the width to length ratio of the order of 0.5 and 0.2 (those values correspond

[3]Y-cut is a standard designation of a cut when a crystalline plate has its largest face normal to the [010] direction and its edges parallel to [100] and [001] directions.

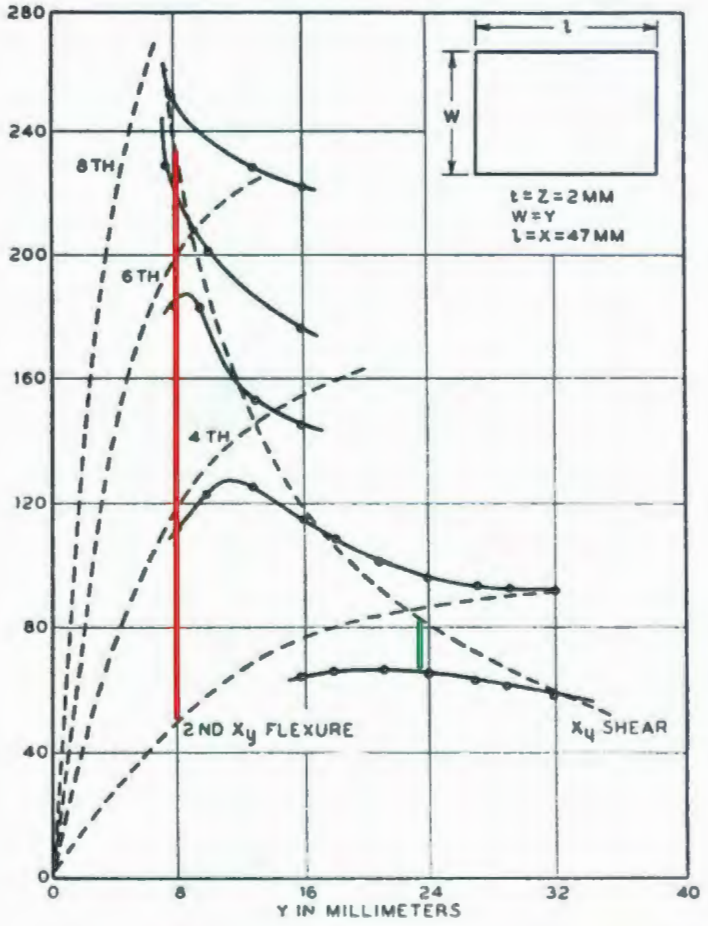

Figure 5.20: The dependence of the resonant frequency (in kHz) of a crystalline plate of quartz vibrating in the face-shear mode on sample dimensions illustrating the coupling of modes (after [3]).

to the appropriate ratios of the sample dimmentions used in this thesis) is indicated by the green and red bars, respectively. Clearly the discrepancy is greater for smaller width to length ratio.

Finally we turn our attention to the temperature dependence of the C_{11}^E elastic constant shown in the bottom graph in Figure 5.17. It confirms the existence of the phase transition in KADP:2.1 sample. Its value initially increases linearly with decreasing temperature at a rate of 34.3×10^{-3} GPaK^{-1}, i.e. slightly higher then in the case of pure KDP, from its room temperature value up to approximately 80 GPa at 125 K. This behavior is represented by the solid line on the graph which is a result of a linear fit for the data points in the region from 125 K up to 296 K, the highest temperature at which a spectrum was collected. A clear minimum of C_{11}^E is observed at T_c. Below that temperature its value increases quickly and approximatelly 20 K below transition temperature attains the rate of increase simmilar to that in the paraelectric phase. At approximately 35 K it reaches the value of 83 GPa and remains constant down to 10 K. Similar temperature behavior was observed during heating of the sample as represented by the blue circles in the bottom graph in Figure 5.17. Since the anomalous behavior of the transverse acoustic mode was of greater interest in this study not enough data points were collected for C_{11}^E elastic constant, therefore the existence of the thermal hysteresis associated with the phase transformation is not clearly represented in that graph.

5.2.3 KADP2

The temperature dependence of the C_{66}^E and C_{11}^E elastic constants obtained from the analysis of Brillouin spectra of the KADP:12 crystal are presented in Figure 5.21. The experiments were conducted only during cooling of the sample. Moreover, due

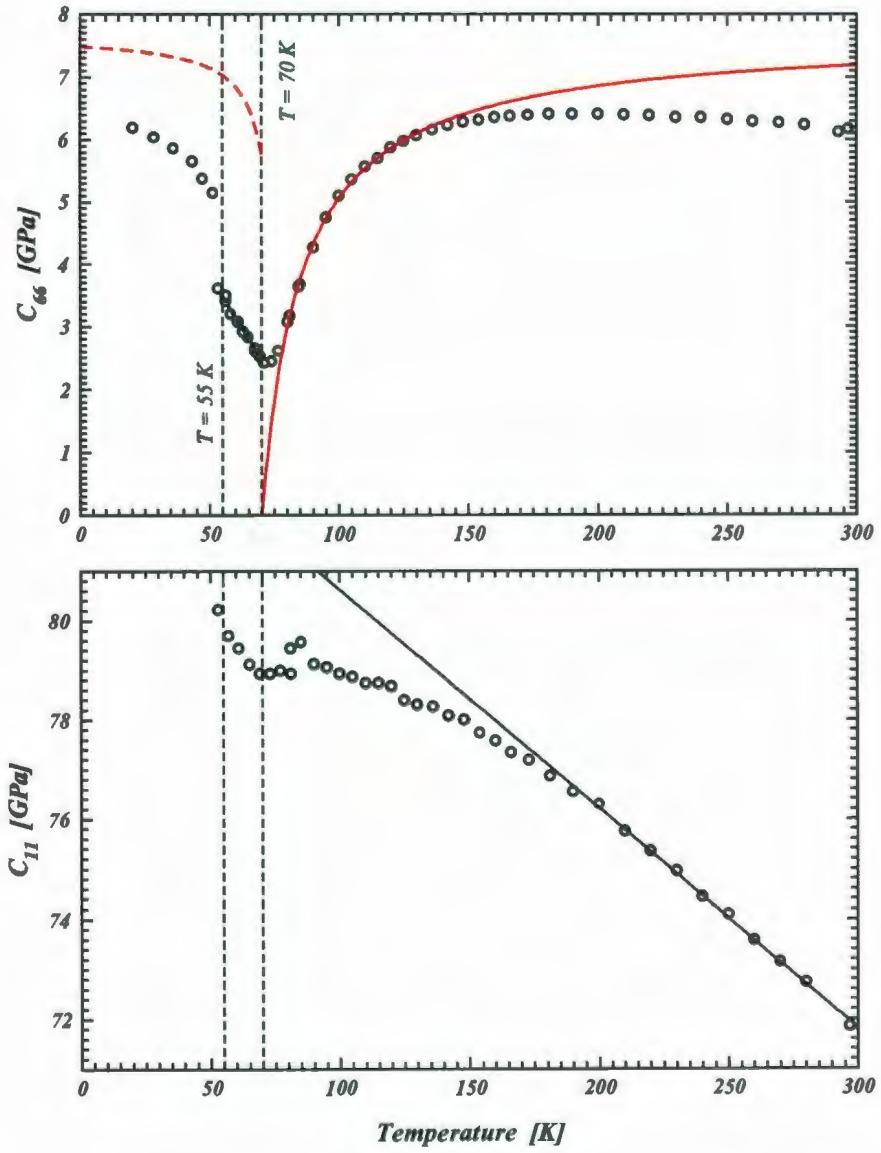

Figure 5.21: The temperature dependence of the C_{66} and C_{11} elastic constants for the KADP:12 crystal as determined by the Brillouin spectroscopy method.

to appearance of the strong elastically scattered component below 80 K it was impossible to perform quantitative analysis of the spectra collected using the traditional 5-pass system. Therefore experiments in that temperature range were repeated using Sandercock Tandem 3+3 pass system. Its very high contrast allowed the data collection despite the strong Rayleigh component. In the process of data analysis it was realized that the peak shape is better approximated by a Lorenzian line shape of the form

$$I(\omega) = I_0 \frac{\frac{1}{2}\Gamma}{(\omega - \omega_0)^2 + \left(\frac{1}{2}\Gamma\right)^2} \tag{5.18}$$

where Γ is the full width at half maximum of the peak profile. This was quite obvious at the temperatures very close to the phase transition where the width of the Brillouin lines was greater then the width of the instrumental response function. The Brillouin shift obtained from that analysis was corrected for the difference in wavelength of the laser light used (532 nm in the case of Tandem system). After plotting both data sets in the same graph the curves overlapped in the region between 80 K and 90 K confirming their self consistency. They were therefore joined and treated as one set for further analysis. It was assumed that the value of the index of refraction was not very much different for the two wavelengths and the value of $n = 1.49$ was used to calculate the acoustic phonon velocity.

As can be seen in Figure 5.21 the temperature dependence of the C_{66}^E elastic constant resembles closely the typical soft mode behavior in the paraelectric phase. However, the softening is only of the order of 60 % relative to the room temperature value. Although it might be rather questionable that the Landau model presented in Section 2.3.2 is applicable for a crystal with a large amount of structural disorder, it was decided to analyze the data in the same fashion as before for comparison purposes. The solid red line in Figure 5.21 is a result of the fit of equation 5.15 to the data points

in the temperature range from 80 K to 150 K. This formula was chosen to minimize the number of free parameters of the fit in the light of the fact that a precise value of T_c could not be deduced from the dielectric constant analysis. However the value of the parameter a was taken as the inverse of the clamped Curie-Weiss constant as determined earlier. The best fit line was characterized by $C_{66}^{P} = 7.70 \pm 0.35$ GPa, i.e. similar to the value of the same parameter determined for the KDP and KADP:2.1 crystals, and, $T_0 = 54.8$ K a value which is very close to the temperature at which a discontinuous decrease of the dielectric constant was observed. Assuming that the theoretical value of $C_{66}^{E} = 0$ at T_c we were able to calculate the value of 70.1 K for the Curie-Weiss temperature, which is in a very good agreement with the temperature at which the minimum of the free dielectric susceptibility occurs. The experimentally determined values of C_{66}^{E} *vs.* T exhibit a minimum at that temperature.

Although the results of the analysis of the temperature dependence of the C_{66}^{E} elastic constant in the paraelectric phase based on the Landau model were encouraging, it is clear that the model does not predict the correct behavior of this parameter below T_c. This fact can be ascertained by comparing the theoretical curve represented by the dashed red line in Figure 5.21 with the experimental data points. This is not a surprise since the experimental data indicate clearly the broadening of the temperature region in which the new phase already present in the KADP:2.1 sample is stable. This region extends from T_c down to 55 K, the latter being the value of T_0. It is not clear at the moment if there is any physical significance related to the fact that the new phase appears between those two characteristic temperatures. The C_{66}^{E} elastic constant increases linearly at a rate of 6.8×10^{-2} GPa/K with decreasing temperature in that range. Upon further cooling its value increases discontinuously at approximately 55 K from 3.8 GPa to 5.1 GPa and continues to increase in a nonlinear way at temperatures below 55 K. It reaches the value of 6.2 GPa at 20 K, the lowest

temperature attained in this experiment. Clearly the incorporation of 12 mol % of NH_4 cations into the KDP crystal structure modifies its elastic properties to a large extent in the temperature range below T_c.

The Brillouin result is compared with the temperature dependence of the C_{66}^E elastic constant obtained from the piezoelectric resonance measurement in Figure 5.22. The large difference in the absolute value of the elastic constant is attributed to

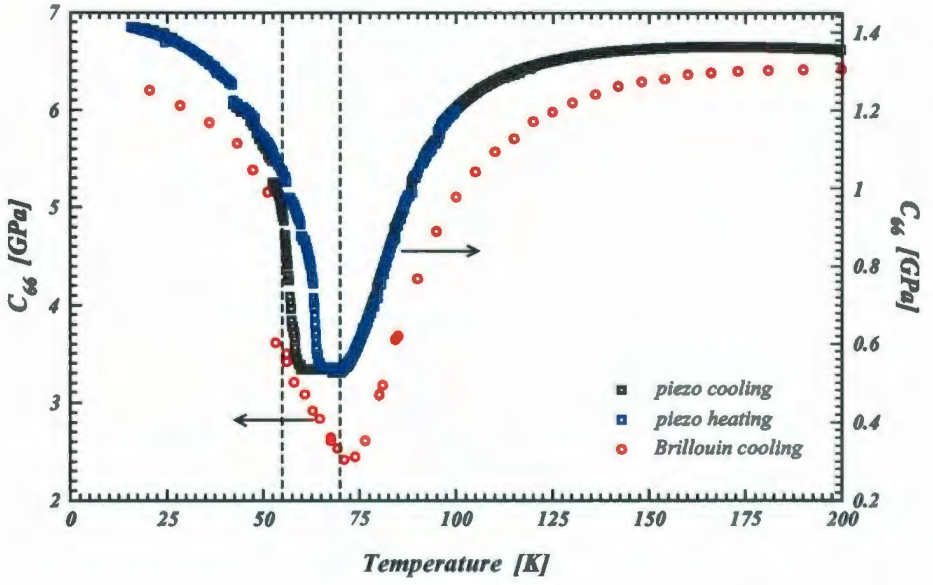

Figure 5.22: A comparison between the temperature dependence of the C_{66} elastic constant for KADP:2.1 crystal as determined by the piezoelectric resonance method and Brillouin spectroscopy.

the shear-to-flexure mode coupling phenomenon as before. Notwithstanding, the two data sets are in good qualitative agreement and the existence of the new phase in the temperature region between 55 K and 70 K is confirmed. However, the temperature dependence of the C_{66}^E elastic constant in that region is different than that obtained previously. Instead of increasing with decreasing temperature it remains approximately constant. Moreover, no discontinuity was observed in the vicinity of

T_0 but a steep increase of C_{66}^E was observed. Those differences can be attributed to the existence of clusters rich in NH_4 ion content which are characterized by a slightly different phase transition temperature. Therefore this discontinuity will be smeared out because the piezoelectric resonance method measures the effective elastic constant of a crystalline plate as a whole, whereas Brillouin spectroscopy is a local probe. It is interesting to note that the anomalous behavior of the C_{66}^E elastic constant in the vicinity of T_0 is characterized by a thermal hysteresis of the order of 10 K. The anomaly occurs at 67 K during the heating run and this temperature corresponds to the temperature at which the regions which scatter laser light very strongly completely disappeared as determined by a visual observation during the Brillouin spectroscopy experiments.

The temperature dependence of C_{11}^E elastic constant in the vicinity of the phase transition in the KADP:12 crystal is also modified by the incorporation of NH_4 cations as can be seen in the bottom graph in Figure 5.21. In particular, although initially its value increases linearly with decreasing temperature at a rate of 44.1×10^{-3} GPa/K the experimental data points start to deviate from the straight line already 100 K before T_c is reached. The linear increase is represented by the black solid line in Figure 5.21 which is a result of the linear regression analysis conducted on the data in the range from room temperature down to 190 K. The rate of increase of this elastic constant decreases gradually and at approximately 90 K it is zero and the C_{11}^E attains a value of 79 GPa. It remains constant down to 70 K and then starts to increase linearly again at a rate similar to that close to room temperature. No minimum of the C_{11}^E *vs.* T dependence at T_c was observed. Unfortunately no spectra were collected in the temperature range below T_0 due to the strong elastically scattered light obscuring the spectra to a large extent. Also, since the temperature dependence of the velocity of the transverse acoustic mode was of greater interest to us the

FSR used for the experiments conducted using the Tandem system was chosen to be 10 GHz. This excluded the possibility of the observation of the longitudinal mode in that experiment.

As already mentioned earlier the strong elastically scattered component was also observed during experiments conducted on the KADP:12 sample. Although no quantitative analysis of this phenomenon was carried out, certain regularities were noticed. As in the case of the KADP:2.1 crystal the entire volume of the sample did not start to scatter light very strongly at once. The first of the strong scattering regions appeared at temperatures close to the T_0 on the high temperature side as can be seen in the upper right hand photograph shown in Figure 5.23. For comparison purposes

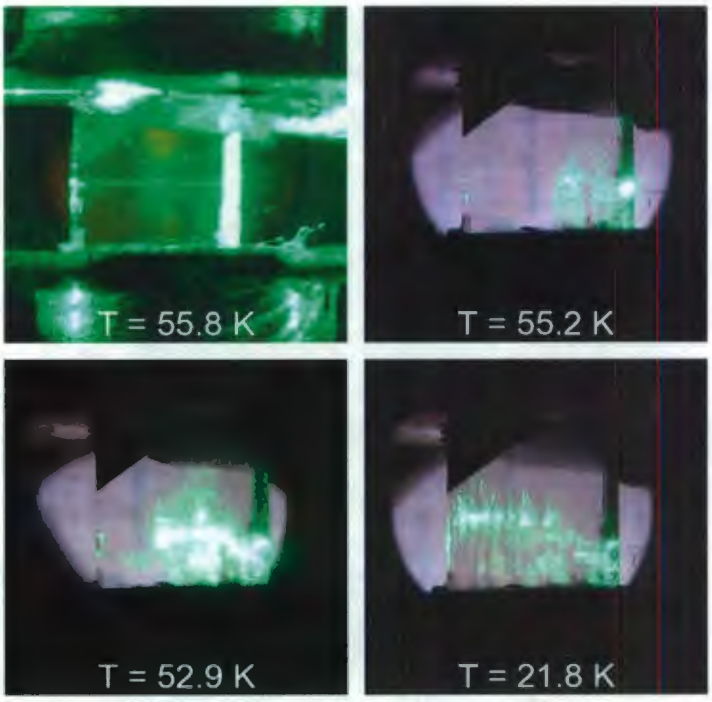

Figure 5.23: Photographs of the KADP:12 crystal inside the cryostat at different temperatures illustrating the development of the regions responsible for strong elastically scattered light.

a picture of the sample enclosed in the cryostat at T=55.8 K is also shown there. At that temperature the laser beam is clearly visible crossing the entire width of the crystal from left to right. Upon further cooling the region extended towards the left (see the bottom left hand side picture in Figure 5.23) and at a few degrees below encompassed the entire sample. It needs to be mentioned that the sample of the KADP:12 crystal became clear again at temperature around 67 K upon heating, showing considerable hysteresis effect. This temperature behavior was reproducible. The sample was cooled down and warmed up several times with the same results. Under the assumption that the phenomenon is caused by lattice defects introduced by incorporation of NH_4 cations in the structure, the sample was removed from the cryostat and annealed for 2 hours at 373 K. Cooling the sample again down to 55 K resulted in the reappearance of those regions. Since the annealing period was short it is possible that this effect could be eliminated entirely after holding the sample at elevated temperatures for several days.

Pile Higher and Deeper
by Jorge Cham
www.phdcomics.com

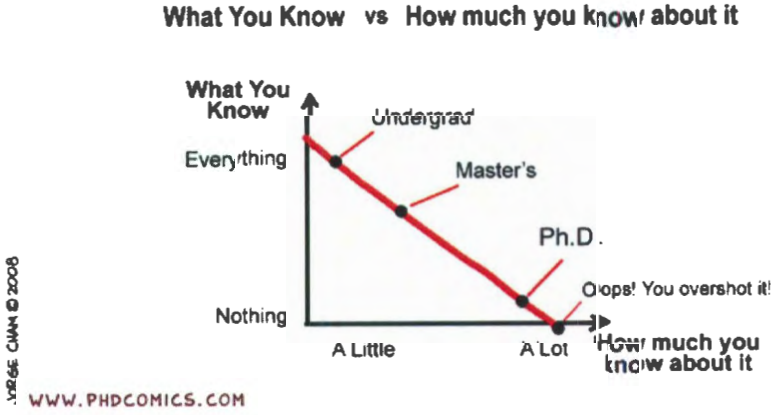

Chapter 6

Summary and Conclusions

The KDP crystal was one of the first ferroelectric materials discovered. Although its phase transition is very well explained by the standard Landau theory of phase transitions, a considerable amount of effort was directed towards understanding the peculiar behaviour of the temperature dependence of its dielectric constant in the temperature range of approximately 30 K below T_c where the plateau region was observed. Until recently it was a unique feature of this material. Several theoretical models were proposed to explain this phenomenon. Although the influence of defects and impurities on the growth habit as well as on the dielectric properties of KDP has been known for years no attempt was made to correlate all of them. Since the incorporation of the trivalent metal ions into KDP structure prevents the growth of large single crystals with considerable amounts of the impurities in it the studies of KDP-ADP solid solution overcomes that problem because good quality single crystals can be grown over the entire range of compositions. Although the determination of the content and distribution of the impurities is an experimentally difficult task the approach employed in this thesis seems to be much more promising. The basic idea is that the measurements of many physical properties should be conducted on crystals

grown from the same batch.

Based on that premise the measurements of the dielectric constant ε_{33}, the C_{66}^E and C_{11}^E elastic constants were performed on the KDP-ADP crystals grown from aqueous solution. The elastic properties were investigated with two different experimental techniques: Brillouin spectroscopy and the piezoelectric resonance method. They were in good qualitative agreement with each other. All of the differences can be atributed to the inhomogeneous distribution of the NH_4 ions in the KDP matrix. Moreover the elastic properties correlate very well with the dielectric properties in terms of the temperatures at which major anomalies were observed.

All of the dielectric constant data were analyzed by means of the Landau model presented in Section 2.3.2. The phenomenological parameters obtained are summarized in Table 6.1. The Curie-Weiss law is obeyed in all cases in the high temperature

Parameter	KDP	KADP:2.1	KADP:12
T_c [K]	122.1 ± 0.3	112.5 ± 0.3	70[a]
$\tilde{T}_0$ [K]	122.0 ± 0.4	112.0 ± 0.6	–
T_0 [K]	118.0 ± 0.5	108.8 ± 0.6	55.0[a]
T_f [K]	100 ± 2	88 ± 2	$\sim 58 \pm 2$
$T_c - T_f/T_c$	0.18 ± 0.02	0.22 ± 0.02	0.18 ± 0.03
ε_r at T_c	20000	5400	470
ε_r at 296 K	30	55	12
C_{C-W}^{σ} [K]	3520 ± 25	3100 ± 22	1880 ± 30
C_{C-W}^{ε} [K]	3620 ± 20	2980 ± 25	1770 ± 30

[a] *as determined from the analysis of the C_{66} vs. T data*

Table 6.1: Summary of selected parameters extracted from the analysis of the dielectric constant measurements for all crystals studied.

phase whereas the anomalous plateau region present in all crystals just below T_c precluded any quantitative analysis in that temperature range. The values of the T_c and T_f both decrease with increasing NH_4 concentration in agreement with previously published results. The Curie-Weiss constant for clamped as well as for free mechanical conditions also decreases with increasing x. However, for the mixed crystals $C^{\sigma}_{C-W} > C^{\epsilon}_{C-W}$. Although no systematic dependence of the room temperature value of the relative dielectric constant as a function of concentration was observed the peak values decreased dramatically with increasing ammonium ion content. This is probably the effect of the long range antiferroelectric ordering gradually becoming more pronounced in the NH_4 rich regions of the sample. It is interesting to note that the ratio of the width of the plateau region to the transition temperature remains approximately constant for all three crystals studied. Finally, two types of dispersion were observed in all samples studied. The first which is resonant in nature, is a direct consequence of the piezoelectric coupling. The second which is relaxational in nature, is a consequence of the existence of the permanent dipole moments in the unit cells of these materials. In the case of the KDP-ADP solid solutions, the latter type of dispersion is characterized by a very broad distribution of relaxation times with its mean relaxation time and its width strongly dependent on the temperature. This is the precursor of the proton glass phase fully realized in samples with amonium concentration higher than the criticall value of approximately 0.25. It would be of great benefit to complement the dielectric data presented in this thesis by conducting measurements in ultra low and very high frequency ranges.

The analysis of the temperature dependence of the C^{E}_{66} elastic constant was also conducted based on the phenomenological theory of phase transitions. Certain parameters obtained from the analysis of the dielectric constant were used and as a result very good agreement between the two datasets was obtained, specifically in

the paraelectric phase. The theoretical predictions of the Landau model in the low temperature range were in good agreement with the data only for the pure KDP crystal. The general features of the temperature dependence of the C_{66}^{E} elastic constant were confirmed by the piezoelectric resonant measurements of the same parameter. Any discrepancies between the two can be explained by assuming an inhomogeneous distribution of NH_4 ions in the host crystal. The observation of a very strong elastically scattered light below 55 K in the crystal with the highest concentration provides additional support for that hypothesis. Better qualtative agreement between the two datasets could be obtained if the effect of the shear-to-flex mode coupling was treated more thoroughly. However, in order to achieve this large, good quality single crystals are needed to allow for the preparation of samples of different width to length ratios.

The appearance of a new phase in the KADP:12 crystal was clearly observed in the C_{66}^{E} *vs.* T data, but its nature is not known at present. Since the dielectric constant data does not clearly indicate the anomalies present in the temperature dependence of the C_{66}^{E} elastic constant related to the new phase transitions, one can conclude that the internal stresses present in the samples could be primary reason for its appearance. Therefore it would be interesting to study the elastic properties of KDP-ADP mixed crystals in wider range of the composition to further confirm this findings. Moreover, similar measurements should be performed on RADP single crystals. In that compound the smaller mismatch in ionic size between Rb^{+} and NH_4^{+} results in smaller internal stresses. Therefore the absence of the anomalous temperature behavior of the elastic properties would confirm the above hypothesis. Also, more detailed investigation of the dielectric constant would clarify the issue of the presence or absence of any anomalies of this physical property related to the existence of the new phase. The measurements should be conducted over wider frequency range then those presented in this thesis allowing for the quantitative analysis of the dispersion

processes involved.

In conclusion the data presented in this thesis support the hypothesis that the type and the amount of impurities and/or defects present in the sample strongly influences the temperature dependence of its physical properties. In particular it appears that they could induce new structural transformations in the crystals. Therefore the control of the impurities content seems to be of crucial importance in any future work. In particular, care should be taken to eliminate any impurities (in the present case the trivalent metal ions) other then the ones purposely introduced by the experimenter. This could be achieved by using the highest purity starting materials. It would also minimize the probability of crystal cracking during growth which in turn would allow a production of large specimens. Moreover, the crystal growth conditions have to be carefully controlled and maintained the same for all crystals. In addition to that, a thorough structural analysis has to be conducted prior to any other measurements, with particular emphasis on the existence of multiple phases resulting from lattice distortions around defects. Finally, any qualitative information about the spatial homogeneity of the crystals would also be of great benefit. X-ray topography, micro-Raman or micro-Brillouin techniques are good candidates for that type of analysis.

Pile Higher and Deeper
by Jorge Cham
www.phdcomics.com

Bibliography

[1] K.-H. Hellwege and A. M. Hellwege, eds., *Landolt - Bornstein Numerical Data and Functional Relationships in Science and Technology*, vol. 16 of *New Series. Group III: Crystal and Solid State Physics* (Springer-Verlag Berlin-Heidelberg, 1982).

[2] Y. Ono, T. Hikita, and T. Ikeda, J. Phys. Soc. Jpn. **56**, 577 (1987).

[3] W. P. Mason, *Piezoelectric Crystals and Their Application to Ultrasonics* (D. Van Nostrand Company Inc., 1950).

[4] S. F. Edwards and P. W. Anderson, J. Phys. F: Metal Phys. **5**, 965 (1975).

[5] D. Sherrington and S. Kirkpatrick, Phys. Rev. Lett. **35**, 1792 (1975).

[6] J. West, Z. Kristallogr. **74**, 306 (1930).

[7] G. E. Bacon and R. S. Pease, Proc. Roy. Soc. (London) A **220**, 397 (1953).

[8] A. R. Ubbelohde and I. Woodward, Proc. Roy. Soc. A (London) **188**, 358 (1947).

[9] B. C. Frazer and R. Pepinsky, Acta Cryst. **6**, 273 (1953).

[10] G. E. Bacon and R. S. Pease, Proc. Roy. Soc. A (London) **230**, 359 (1955).

[11] T. Plesser and H. Stiller, Solid State Communications **7**, 323 (1969).

[12] R. J. Nelmes and V. R. Eiriksson, Solid State Communications **11**, 1261 (1972).

[13] J. C. Slater, Journal of Chemical Physics **9**, 16 (1941).

[14] M. de Quervain, Helv. Phys. Acta **17**, 509 (1944).

[15] G. Busch and P. Scherrer, Naturwissenschaft **23**, 737 (1935).

[16] G. Busch, Helv. Phys. Acta **11**, 269 (1938).

[17] B. A. Strukov, A. Baddur, V. A. Koptsik, and I. A. Velichko, Sov. Phys. Solid State **14**, 885 (1972).

[18] G. A. Samara, Ferroelectrics **5**, 25 (1973).

[19] H. M. Barkla and D. M. Finlayson, Philos. Mag. **44**, 109 (1953).

[20] B. Paul, J. Albers, and H. E. Muser, Ferroelectrics **14**, 707 (1976).

[21] J. Bornarel and B. Torche, Ferroelectrics **76**, 201 (1987).

[22] E. Nakamura, Ferroelectrics **135**, 237 (1992).

[23] S. Havlin, E. Litov, and E. A. Ueling, Phys. Rev. B **9**, 1024 (1974).

[24] S. Havlin, E. Litov, and H. Sompolinsky, Phys. Lett. A **51**, 33 (1975).

[25] T. Mitsui and J. Furuichi, Phys. Rev. **90**, 193 (1953).

[26] J. W. Benepe and W. Reese, Phys. Rev. B **3**, 3032 (1971).

[27] Y. Uesu, T. Tanaka, and J. Kobayashi, Ferroelectrics **7**, 247 (1974).

[28] J. Kobayashi, Y. Uesu, I. Mizutani, and Y. Enomoto, Phys. Status Solidi (a) **3**, 63 (1970).

[29] J. Kobayashi, Y. Uesu, and Y. Enomoto, Phys. Status Solidi (b) **45**, 293 (1971).

[30] C. C. Stephenson and J. G. Hooley, J. Amer. Chem. Soc. **66**, 1397 (1944).

[31] H. R. Danner and R. Pepinsky, Phys. Rev. **99**, 1215 (1955).

[32] W. N. Lawless, Ferroelectrics **71**, 149 (1987).

[33] I. P. Kaminow and T. C. Damen, Phys. Rev. Letters **20**, 1105 (1968).

[34] C. Y. She, T. W. Broberg, L. S. Wall, and D. F. Edwards, Phys. Rev. B **6**, 1847 (1972).

[35] P. S. Peercy, Phys. Rev. B **12**, 2725 (1975).

[36] E. M. Brody and H. Z. Cummins, Phys. Rev. Letters **21**, 1263 (1968).

[37] E. M. Brody and H. Z. Cummins, Phys. Rev. B **9**, 179 (1974).

[38] V. H. Schmidt, Bull. Am. Phys. Soc. **19**, 649 (1974).

[39] V. H. Schmidt, A. B. Western, and A. G. Baker, Phys. Rev. Lett. **37**, 839 (1976).

[40] P. Bastie, M. Vallade, C. Vettier, and C. M. E. Zeyen, Phys. Rev. Lett. **40**, 337 (1978).

[41] G. A. Samara, Phys. Rev. Lett. **27**, 103 (1971).

[42] N. Lagakos and H. Z. Cummins, Phys. Rev. B **10**, 1063 (1974).

[43] I. L. Fabelinskii, *Molecular Scattering of Light* (Plenum Press, 1968).

[44] E. Courtens, Phys. Rev. Letters **41**, 1171 (1978).

[45] A. S. Chaves, F. V. Letelier, J. F. Sampaio, and R. Gazzinelli, Phys. Rev. B **47**, 4880 (1993).

[46] J. F. Araujo, J. M. Filho, F. E. A. Melo, F. V. Letelier, and A. S. Chaves, Phys. Rev. B **57**, 783 (1998).

[47] B.-G. Kim, Phys. Rev. B **59**, 13509 (1999).

[48] L. Pauling, J. Am. Chem. Soc. **57**, 2680 (1935).

[49] W. Bantle, Helv. Phys. Acta **15**, 373 (1942).

[50] K. K. Kobayashi, J. Phys. Soc. Jpn. **24**, 497 (1968).

[51] M. Ichikawa and K. Motida, Phys. Rev. B **36**, 874 (1987).

[52] H. Bilz, G. Benedek, and A. Bussmann-Holder, Phys. Rev. B **35**, 4840 (1987).

[53] M. E. Lines and A. M. Glass, *Principles and Applications of Ferroelectrics and Related Materials* (Oxford University Press, 2001).

[54] A. Bussmann-Holder, H. Bilz, and G. Benedek, Phys. Rev. B **39**, 9214 (1989).

[55] A. Bussmann-Holder and K. H. Michel, Phys. Rev. Lett. **80**, 2173 (1998).

[56] S. B. Hendricks, Amer. J. Sci. **14**, 269 (1927).

[57] R. Ueda, J. Phys. Soc. Jpn **3**, 328 (1948).

[58] A. A. Khan and W. H. Baur, Acta Cryst. B **29**, 2721 (1973).

[59] L. Tenzer, B. C. Frazer, and R. Pepinsky, Acta Cryst. **11**, 505 (1958).

[60] A. W. Hewat, Nature **246**, 90 (1973).

[61] R. O. Keeling, Jr. and R. Pepinsky, Z. Krist. **106**, 236 (1955).

[62] W. P. Mason, Phys. Rev. **69**, 173 (1946).

[63] C. C. Stephenson and A. C. Zettlemoyer, J. Am. Chem. Soc. **66**, 1405 (1944).

[64] M. Amin and B. A. Strukov, Sov. Phys. Solid State **12**, 1616 (1971).

[65] D. J. Genin, D. E. O'Reilly, and T. Tsung, Phys. Rev. **167**, 445 (1968).

[66] T. Nagamiya, Progr. theor. Phys. **7**, 275 (1952).

[67] Y. Ishibashi, S. Ohya, and Y. Takagi, J. Phys. Soc. Jpn. **33**, 1545 (1972).

[68] P. Askenasy and F. Nessler, Z. Anorg. Chem. **189**, 305 (1930).

[69] A. Y. Zvorykin and V. G. Kuznetssov, Bull. acad. sci. U.R.S.S. **1**, 195 (1938).

[70] I. Nitta, R. Kiriyama, and M. Haisa, Sci. Pap. Osaka Univ. **No. 30**, 1 (1951).

[71] E. Courtens, Ferroelectrics **72**, 229 (1987).

[72] E. Courtens, J. Phys. Lett. (Paris) **43**, L199 (1982).

[73] Z. Trybuła and J. Stankowski, Cond. Matter Phys. **1**, 311 (1998).

[74] U. T. Höchli, K. Knorr, and A. Loidl, Adv. Phys. **51**, 589 (2002).

[75] Y. Kim, S. I. Kwun, S. Park, B. Oh, and D. Lee, Phys. Rev. B **28**, 3922 (1983).

[76] B. K. Choi and J. J. Kim, Phys. Rev. B **28**, 1623 (1983).

[77] A. D. Bruce and R. A. Cowley, Adv. Phys. **29**, 219 (1980).

[78] S. A. Gridnev, L. N. Korotkov, and L. A. Shuvalov, Ferroelectrics **144**, 157 (1993).

[79] S. A. Gridnev, L. N. Korotkov, L. A. Shuvalov, and R. M. Fedosyuk, Ferroelectrics **175**, 107 (1996).

[80] E. Courtens, T. F. Rosenbaum, S. E. Nagler, and P. M. Horn, Phys. Rev. B **29**, 515 (1984).

[81] S. A. Gridnev, L. N. Korotkov, and L. A. Shuvalov, Ferroelectrics **167**, 99 (1995).

[82] J. A. Mydosh, *Spin Glasses. An Experimental Intoduction* (Taylor & Francis, 1993).

[83] E. Courtens and H. Vogt, Z. Phys. B - Condensed Matter **62**, 143 (1986).

[84] Y. A. Popkov and A. V. Vankevich, Low Temp. Phys. **21**, 930 (1995).

[85] E. Courtens and H. Vogt, J. Chim. Phys. **82**, 317 (1985).

[86] T. Hattori, H. Araki, S. Nakashima, A. Mitsuishi, and H. Terauchi, J. Phys. Soc. Jpn. **56**, 781 (1987).

[87] Y. A. Popkov, A. V. Vankevich, L. A. Shuvalov, and R. M. Fedosyuk, Low Temp. Phys. **19**, 138 (1993).

[88] T. Hattori, H. Araki, S. Nakashima, A. Mitsuishi, and H. Terauchi, J. Phys. Soc. Jpn. **57**, 1127 (1988).

[89] A. F. Wells, *Structural Inorganic Chemistry* (Clarendon Press, 1984).

[90] W. R. Cook, Jr., J. Appl. Phys. **38**, 1637 (1967).

[91] A. Boukhris, C. Lecomte, B. Wyncke, F. Brehat, and A. Thalal, J. Phys.: Cond. Matter **6**, 2475 (1994).

[92] A. Boukhris, M. Souhassou, C. Lecomte, B. Wyncke, and A. Thalal, J. Phys.: Cond. Matter **10**, 1621 (1998).

[93] Z. Trybuła and J. Kaszyński, Ferroelectrics **298**, 347 (2004).

[94] J. Kaszyński, Z. Trybuła, and H. Małuszyńska, Acta Physica Polonica A **108**, 103 (2005).

[95] M. Lax and D. F. Nelson, in *Theory of Light Scattering in Condensed Matter*, edited by B. Bendow, J. L. Birman, and V. M. Agranovich (Plenum Press, New York, 1976), pp. 371–390.

[96] H. Z. Cummins and P. E. Schoen, in *Laser Handbook*, edited by F. T. Arecchi and E. O. Schulz-Dubois (North-Holland Publishing Company, 1972), pp. 1029–1075.

[97] J. F. Nye, *Physical properties of Crystals. Their representation by tensors and matrices* (Oxford University Press, 1957).

[98] D. J. Griffiths, *Introduction to Electrodynamics* (Prentice Hall, 1999).

[99] P. Debye, *Polar Molecules* (Dover, 1945).

[100] A. Chełkowski, *Dielectric Physics* (Elsevier, 1980).

[101] C. J. F. Böttcher and P. Bordewijk, *Theory of Electric Polarization* (Elsevier, 1978).

[102] I. Bunget and M. Popescu, *Physics of Solid Dielectrics* (Elsevier, 1984).

[103] D. W. Davidson and R. H. Cole, J. Chem. Phys. **18**, 1417 (1951).

[104] D. W. Davidson and R. H. Cole, J. Chem. Phys. **19**, 1484 (1951).

[105] B.-G. Kim and J.-J. Kim, Phys. Rev. B **55**, 5558 (1997).

[106] V. Janovec, V. Dvorak, and J. Petzelt, Czech J. Phys. B **25**, 1362 (1975).

[107] J. Grindlay, *An Introduction to the Phenomenological Theory of Ferroelectricity* (Pergamon Press, 1970).

[108] J. C. Słonczewski, Phys. Rev. B **1**, 3599 (1970).

[109] I. Prigogine and R. Defay, *Chemical Thermodynamics* (Longman, 1957).

[110] J. W. Mullin, *Crystallization* (Elsevier, 2001).

[111] W. Ostwald, Zeitschrift fur Physikalische Chemie **22**, 289 (1897).

[112] A. E. Robinson, Disc. Farad. Soc. **5**, 315 (1949).

[113] F. C. Frank, Discution of the Faraday Society **5**, 48 (1949).

[114] L. N. Rashkovich, *KDP-family Single Crystals* (Adam Hilger, 1991).

[115] J. W. Mullin and A. Amatavivadhana, Journal of Applied Chemistry **17**, 151 (1967).

[116] J. W. Mullin, A. Amatavivadhana, and M. Chakraborty, Journal of Applied Chemistry **20**, 153 (1970).

[117] R. M. Garrels and C. L. Christ, *Solutions, Minerals, and Equilibria* (Jones and Bartlett Publishers, 1990).

[118] H. P. Klug and L. E. Alexander, *X-ray diffraction procedures for polycrystalline and amorphous materials.* (Wiley, 1974).

[119] H. M. Rietveld, Acta Crystallographica **22**, 151 (1967).

[120] L. Lutterotti, *Maud*, available at: `http://www.ing.unitn.it/~ maud/`.

[121] E. I. Suvorova and V. V. Klechkovskaya, Ferroelectrics **144**, 245 (1993).

[122] E. I. Suvorova and V. V. Klechkovskaya, Crystallography Reports **39**, 1011 (1994).

[123] E. I. Suvorova and V. V. Klechkovskaya, Ferroelectrics **151**, 187 (1994).

[124] *Tandem Fabry - Perot Interferometer TFP - 1. Operator Manual.*, JRS Scientific Instruments, Zwillikon, Switzerland (2004).

[125] M. Born and E. Wolf, *Principles of Optics* (Cambridge University Press, 1999).

[126] P. Hariharan and D. Sen, J. Opt. Soc. Am. **51**, 398 (1961).

[127] J. G. Dil, N. C. J. A. van Hijningen, F. van Dorst, and R. M. Aarts, Applied Optics **20**, 1374 (1981).

[128] J. R. Sandercock, *U.S. Patent 4,225,236* (1980).

[129] S. M. Lindsay, M. W. Anderson, and J. R. Sandercock, Rev. Sci. Instrum. **52**, 1478 (1981).

[130] J. M. Vaughan, *The Fabry-Perot Interferometer* (IOP Publishing Ltd., 1989).

[131] P. Curie and J. Curie, Bull. Soc. Min. de France **3**, 90 (1880).

[132] M. G. Lippmann, Ann. de Chimie et de Phys **24**, 145 (1881).

[133] T. Ikeda, *Fundamentals of Piezoelectricity* (Oxford University Press, 1996).

[134] W. P. Masson, *Crystal Physics of Interaction Processes* (Academic Press, 1966).

[135] T. Krajewski, *Zagadnienia Fizyki Dielektryków*, Problemy Elektroniki i Telekomunikacji (Wydawnictwa Komunikacji i Ł ączności, 1970).

[136] X.-H. Du, Q.-M. Wang, and K. Uchino, IEEE T. Ultrason. Ferr. **51**, 227 (2004).

[137] X.-H. Du, Q.-M. Wang, and K. Uchino, IEEE T. Ultrason. Ferr. **51**, 238 (2004).

[138] J. Bornarel and J. Lajzerowicz, J. Appl. Phys. **39**, 4339 (1968).

[139] Y. N. Huang, X. Li, Y. N. Wang, H. M. Shen, Z. F. Zhang, C. S. Fang, S. H. Zhuo, and P. C. W. Fung, Phys. Rev. B **55**, 16159 (1997).

[140] J. Bornarel, J. Appl. Phys. **42**, 845 (1972).

[141] V. N. Fedosov and A. S. Sidorkin, Sov. Phys. Solid State **19**, 1359 (1977).

[142] M. A. Moore and H. C. W. L. Williams, J. Phys. C: Solid State Phys. **5**, 3168 (1972).

[143] K. Kuramoto, J. Phys. Soc. Jpn. **56**, 1859 (1987).

[144] J. Bornarel and B. Torche, Ferroelectrics **132**, 273 (1992).

[145] D. Hull and D. J. Bacon, *Introduction to Dislocations.* (Butterworth-Heinemann, 2001).

[146] E. Nakamura, K. Kuramoto, K. Deguchi, and K. Hayashi, Ferroelectrics **98**, 51 (1989).

[147] H. Motegi, K. Kuramoto, E. Nakamura, K. Hayashi, and I. Kitayama, J. Phys. Soc. Jpn. **54**, 2735 (1985).

[148] V. Mueller, Y. Shchur, H. Beige, A. Fuith, and S. Stepanow, Europhys. Lett. **57**, 107 (2002).

[149] V. Mueller, H. Beige, and Y. Shchur, Ferroelectrics **290**, 151 (2003).

[150] L. N. Kamysheva and S. N. Drozhdin, Ferroelectrics **71**, 281 (1987).

[151] R. W. Gammon, E. Courtens, and W. B. Daniels, Phys. Rev. B **27**, 4359 (1983).

[152] S. Sen Gupta, T. Kar, and S. P. Sen Gupta, Materials Chemistry nd Physics **58**, 227 (1999).

[153] L. N. Korotkov, L. A. Shuvalov, and R. M. Fedosyuk, Ferroelectrics **265**, 99 (2002).

[154] L.Vegard, Z. Phys. **5**, 17 (1921).

[155] L. E. Cross, Ferroelectrics **76**, 241 (1987).

[156] S. Li, J. A. Eastman, R. E. Newnham, and L. E. Cross, Phys. Rev. B **55**, 12067 (1997).

[157] N. Setter and L. E. Cross, J. Appl. Phys. **51**, 4356 (1980).

[158] C. G. F. Stenger, F. L. Scholten, and A. J. Burggraat, Solid State Comm. **32**, 989 (1979).

[159] C. A. Randall, D. J. Barber, R. W. Whatmore, and P. Groves, J. Mat. Sci. **21**, 4456 (1986).

[160] C. A. Randall, D. J. Barber, P. Groves, and R. W. Whatmore, J. Mat. Sci. **23**, 3678 (1988).

[161] A. D. Hilton, D. J. Barber, C. A. Randall, and T. R. Shrout, J. Mat. Sci. **25**, 3461 (1990).

[162] V. V. Kirillov and V. A. Isupov, Ferroelectrics **5**, 3 (1973).

[163] J. Chen, H. M. Chan, and M. P. Harmer, J. Am. Ceram. Soc. **72**, 593 (1989).

[164] L. N. Korotkov, S. A. Gridnev, and R. M. Fedosyuk, Crystallography Reports **44**, 821 (1999).

[165] L. N. Korotkov, S. A. Gridnev, L. A. Shuvalov, and R. M. Fedosyuk, Ferroelectrics **299**, 133 (2004).

[166] E. Nakamura and K. Kuramoto, J. Phys. Soc. Jpn. **57**, 2182 (1988).

[167] I. Wolfram Research, *Mathematica 5.1* (Wolfram Research, Inc., Champaign, Illinois, 2005).

[168] W. P. Mason, Bell System Technical Journal **13**, 405 (1934).

[169] B. Zwicker, Helv. Phys. Acta **19**, 523 (1946).

[170] W. J. Price and H. B. Hungtington, J. Acoust. Soc. Am. **22**, 32 (1950).

[171] W. Bantle, B. Matthias, and P. Scherrer, Helv. Phys. Acta **18**, 389 (1945).

[172] S. Haussühl, Z. Kristallogr. **120**, 401 (1964).

[173] L. Boyer and R. Vacher, Phys. Status Solidi a **6**, K105 (1971).